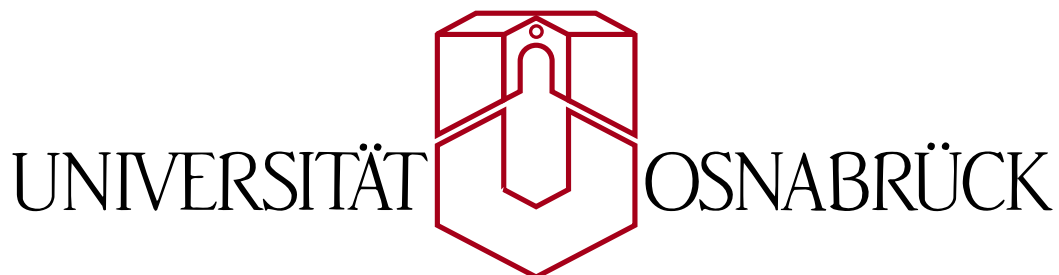

Mutual interactions of femtosecond pulses and transient gratings in nonlinear optical spectroscopy

KUMULATIVE DISSERTATION
ZUR ERLANGUNG DES GRADES
EINES DOKTOR DER NATURWISSENSCHAFTEN

von
Stefan Nolte

GENEHMIGT DURCH DEN FACHBEREICH PHYSIK DER



August 2018

Erstgutachter:	Prof. Dr. Mirco Imlau
Zweitgutachter:	Prof. Dr. Dominik Schaniel
Tag der Einreichung:	9. August 2018
Tag der Disputation:	30. Oktober 2018

Contents

1	Introduction	3
2	Fundamental principles	6
2.1	Femtosecond laser pulses	6
2.1.1	Mathematical description	6
2.1.2	Dispersion & pulse shaping	8
2.2	Lithium niobate	9
2.2.1	Nonlinear optical properties	9
2.2.2	Grating recording	10
3	Ultrafast absorption spectroscopy	12
3.1	Z-Scan with different pulse durations	12
3.2	Transient absorption with ultrafast white light supercontinuum	13
3.2.1	Experimental technique	13
3.2.2	Experimental results	14
3.2.3	Discussion	17
4	Pulse interaction with self-induced and static gratings	20
4.1	Frequency-resolved optical gating from self-diffraction	20
4.1.1	Experimental technique	20
4.1.2	Phase retrieval algorithm	21
4.1.3	Experimental results	23
4.1.4	Discussion	25
4.2	Two color holography	28
4.3	Grating-assisted energy transfer	29
4.4	Diffraction of ultrashort lasers pulses from relief gratings	30
5	Conclusion & outlook	31
A	Publications	37
A.1	Scanning nonlinear absorption in lithium niobate over the time regime of small polaron formation	37
A.2	Interference and holography with femtosecond laser pulses of different colours	51
A.3	Doppler-shifted Raman-Nath diffraction from gratings recorded in LiNbO ₃ with ultra-short laser pulses of different color	60
A.4	Dynamic-grating-assisted energy transfer between ultrashort laser pulses in lithium niobate	67

A.5 Chirp control of femtosecond-pulse scattering from drag-reducing surface-relief gratings	84
--	----

Chapter 1

Introduction

Starting with A. Einstein's description of stimulated emission of light from population inversion in 1917 [1], C. H. Townes and coworkers for the first time utilized this principle of amplification to produce coherent electromagnetic waves, in a device called maser - *microwave amplification by stimulated emission of radiation* [2]. Working for visible light, the first laser was realized by T. Maiman in 1960 [3]. Since, efforts were made to generate subsequently shorter pulses below the temporal resolution of electronic devices, from picosecond pulse durations [4] to femtoseconds [5] and even attoseconds in 2001 [6]. The work of A. H. Zewail established the spectroscopic usage of femtosecond laser pulses to investigate structural changes and transitions of molecules, what was called *femtochemistry* [7]. Accompanied by the development of coherent light sources, the holographic principle, invented by D. Gabor with electron beams in 1948 [8], became widely applicable as well.

Spectroscopy with ultrashort laser pulses offers the possibility to observe optical processes on a new timescale. Because of the revolutionary temporal domain, extreme peak intensities can be reached with relatively low pulse energies and optical laser powers. These intensities efficiently enable to study and utilize nonlinear optical phenomena, like high-harmonic generation or frequency conversion [9, 10]. Not only the pulse duration and the magnitude of intensities are a breakthrough, one has to deal with broad bandwidths, complex temporal profiles and the influence of the medium on these parameters and the pulse itself.

This work is dedicated to a comprehensive experimental study on the interaction of femtosecond laser pulses with the nonlinear optical medium lithium niobate. The nonlinear optical response in the nanosecond regime was already studied extensively with a variety of techniques, whereas femtosecond pulses were mainly used in transient absorption or transient grating experiments. Naturally, the temporal resolution of these measurements depends on the pulse duration, however, dynamics during the pulse excitation were barely investigated.

The motivation of this work is to widen the limits of femtosecond spectroscopy, not only to temporally resolve faster nonlinear optical processes, but further to show a sensitivity to other coupling mechanisms between the pulses and the material. Especially, the role of transient, dynamic holographic gratings is investigated with a careful determination of the pulse duration, bandwidth and frequency chirp. A basis of this work is established in the first part by studying the material response via light-induced absorption before focusing on the main topic, the pulse interaction with elementary (holographic) gratings, both self-induced and static, in the second

part. By this detailed study, several features of femtosecond laser pulses, holographic gratings and the ultrafast material response can be revealed: (i) grating recording is feasible even with pulses of different frequencies, provided that their pulse duration is sufficiently short, (ii) grating based pulse coupling causes a pronounced energy transfer even in a common pump-probe setup for transient absorption measurements with (non-)degenerated frequencies, (iii) beyond expectation, oscillations in the phonon frequency range become apparent in different measurements. The presented results point towards appropriate future experiments to obtain a more consistent, microscopic model for the ultrafast response of the crystal, involving the interplay between photo-generated polarons, self-induced gratings, and phonons.

The medium lithium niobate is chosen because of its pronounced nonlinear optical properties and the multitude of previous investigations with continuous waves as well as pulsed laser light during the last decades. Famous for its photorefractive effect, the capability of persistent data storage was investigated in lithium niobate [11, 12]. Pronounced two-photon absorption and optical Kerr-effect are reported [13]. It features metastable entities as small polarons or free charge-carriers [14, 15], that can be responsible for charge transport or laser induced damaging of the sample [16]. Both photo-generated states are investigated by transient absorption measurements [17–19] and/or recording of a holographic grating [15, 20]. A comprehensive overview of the nonlinear optical properties and different polaronic states of lithium niobate is given in the following section 2.2.

In the context of a detailed study of the nonlinear absorption particular relations are investigated. As it is already established in literature, lithium niobate features the photo-generation of polarons within the femtosecond timescale [17–19]. It is of interest how the formation process influences the absorption of the excitation pulse itself. Therefore, the established z-scan technique is extended by pulse shaping to apply variable pulse durations. Further, broadband absorption spectra are studied when using a white light supercontinuum probe pulse to monitor the excitation from a sub-50 fs laser pulse. This reveals complete absorption spectra and also oscillations in the terahertz frequency regime. The latter can be compared with impulsive stimulated Raman scattering, a coherent excitation of phonon modes. A strong damping of these oscillations in the order of a picosecond is discovered.

The following dependencies are studied to clarify the interaction between ultra-short laser pulses and elementary gratings. Based on the fringe pattern from two coherent waves, an intensity modulation can be transferred into a medium by different optical processes to record a holographic grating (see section 2.2.2). First, self-diffraction from a self-induced grating is analyzed to obtain characteristics of the used pulses in a frequency-resolved optical gating measurement. Afterwards, it is of interest how this interference pattern depends on the particular pulse characteristics: duration and frequency detuning. It is demonstrated for the first time that even in the case of frequency detuned femtosecond pulses the modulation is sufficient to record a hologram with an image bearing pulse. The novel finding of recording of a dynamic grating with femtosecond pulses of different color exhibits self-diffraction as well. In a detailed study of this phenomenon it can be shown that the diffracted light gets affected by the Doppler-effect. Besides, the two interacting pulses yield an energy transfer that is based on self-induced gratings as well. In a comprehensive study two coupling mechanisms are identified: transient energy transfer from different intensities and gain from a dynamic grating because of a frequency detuning. The first

effect was newly observed in a bulk material on the femtosecond timescale. On the other hand, the detuning dependence exhibits a maximum in the terahertz frequency regime, that is comparable with the results obtained from absorption spectroscopy and self-diffraction. Finally, the influence of the pulse duration, frequency chirp and bandwidth on the light fringes is underlined by investigating the diffraction pattern from a static relief grating. By carefully adjusting these pulse parameters, the fine structure of the diffraction signal can be switched on and off.

Chapter 2

Fundamental principles

2.1 Femtosecond laser pulses

The description of femtosecond laser pulses is given based on the *Springer handbook of lasers and optics* from F. Träger [21].

2.1.1 Mathematical description

Real laser pulses contain a spatial and temporal dimension, what is often described by a transversal $I(x, y)$ and a temporal $I(t)$ intensity profile. Both of them are used to estimate the peak intensity from a known pulse energy W . In the following, only the temporal profile is of interest because naturally this is the feature that distinguishes pulses from continuous waves. To describe the time dependent electric field $E(t)$ of the pulse, an envelope function $A(t)$ is multiplied by an harmonic oscillation with an angular frequency ω_0 and a starting phase ϕ_0 :

$$E(t) = A(t) \cos(\omega_0 t + \phi_0) = \frac{1}{2} (\tilde{E}(t) + \tilde{E}^*(t)) , \quad (2.1)$$

$$\tilde{E}(t) = A(t) \exp [i(\omega_0 t + \phi_0)] . \quad (2.2)$$

More general, a complex-valued electric field $\tilde{E}(t)$ and its complex conjugate $\tilde{E}^*(t)$ are used. The intensity $I(t)$ can be obtained from the squared amplitude of this field multiplied by additional constants that are neglected here:

$$I(t) \propto |\tilde{E}(t)|^2 = A(t)^2 . \quad (2.3)$$

Furthermore, ultrashort pulses are rarely monochromatic with a single frequency ω_0 , but rather contain a bandwidth $\Delta\omega$ and even a certain distribution of the frequencies within the pulse $\omega(t)$. When describing the oscillating pulse field $E(t)$, it is more common to extend the time dependent phase $\phi(t)$ with higher order derivatives:

$$\phi(t) = \int \omega(t) dt = \phi_0 + \omega_0 t + \frac{1}{2} \frac{d\omega}{dt} t^2 + \dots . \quad (2.4)$$

Therein, the phase is obtained from an integral of the angular frequency which linearly changes with time $\omega(t) = \omega_0 + \dot{\omega}t$. Besides this fundamental description, the Fourier

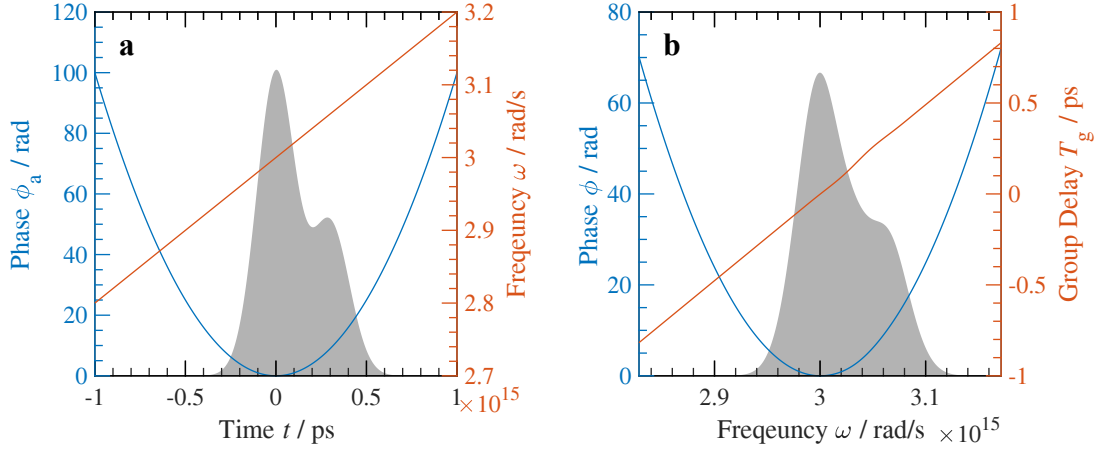


Figure 2.1: Fourier transform relation of an arbitrary pulse shape. (a) time dependence of intensity I (gray shaded), nonlinear phase $\phi_a = 1/2 \cdot \dot{\omega} t^2$ (blue) and frequency ω (red). (b) spectral dependence of intensity I (gray shaded), phase ϕ (blue) and group delay T_g (red).

transform is of major interest, because it correlates the temporal and spectral domain:

$$\tilde{E}(\omega) = \frac{1}{\sqrt{2\pi}} \int_{-\infty}^{\infty} \tilde{E}(t) \exp(-i\omega t) dt , \quad (2.5)$$

$$\tilde{E}(t) = \frac{1}{\sqrt{2\pi}} \int_{-\infty}^{\infty} \tilde{E}(\omega) \exp(i\omega t) d\omega . \quad (2.6)$$

Similar to the temporal domain, the spectral intensity $I(\omega)$ is defined as follows:

$$\tilde{E}(\omega) = A(\omega) \exp [i\phi(\omega)] , \quad (2.7)$$

$$E(\omega) = \frac{1}{2} (\tilde{E}(\omega) + \tilde{E}^*(\omega)) , \quad (2.8)$$

$$I(\omega) \propto |\tilde{E}(\omega)|^2 = A(\omega)^2 . \quad (2.9)$$

The spectrum $\tilde{E}(\omega)$ is complex-valued as well and contains a spectral phase $\phi(\omega)$ similar to $\phi(t)$ that is most often approximated by a Taylor series:

$$\phi(\omega) = \phi(\omega_0) + \phi'(\omega - \omega_0) + \frac{1}{2} \phi''(\omega_0) (\omega - \omega_0)^2 + \dots \quad (2.10)$$

The spectral phase $\phi(\omega)$ is affected by the dispersion of a medium, i.e., the first derivative $\phi'(\omega)$ describes the pulse delay and the second derivative $\phi''(\omega)$ represents the group velocity dispersion, a broadening of the pulse duration. With this tools, it is possible to simulate the influence of a medium on the temporal pulse shape.

For elementary pulse shapes the Fourier transform provides a limit of the pulse duration Δt and bandwidth $\Delta \omega$ (both the full width at half maximum of the intensity). Very often a Gaussian temporal shape is assumed for which this limit is

$$\Delta t \Delta \omega \geq 4 \ln(2) . \quad (2.11)$$

In other words, when reducing the pulse duration, the bandwidth needs to be extended and contrariwise. For a Gaussian-shaped pulse, this limit can be used with the measured bandwidth to indicate a minimal pulse duration. Vice versa, a measured pulse duration can indicate a lower limit of the bandwidth. In both cases the assumed variable can be larger.

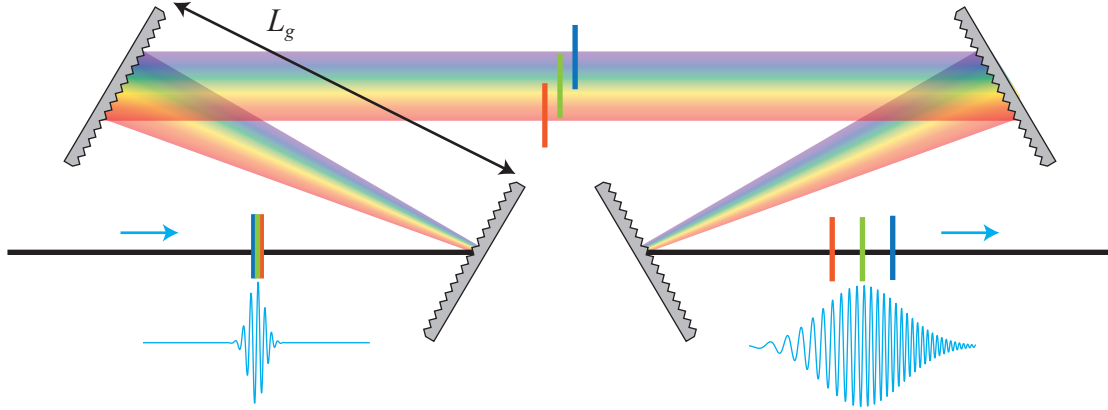


Figure 2.2: Scheme of a grating compressor. Four equal gratings (gray) are placed mirror-symmetrically to introduce a negative chirp to an incident Fourier-limited pulse (compare blue pulse shapes). The optical path lengths are different for each wavelength, resulting in a specific group delay (indicated by orange, green and blue vertical lines). The extent of pulse chirp can be controlled by the grating distance L_g .

2.1.2 Dispersion & pulse shaping

When light passes a medium, it experiences dispersion of the refractive index $n(\lambda)$. Angular dispersion is well known when sunlight passes a prism and gets split into different directions depending on the wavelength. The frequency dependence of the refractive index further manifests itself in a group delay dispersion, i.e., different frequencies take different times to pass the same medium. While this marginally affects continuous wave laser light, it has a distinct impact on ultrashort laser pulses.

Laser pulses with a single wavelength λ_0 , or equal frequencies within a pulse pass a medium within the timespan [cf. Eq. (2.10)]:

$$\phi' = T_g = \frac{\ell}{v_g} = \frac{\partial k}{\partial \omega} \ell = \frac{1}{c} \left(n - \lambda_0 \frac{\partial n}{\partial \lambda_0} \right) \ell, \quad (2.12)$$

where c is the speed of light in vacuum, v_g the group velocity, k the wavenumber and ℓ the thickness of the medium. The quantity T_g is commonly termed as group delay. Furthermore, the influence of dispersion on a laser pulse with an extended spectrum can be described by the group delay dispersion (GDD):

$$\phi'' = GDD = \frac{\partial^2 k}{\partial \omega^2} \ell = \frac{\partial}{\partial \omega} \frac{\ell}{v_g} = \frac{\lambda_0^3}{2\pi c^2} \frac{\partial^2 n}{\partial \lambda_0^2} \ell. \quad (2.13)$$

This equation obviously considers the second order derivative of the refractive index. It should be mentioned that even higher order dispersion can emerge. The GDD must be added to the spectral phase $\phi(\omega)$ as depicted by Eq. (2.10). Via performing the Fourier transform, its effect on the temporal pulse shape can be obtained [cf. Fig. 2.1].

When the Fourier-limited pulse duration Δt_0 of a Gaussian-shaped pulse is known, the pulse broadening due to GDD can be calculated with the following equation:

$$\Delta t = \sqrt{\Delta t_0^2 + \left(4 \ln 2 \frac{\phi''}{\Delta t_0} \right)^2}. \quad (2.14)$$

Inversely, the pulse duration Δt can be used to estimate the magnitude of ϕ'' . A comparable relation can be derived considering the bandwidth Δt to obtain the frequency chirp $\dot{\omega}$.

$$\dot{\omega} = \frac{\Delta\omega}{\Delta t} \sqrt{1 - \left(\frac{\Delta t_0}{\Delta t}\right)^2} \quad (2.15)$$

In the following experiments, the frequency dependence $\omega(t)$ is varied to set up a well defined frequency chirp and pulse duration Δt . Therefore, the angular dispersion from a grating and/or prism setup is utilized to introduce a particular negative value of ϕ'' [Fig. 2.2]. On the contrary, the value of ϕ'' from material dispersion (*GDD*) can only be positive.

2.2 Lithium niobate

This section gives an overview of the nonlinear optical medium lithium niobate. Its properties are summarized before the known processes of grating recording and dependencies from grating parameters are shown. An overview of the crystal structure of lithium niobate (LiNbO_3) and small polarons in it is given in references [14, 22, 23].

2.2.1 Nonlinear optical properties

In a z-scan setup, a single beam experiment, the two-photon absorption (TPA) and electro-optical Kerr-effect can be measured simultaneously. For a wavelength of $\lambda = 532 \text{ nm}$ and a picosecond pulse duration coefficients of two-photon absorption $\beta = 0.25 \text{ cm/GW}$ and nonlinear refraction $n_2 = 5.3 \times 10^{-6} \text{ cm/GW}$ are reported [13]. Both, two-photon absorption as well as optical Kerr-effect are a near-instantaneous response of the optical medium from third order susceptibility $\chi^{(3)}$.

In a pump-probe setup the pronounced two-photon absorption is studied with femtosecond pulses of different wavelengths in reference [24]. Therein, a TPA coefficient of $\beta = 3.5 \text{ cm/GW}$ is obtained for a wavelength of $\lambda = 388 \text{ nm}$. They also identify a long lasting absorption plateau with a small polarization dependence [25]. In addition, the authors point to an influence of the pulse duration on the obtained two-photon absorption coefficient, because the measurements can be distorted by additional absorption from photo-generated small polarons.

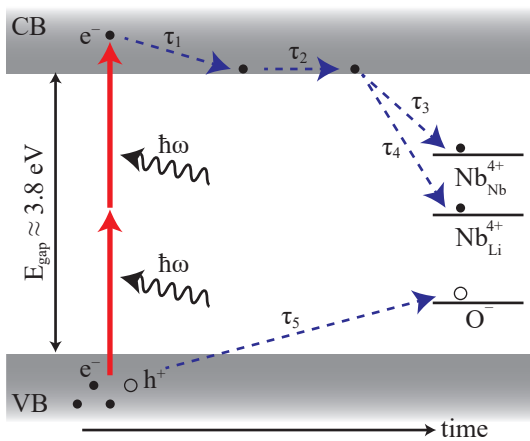


Figure 2.3: Scheme of the excitation process in lithium niobate. Formation of bound and free small polarons with time constants $\tau_1 - \tau_4$ according to reference [17] and, added, the formation of hole polarons with a time constant τ_5 . The subsequent excitation of the generated polarons becomes visible as a long-lasting absorption.

Two-photon absorption causes the transition of an electron from the conduction to the valance band. Based on the description by Qiu *et al.* [17] the formation process of polarons is depicted in Fig. 2.3. After the initial excitation, the hot electron undergoes a relaxation due to scattering from phonons until it reaches the bottom of the conduction band. Then, it localizes onto a distorted site in the lattice, which is commonly described as a small polaron. Eventually, the polaron energy decreases by vibration relaxation into a meta-stable state. The time constant of the formation process is not definitely specified yet, but it is indicated to be in the order of 10^{-13} s [17, 18]. This model was successfully applied to describe the formation of small free polarons in the mid-infrared [26].

Polaronic states [27] are identified and investigated in lithium niobate in several publications [28–33]. Different small polarons are distinguishable by characteristic absorption bands and relaxation dynamics [34]. In the mentioned references, the relaxation is most often described by a stretched exponential function or KWW function (Kohlrausch-Williams-Watts function) yielding two parameters, the decay constant τ_{KWW} and the stretching factor β_{KWW} :

$$A(t) = \sum_{i=1}^N A_i \exp \left(- (t/\tau_{KWW,i})^{\beta_{KWW,i}} \right) . \quad (2.16)$$

The sum in this equation represents multiple relaxation paths. The stretched exponential dynamic is related to a hopping-transport of the polarons [35]. Different recombination time constants between $10^{-7} - 10^2$ s at room temperature are reported. Both, formation and relaxation dynamics after femtosecond pulse excitation are comprehensively studied in references [18, 19, 36]. By fitting a single stretched exponential function, they reveal a decrease of the decay constant and the stretching factor when increasing the pump intensity [19, 36]. A saturation of photo-generated polarons is not observed [18].

Phonon modes in lithium niobate are studied by Raman measurements and are assigned to particular modes of the crystal structure [37–39]. The Raman spectra depend on the polarization setup and show multiple peaks within the wavenumber interval $\nu = (100 - 1000) \text{ cm}^{-1}$.

2.2.2 Grating recording

The interference of two coherent waves with equal polarization results in a fringe pattern, which can be transferred into the medium by its nonlinear optical response. Such holographic gratings are characterized by a modulation of the absorption (amplitude gratings) or the index of refraction (phase gratings). Commonly, a signal and reference beam are used to record a long lasting holographic grating, whereas the signal beam can be turned off when reading the grating with the reference beam. Alternatively, an additional beam is introduced at the Bragg-angle to permanently monitor its diffraction [Fig. 2.4(a)]. When using different wavelengths of the recording waves, the fringe pattern is not stationary, which inhibits the recording of a grating [Fig. 2.4(b)] [40].

For volume holographic gratings the diffraction efficiency is derived from coupled wave theory for amplitude and phase gratings, and is shown to be proportional to

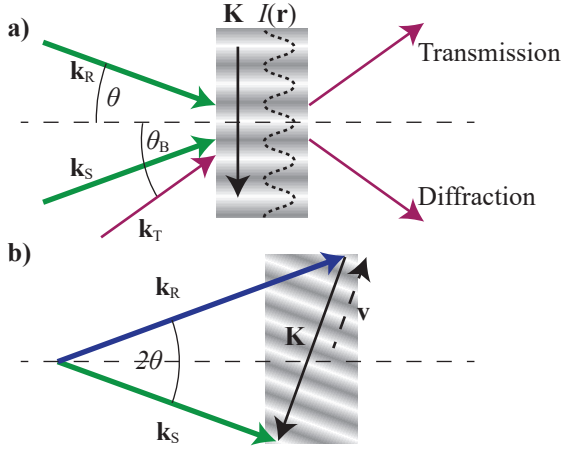


Figure 2.4: Principle of grating recording with (a) two identical beams and (b) two frequency detuned beams. The interference pattern $I(r)$ is marked as gray to white shaded areas. The grating vector $\mathbf{K} = \mathbf{k}_R - \mathbf{k}_S$ can be constructed from the incident wave vectors of the signal and reference beam with a symmetric angle of incidence θ . A readout beam \mathbf{k}_T impinges onto the sample under the Bragg angle θ_B . For different wavenumbers $|\mathbf{k}_S| \neq |\mathbf{k}_R|$ of the signal and reference beam the grating becomes tilted and performs a lateral movement with a velocity v .

the square of the modulation of the refractive index Δn and the absorption $\Delta\alpha$ [41]:

$$\eta = \left[\sin^2 \left(\frac{\pi \Delta n d}{\lambda \cos \theta_B} \right) + \sinh^2 \left(\frac{\Delta \alpha}{2 \cos \theta_B} \right) \right] \cdot \exp \left(- \frac{2 \alpha d}{\cos \theta_B} \right). \quad (2.17)$$

The dynamic processes and wave mixing that occur when the two recording waves are interacting with the nonlinear medium and the holographic grating are described in [40, 42, 43]. This can result in self-diffraction and energy redistribution [44, 45].

In lithium niobate efficient photorefractive grating recording is observed, especially in iron doped crystals [11, 12, 46, 47]. Electrons and holes are generated by light exposure and the electrons move to areas with no illumination due to the directional bulk photovoltaic effect. Subsequently an internal electric field (space charge field) is build-up between the separated charges. This, however, leads to a modulation of the refractive index by the electro-optical effect, that results in high diffraction efficiencies from a pure phase grating. The long-lasting holographic gratings are suitable for data storage, but are also thermally reversible [11, 12]. Recording is also possible with pulsed laser light and less irradiation, revealing a fast response of the material [46]. Gratings based on different physical origins are analyzed, underlining a dominant role of the photorefractive nonlinearity [47].

Besides the prominent photorefractive effect, efficient grating recording is possible due to the density modulation of small polarons after excitation with nanosecond laser pulses [48, 49]. Gratings from the near-instantaneous nonlinearities, optical Kerr effect and two-photon absorption, are deduced from measurements with femtosecond pulses [15, 20]. They are marked by a peak of the diffraction efficiency during the overlap of the reading pulse with the excitation pulses. A much weaker diffraction efficiency lasts for more than one nanosecond after the excitation, which is attributed to the photo-generation of excited carriers [20]. The analysis of the grating from free carrier reveal an adiabatic correlation between the absorbed energy from two-photon absorption and the buildup of the diffraction efficiency [15]. Peak values of the diffraction efficiency are obtained with amplitudes in the order of 10^{-3} in [20] and in the order of 10^{-4} and 10^{-7} for optical Kerr effect and free carrier in [15].

Chapter 3

Ultrafast absorption spectroscopy

When studying the interaction between femtosecond laser pulses and the nonlinear response of the lithium niobate crystal, first of all the absorption is of interest. In the following section the initial two-photon absorption and the absorption from photo-generated polarons are analyzed. Therefore, the influence of different pulse durations of the excitation pulse as well as spectral and temporal absorption characteristics of polarons are investigated.

3.1 Z-Scan with different pulse durations

The author contributed to the following article which studies the interplay between polaron absorption and the two-photon absorption coefficient. The abstract is printed here with the friendly permission of the *Optical Society of America* (OSA). The complete article can be found in the attachment [A.1](#).

- H. Badarre, S. Nolte, F. Freytag, P. Bäune, V. Dieckmann and M. Imlau.
Scanning nonlinear absorption in lithium niobate over the time regime of small polaron formation,
Opt. Mater. Express **5**, 2729–2741, (2015); doi: 10.1364/OME.5.002729.

Abstract: Nonlinear absorption is studied in presence of small polaron formation in lithium niobate using the z-scan technique and ultrashort laser pulses with pulse durations of (70 – 1,000) fs. A model for the analysis of the transmission loss as a function of pulse duration is introduced that considers (i) the individual contributions of two-photon and small polaron absorption, (ii) the small polaron formation time and (iii) an offset time between the optical excitation of free carriers by two-photon absorption and the appearance of small polarons. It is shown that the model allows for the analysis of the experimentally determined z-scan data with high precision over the entire range of pulse durations using a two-photon absorption coefficient of $\beta = (5.6 \pm 0.8)$ mm/GW. A significant contribution by small polaron absorption to the nonlinear absorption is uncovered for pulse durations exceeding the characteristic small polaron formation time of ≈ 100 fs. It can be concluded that the small polaron formation time is as short as (70 – 110) fs and the appearance of small polaron formation is delayed with respect to two-photon absorption by an offset of about 80 fs.

3.2 Transient absorption with ultrafast white light supercontinuum

3.2.1 Experimental technique

The light-induced absorption from a strong excitation pulse is monitored by a broadband white light probe pulse in a common pump-probe setup. Whereas the excitation pulse is simply focused on the sample, the generation of the white light supercontinuum (WLC) needs some explanation. The output energy from the laser system (*Coherent Astrella*) with a wavelength of $\lambda = 800$ nm and pulse durations $\Delta t \approx 35$ fs is reduced to a few μJ . When focusing the beam onto a crystal as sapphire (Al_2O_3) or calcium fluoride (CaF_2), a laser filament due to self-focusing can be carefully adjusted by both a variable attenuator and an aperture [cf. Fig. 3.1]. Besides that, self-phase modulation causes an extension of the bandwidth towards the majority of the visible spectral region. Sapphire offers a white light continuum in the wavelength range $\lambda = (420 - 720)$ nm, and calcium fluoride in the wavelength range $\lambda = (290 - 720)$ nm [50]. Naturally, the spectrum also covers the fundamental wave at $\lambda = 800$ nm and is extended to the infrared as well. However, only the visible spectral range is under investigation in the following experiments and filters are used to suppress the wavelengths $\lambda > 700$ nm.

Behind the sample the white light probe is monitored with a fiber-coupled spectrometer (*PI, Isoplane SCT 320, PIXIS camera*). Baseline spectra $I_0(\lambda)$ are used to normalize the transmitted intensity with a pump pulse $I(\lambda)$ to obtain the light-induced absorption of the sample. Both are corrected by background spectra. The change of transmission $T(\lambda) = I(\lambda)/I_0(\lambda)$ is used to define the absorbance $A(\lambda)$ or equally called optical density:

$$A(\lambda) = -\log_{10}(T(\lambda)) = -\log_{10}(I(\lambda)/I_0(\lambda)) . \quad (3.1)$$

Deliberately, it is avoided to use the absorption coefficient $\alpha = A/d$ because the sample thickness d does not need to coincide with an effective absorption thickness from nonlinear absorption. The light-induced absorption decreases with the propagation coordinate as well as the intensity due to linear and two-photon absorption. Time-resolved spectra are received by a temporal delay τ between the pump and the probe pulses when changing the path length with a delay line. The repetition rate of the laser system is reduced to 10 Hz to suppress accumulated effects. The pump pulse is obtained from the fundamental wave either immediately by second harmonic generation (SHG) at $\lambda = 400$ nm or by using an optical parametric amplifier (OPA) at $\lambda = 540$ nm. The beam diameter at the sample position is adjusted via its distance to the spherical mirrors so that the pump spot is bigger than the probe spot. The polarization of the pump \mathbf{e}_P and of the white light continuum \mathbf{e}_C are marked in each measurement with respect to the polar axis \mathbf{c} of the lithium niobate crystal.

Additionally, a continuous wave laser with a wavelength of $\lambda = 632$ nm is focused onto the sample to record the light-induced absorption between tens of nanoseconds and seconds. The transmitted intensity is recorded with a silicon diode and a digital oscilloscope, that is triggered by another diode detecting the pump pulse.

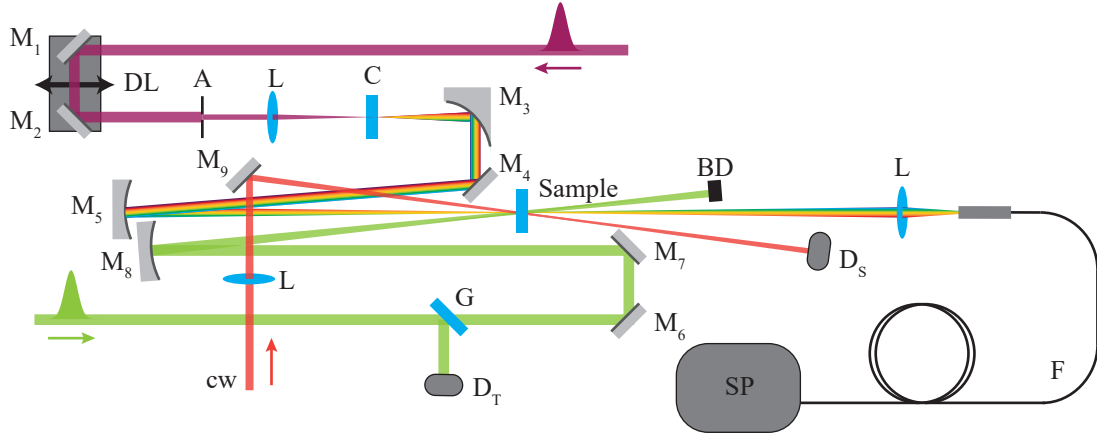


Figure 3.1: Scheme of the experimental setup for femtosecond transient absorption measurements with a white light supercontinuum probe pulse. The 800 nm probe pulse (purple) passes an optical delay line (DL), an aperture (A) and a lens (L) to become focused inside a crystal (C) for white light generation. The divergent white light supercontinuum is collimated by an off-axis parabolic mirror M_3 . The spherical mirrors M_5 and M_8 respectively focus the white light and the excitation pulse (green) onto the sample. $M_{1,2,4,6,7,9}$ are plane mirrors, BD is a beam dump, and another lens (L) focuses the white light onto an optical fiber (F) that transmits it into a spectrometer (SP). A continuous wave laser (red) is focused with a lens (L) onto the sample as well to monitor its transmission with a silicon diode D_s and a digital oscilloscope, which is triggered by the pump pulse reflection from a glass plate (G) and another diode D_T .

3.2.2 Experimental results

Relaxation dynamic

First, the absorption spectrum of congruent, nominally undoped lithium niobate (cLN) is investigated with different temporal delays τ between pump and probe pulses. For large pulse delays $\tau \gg 10$ ps a lateral shift of the beam spot on the sample, due to a minimal distortion of the delay line, is observed. Therefore, it is necessary to readjust the spatial overlap of the beams to achieve the maximum change of transmission for each particular temporal delay. Despite this restriction

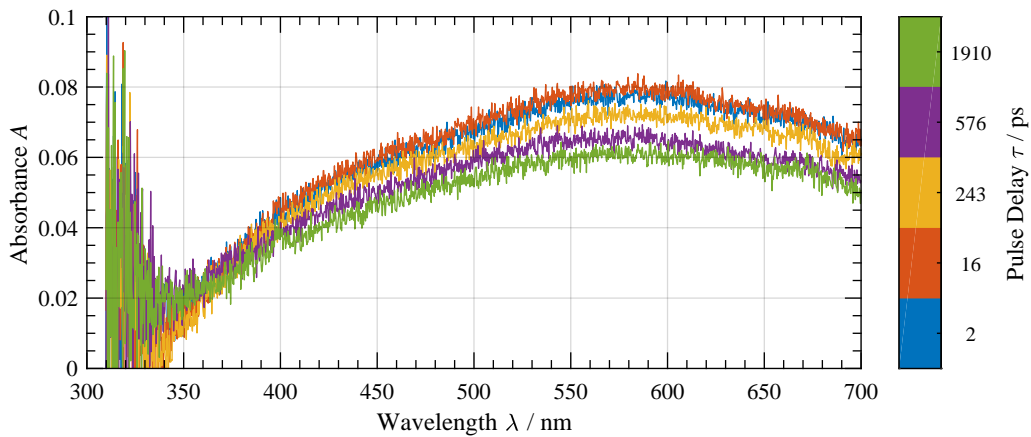


Figure 3.2: Absorbance spectrum $A(\lambda)$ of congruent, nominally undoped lithium niobate ($d = 280 \mu\text{m}$) recorded with a white light probe from calcium fluoride and pump pulses at $\lambda = 400 \text{ nm}$. The polarization is set to $\mathbf{e}_P \parallel \mathbf{c}$ and $\mathbf{e}_C \perp \mathbf{c}$. The data in different colors denote the pulse delay τ .

of accuracy, a temporal trend can be clearly seen for the data depicted in Fig. 3.2. The excitation wavelength of $\lambda = 400$ nm is used in these measurements with a pulse duration of $\Delta t < 100$ fs. The results show a spectral broad absorption band covering the complete measuring range with a maximum between $\lambda = (550 - 600)$ nm. In a qualitative comparison with the known absorption bands from reference [34], it could be interpreted as the combined absorption from hole, free and bound polarons.

To identify polaronic states commonly the relaxation dynamic is analyzed to fit it with a stretched exponential function according Eq. (2.16). The results from a continuous wave laser at $\lambda = 632$ nm are depicted in Fig. 3.3 together with the absorbance evaluated from the data in Fig. 3.2 for the same wavelength. Only the cw data are used to fit stretched exponential functions with $N = 1$ (red) and $N = 2$ (black) and with the depicted parameters for amplitudes A_i , decay constants τ_{KWW} and stretching factors β_{KWW} . In Fig. 3.3 one can observe that the fit of a single function (red) deviates from the measured data, which is highlighted with red circles. In contrast, a two-fold function (black) coincides well with the experimental data from the cw laser. Compared with the femtosecond white light probe data, the latter fit function appears to be systematically larger. However, no scaling correction is applied between both detection methods in the presented results, which would ensure continuous amplitudes as it is done in other publications [19, 36]. An offset between the femtosecond and cw probe data might be caused by different beam diameters/profiles of the probe beams in relation to the excitation pulse.

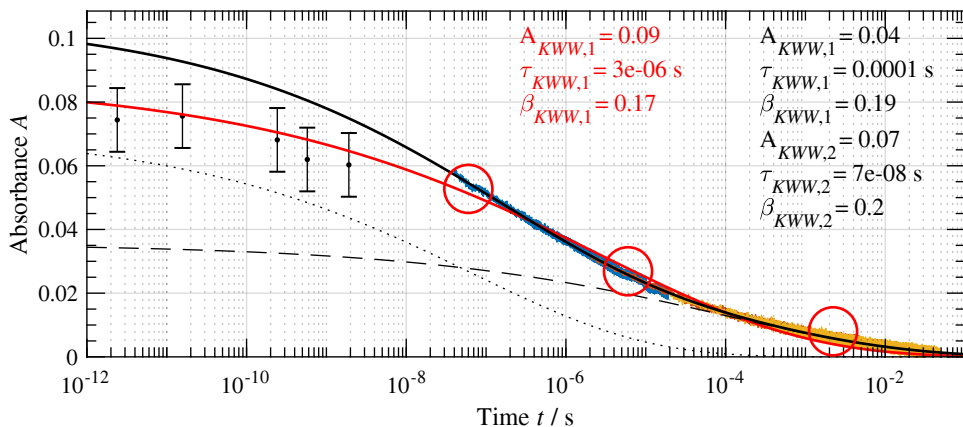


Figure 3.3: Temporal dependence of the absorbance $A(t)$ in congruent, nominally undoped lithium niobate ($d = 280 \mu\text{m}$) after femtosecond excitation with $\lambda = 400$ nm pump pulses at a probe wavelength of $\lambda = 632$ nm. The polarization is set to $\mathbf{e}_P \parallel \mathbf{c}$ and $\mathbf{e}_C \perp \mathbf{c}$. The black dots with errorbars indicate the data from the previous experiment shown in Fig. 3.2. The blue, orange and yellow data are recorded with a cw laser and an oscilloscope. Solid red and black lines indicate single and two-fold stretched exponential functions fitted to the cw data with the shown parameter according to Eq. (2.16). The dashed and dotted black lines depict the two partial functions from the solid black fit. The red circles highlight the deviation between the red fit function and the data.

Excitation dynamic

The following measurements focus on a shorter timescale of a few picoseconds around the excitation pulse. For that, the position of temporally synchronized pulses and zero pulse delay $\tau \approx 0$ is arbitrary set to the region of strongest and persistent change of the absorbance. The results are depicted in Fig. 3.4 and reveal another feature of

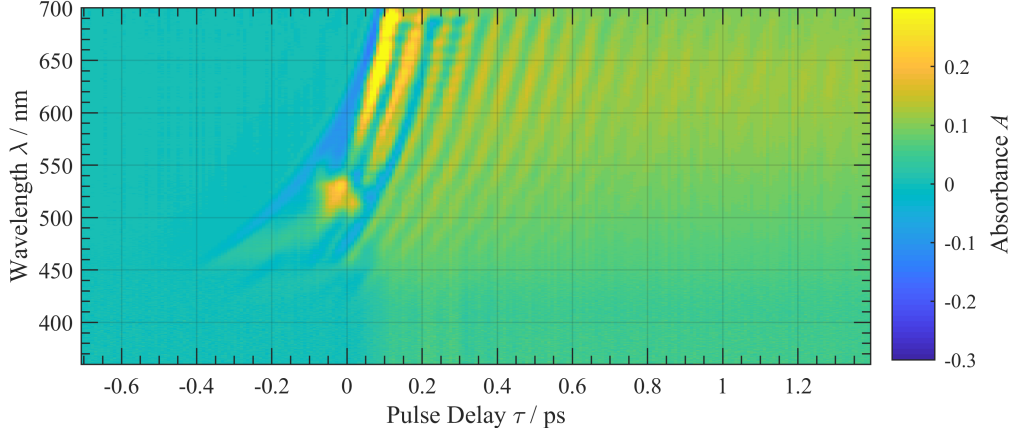


Figure 3.4: Absorbance spectrum $A(\lambda, \tau)$ recorded with a white light probe from sapphire and pump pulses at $\lambda = 540$ nm, with polarizations set to $\mathbf{e}_P \perp \mathbf{c}$ and $\mathbf{e}_C \perp \mathbf{c}$ in congruent, nominally undoped lithium niobate ($d = 280$ μm). The absorbance is clipped to an interval $-0.3 < A < 0.3$ to increase the contrast. The pulse duration of the pump is $\Delta t \approx 30$ fs measured by intensity autocorrelation.

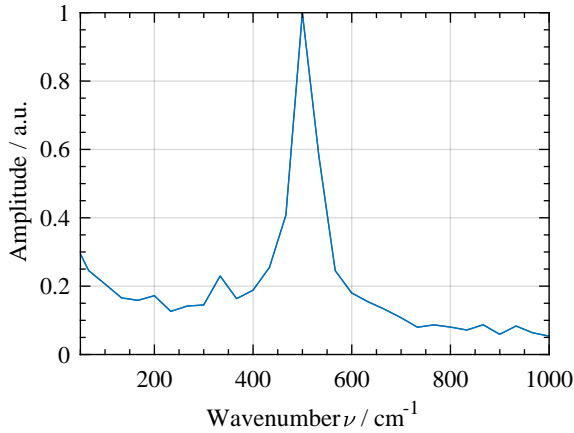


Figure 3.5: Fourier transform of the data in Fig. 3.4 in the range $\tau = (0.25 - 1.25)$ ps and $\lambda = (400 - 750)$ nm. The maximum is obtained for a wavenumber of $\nu_{\text{max}} \approx 500$ cm^{-1} which corresponds to an angular frequency of $\omega \approx 9.4 \times 10^{13}$ rad/s.

the congruent, nominally undoped lithium niobate sample. Oscillations can be seen clearly for positive pulse delays $\tau > 0$ between wavelengths of $\lambda = (450 - 700)$ nm. To increase the visibility and increase the contrast, the absorbance is clipped to an amplitude of $|A| < 0.3$. The maximum, however, reaches ≈ 0.7 (bright yellow in the vicinity of zero pulse delay), what could be related to two-photon absorption. Prior this negative absorbance values down to ≈ -0.3 (dark blue) are remarkable, indicating an increase of the transmitted light. One also can see a color change from green-blue to yellowish around zero pulse delay in the complete measured spectral region. This illustrates the light-induced absorption, i.e., the photo-generation of small polarons [cf. Fig. 3.2]. In the measured data of Fig. 3.4, lines of equal magnitudes systematically reveal similar curvatures that originate from the frequency chirp of the white light continuum [50].

To analyze the oscillations visible in Fig. 3.4, a Fourier transform of the data in the range $\tau = (0.25 - 1.25)$ ps and $\lambda = (400 - 750)$ nm is performed. The results depicted in Fig. 3.5 reveal a main frequency of $\nu = 500$ cm^{-1} in wavenumbers. Because the oscillations are strongly damped, so that they are visible for roughly a picosecond, the resolution of the Fourier transform is limited. Furthermore, a trace for a single wavelength of the spectrum is plotted in Fig. 3.6 to fit the exponential damping in

the first instance. The overall fit function $T(\tau) = T_1(\tau) \cdot T_2(\tau) \cdot T_3(\tau)$ consists of three parts:

$$T_1(\tau) = 1 - \frac{A}{2} \cdot \left[1 + \operatorname{erf} \left(\sqrt{4 \ln 2} \cdot \frac{\tau}{\Delta t} \right) \right], \quad (3.2)$$

$$T_2(\tau) = 1 - B \cdot \exp \left(-\frac{\tau}{C_1} \right), \quad (3.3)$$

$$T_3(\tau) = \sin \left(\phi(\tau) + \phi_0 \right), \quad (3.4)$$

$$\phi(\tau) = \int \omega_0 + \omega_1 \left[1 - \exp \left(-\frac{\tau}{C_2} \right) \right] d\tau. \quad (3.5)$$

The first term represents the absorption change of the sample due to the excitation of small polarons. Assuming that change of the persistent absorbance is faster than the pulse duration, the width of the fitted error function is set to the pulse width of the excitation pulse Δt . The parameter A describes the transmission change from unity. In the second term the exponential damping is characterized by a constant C_1 and starting amplitude B . The third equation denotes periodic oscillations with an angular frequency ω . Purely phenomenologically, a temporal change of the frequency is included to fit the data more reliable. In doing so the main frequency $\omega = \omega_0 + \omega_1 \approx 9.4 \times 10^{13}$ rad/s [Fig. 3.5] is reached after fractions of a picosecond. Oscillations with a wavenumber of $\nu \approx 500$ cm $^{-1}$ and a damping constant of ≈ 200 fs are determined.

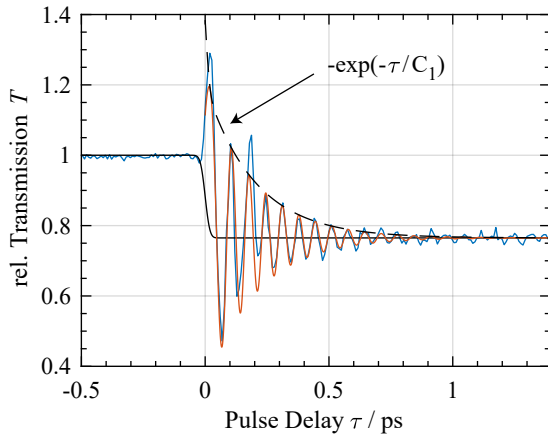


Figure 3.6: Pulse delay dependence of the relative transmission T from data of Fig. 3.4 at a wavelength of $\lambda = 622$ nm (blue). The other lines show different fit functions shifted to unity: solid black - error function according pump pulse duration and absorption plateau $T_1(\tau)$; dashed black - exponential function with time constant $C_1 \approx 200$ fs multiplied by the previous function $T_2(\tau) \cdot T_1(\tau)$; red - sine wave multiplied by the dashed function $T(\tau) = T_3(\tau) \cdot T_2(\tau) \cdot T_1(\tau)$ [see Eqs. (3.3)-(3.5)] with $C_2 \approx 60$ fs.

3.2.3 Discussion

The presented results of transient absorption qualitatively correspond with references [18, 19, 36]. After the excitation by a femtosecond laser pulse an absorption plateau can be observed that covers the entire visible spectrum [Figs. 3.2 and 3.4]. It can be related to the photo-generation of small polarons via two-photon absorption. In the references the TPA becomes visible as a pronounced dip in the probe pulse transmission during the temporal overlap with the pump pulse when one photon of each pulse is absorbed together. Although, it cannot be identified distinctly in the results in Fig. 3.4 with an excitation wavelength of $\lambda = 540$ nm, it is more clearly visible at zero pulse delay for a 400 nm pump pulse (not shown). The weaker two-photon absorption is supported by the dispersion of the two-photon absorption coefficient reported in reference [24]. Nevertheless, therein the values are reported for the absorption of two photons with equal energy, while here the pump and probe photons

can possess different energies. For investigating the relaxation dynamic of the photo-generated polarons, a stretched exponential decay is fitted to the data of Fig. 3.3 for a two-center relaxation according to reference [29]. The obtained parameters of the stretching factor $\beta = 0.17$ and the time constant $\tau \approx 10^{-6}$ s coincide with the references [18, 19, 36]. Both values are smaller than in the case of nanosecond pulse excitation, which were assigned to large polaron densities from high intensities and short pulse durations within these publications. Comparing the fit function with the measured data, small, systematical deviations become visible. Therefore, a two-fold decay function is fitted to the data as well. In doing so, the agreement between fit and experimental data is clearly improved. The time constants suggest a slow decay with $\tau_1 \approx 10^{-4}$ s and a fast decay with $\tau_2 \approx 10^{-8}$ s. It is established that bound polarons recombine with hole polarons (GP-HP), typically showing a single stretched exponential decay [18, 19, 29, 36]. The second contribution might originate from a recombination of free polarons with hole polarons (FP-HP), which should be faster than the previously mentioned one. Their formation and relaxation process is already reported in magnesium doped lithium niobate [18, 26]. Assuming both electron polarons recombine with hole polarons, the number density of the latter is always higher than that of the other two. To evaluate the amplitudes of the two fit functions at the investigated wavelength of $\lambda = 632$ nm, the cross-sections reported in reference [34] are simply added for this two recombination paths:

$$\sigma_{\text{GP-HP}} \approx 7.4 \times 10^{-22} \text{ m}^2 , \quad (3.6)$$

$$\sigma_{\text{FP-HP}} \approx 3.6 \times 10^{-22} \text{ m}^2 . \quad (3.7)$$

A rough estimate of the ratio between free and bound polarons can be derived from the amplitudes A_1 and A_2 of the fit function and these cross-sections:

$$\frac{A_1/\sigma_{\text{GP-HP}}}{A_2/\sigma_{\text{FP-HP}}} \approx 0.3 . \quad (3.8)$$

This value denotes that with the shown experimental conditions there might be 3-4 times more free polarons than bound polarons during the first picoseconds. Based on the presented evaluation, free polarons should be considered even in congruent, undoped lithium niobate. To be certain, the magnitude of the absorption measured by femtosecond pulses needs to coincide with the fit function. By carefully adjusting equal beam diameters of the different probe beams, femtosecond and cw data should be equally scaled. Afterwards, an influence of the wavelength and/or the pulse duration of the pump pulse on the polaron ratio might be observed.

Combining the cross-sections of the different polaron species [34] with the above mentioned polaron ratio, the absorption from hole polarons should be dominant in the visible spectral range. Indeed, the absorption spectra depicted in Fig. 3.2 have a maximum between the wavelengths $\lambda = (550 - 600)$ nm, which supports such a statement. The absorption from free polarons might unambiguously be seen when extending the measurements to the infrared, i.e., a photon energy where their absorption cross-section is maximal [26]. Nevertheless, hole polarons associated to the recombination of free polarons are already recorded in the visible.

Within a short time window after excitation with a femtosecond laser pulse at $\lambda = 540$ nm and a pulse duration of $\Delta t \approx 30$ fs, pronounced oscillations are observed [Fig. 3.4]. Similar results in white light transient absorption experiments in a different

material are accounted to impulsive stimulated Raman scattering [50]. Details of this phenomenon can be found in several references [51–55]. Due to the short pulse duration, phonon modes can be excited coherently from difference-frequency generation from different wavelengths within the bandwidth of one pulse. The superposition of these single vibrations can result in an observable oscillation. In theory, a decay is reported when the phonons become dephased. Regularly, changes of the refractive index from the coherent phonons are measured by analyzing the light polarization, which changes due to a light-induced birefringence.

In the present experiment, however, the absorbance is modulated. It might originate either from an actual change of the absorption or from changes of the refractive index and Kerr-lensing. The second effect would only become visible when the analyzed beam is spatially clipped, what might be possible due to the small aperture of the used fiber. One could also assume that the coherently driven phonons can be related to an index modulation along the direction of pulse propagation, i.e., they can act as a phase grating with a grating vector parallel to the wave vector of the pump pulse. This would diffract the white light continuum probe pulse backwards, so that its transmission gets decreased. When altering the delay of the probe pulse, it could experience either maxima or minima of the oscillating modulation. A different explanation can be related to a coupling between polarons and phonons, that might either result in a dynamic of the refractive index or the absorption. This explanation is supported by the visibility of oscillations in the entire long-lasting absorption plateau of the polarons. The obtained terahertz frequency suggests a phononic origin, however, no phonon modes are reported for a wavenumber of $\nu = 500 \text{ cm}^{-1}$ [37–39]. A dephasing of the phonons could result from scattering at defects or interactions with other phonons. In further measurements, the latter could be controlled by different temperatures of the sample, which might facilitate a long lifetime of the phonon coherence.

Chapter 4

Pulse interaction with self-induced and static gratings

After the previous overview of the nonlinear absorption including polaron dynamics, the pulse interaction with self-induced and static gratings is studied in the following. As the main part of this work, holographic gratings are investigated by analyzing self-diffraction, image recording, and energy transfer, especially in the case of two frequency detuned recording pulses. Thereby, the grating recording strongly depends on the pulse parameters: duration, bandwidth and frequency chirp. Therefore, this study begins with a detailed description of the pulse characterization from the frequency-resolved optical gating technique.

4.1 Frequency-resolved optical gating from self-diffraction

When using ultrashort laser pulses, it is essential to know the exact temporal profile and even more the frequency distribution within the pulse. One method to characterize the pulse is the *intensity autocorrelation* that gives access to the temporal profile by generating an intensity dependent signal from a nonlinear optical process. A complete characterization including the phase can be achieved by *frequency-resolved optical gating* (FROG) measurements, that were first proposed by Rick Trebino and Daniel J. Kane [56–58]. This technique extends the intensity autocorrelation to the measurement of the signal spectrum. A 3D spectrogram is obtained as the result of this measurement of the intensity in dependence on the temporal delay in one dimension and the frequency in the other. Basic features of this spectrogram can be intuitively evaluated, but a numerical, iterative *phase retrieval algorithm* is necessary for a complete characterization of the laser pulse [57].

In the following, the aim is to use the FROG-technique to get a detailed knowledge about the laser pulse itself and also to investigate if lithium niobate is a suitable medium for this kind of measurement because it features a pronounced Kerr-effect.

4.1.1 Experimental technique

Setting up an autocorrelation experiment needs only a few components: a beamsplitter, an optical delay line, a nonlinear medium and a detector [see Fig. 4.1]. Special

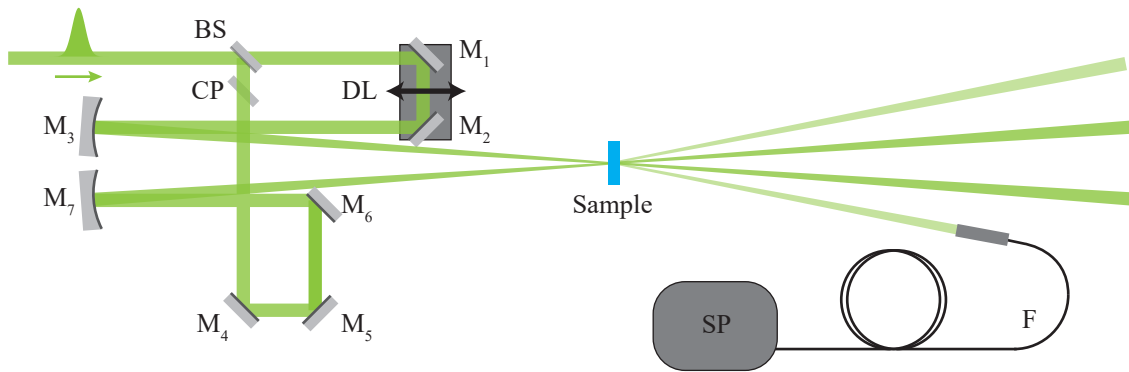


Figure 4.1: Scheme of the experimental setup for frequency-resolved self-diffraction measurements. The pulses impinge on a 50/50 beamsplitter (BS), an optical delay line (DL), a compensatory plate (CP), plane mirrors ($M_{1,2,4,5,6}$), spherical mirrors ($M_{3,7}$), and an optical fiber (F), which transmits the pulse into a spectrometer (SP).

interest is given to the splitting of the laser pulse in two identical parts, because the group velocity dispersion only affects the pulse that propagates through the beamsplitter. Therefore, a second plate similar to the beamsplitter material is put into the reflected pulse to compensate for the differences between reflection and transmission. The experiment is designed for the use of *self-diffraction*, which is based on the optical Kerr effect, a third order nonlinear process. To address this nonlinearity, high intensities are needed that are achieved by focusing the two beams with spherical mirrors. The spatial overlap is adjusted at a distance a few centimeters offside the focus, whereby the angle between the two beams is small $2\theta = 3.5^\circ$, and the medium is thin because the process of self-diffraction is not phase-matched. The optical delay line has a resolution of $ds = 0.1 \mu\text{m}$ that determines the maximum temporal resolution $d\tau \leq 1 \text{ fs}$ of the measurement. One can either use a photodiode for intensity autocorrelation measurements or a spectrometer for FROG measurements as a detection unit.

4.1.2 Phase retrieval algorithm

In the obtained spectrogram of the intensity, the phase information is not accessible. However, one can use an algorithm that varies the phase until the reconstructed data coincide with the measured results. For self-diffraction, a third order nonlinearity, the signal can be described by the following equations where τ is the pulse delay [56–58]:

$$E_{\text{sig}}(t, \tau) \propto E(t)^2 E^*(t - \tau) \quad (4.1)$$

$$I_{\text{FROG}}(\omega, \tau) = \left| \int_{-\infty}^{\infty} E_{\text{sig}}(t, \tau) \exp(-i\omega t) dt \right|^2. \quad (4.2)$$

These terms include the convolution of the squared electrical field of the pulse with its complex conjugate. The second operation is a Fourier transform to get the spectral content from the temporal domain.

The algorithm starts with a first guess for the pulse $E(t)$, which is used to calculate the signal field $E_{\text{sig}}(t, \tau)$. Second, the Fourier transform $E(\omega, \tau)$ is generated from this field. While containing the complex phase, the amplitude of the field is replaced by the square root of the measured spectrogram $\sqrt{I_{\text{FROG}}(\omega, \tau)}$. Third, the obtained field

is inversely Fourier transformed to get a new signal field $E'_{\text{sig}}(t, \tau)$, which is compared with the initial field $E_{\text{sig}}(t, \tau)$ to calculate a deviation Z from Eq. (4.3). The fourth step is to find a new pulse $E'(t)$ that minimizes Z for the next iteration. In general, this procedure is called *generalized projection* (GP) and it uses the gradient $\partial Z / \partial E(t)$ of the distance function:

$$Z = \sum_{i,j=1}^N \left| E'_{\text{sig}}(t_i, \tau_j) - E(t_i)^2 E^*(t_i - \tau_j) \right|^2 \quad (4.3)$$

The basic code from Trebino [59] was therefore adapted for self-diffraction measurements and optimized for Matlab2018a. The functionality is tested by numerically constructing a FROG spectrogram from an arbitrary pulse $E(t)$ according to Eq. (4.2) with a grid of $N \times N = 256 \times 256$ data points. In Fig. 4.2 the input pulse is depicted gray shaded and is characterized by the temporal profile, the derivative of the temporal phase, and the spectrum. By using the GP-algorithm the initial FROG spectrogram can be reconstructed with a good agreement of a remaining distance $Z < 10^{-7}$ within 1000 iterations. The reconstructed temporal and spectral pulse shapes are shown with blue lines that coincide well with the gray-shaded input.

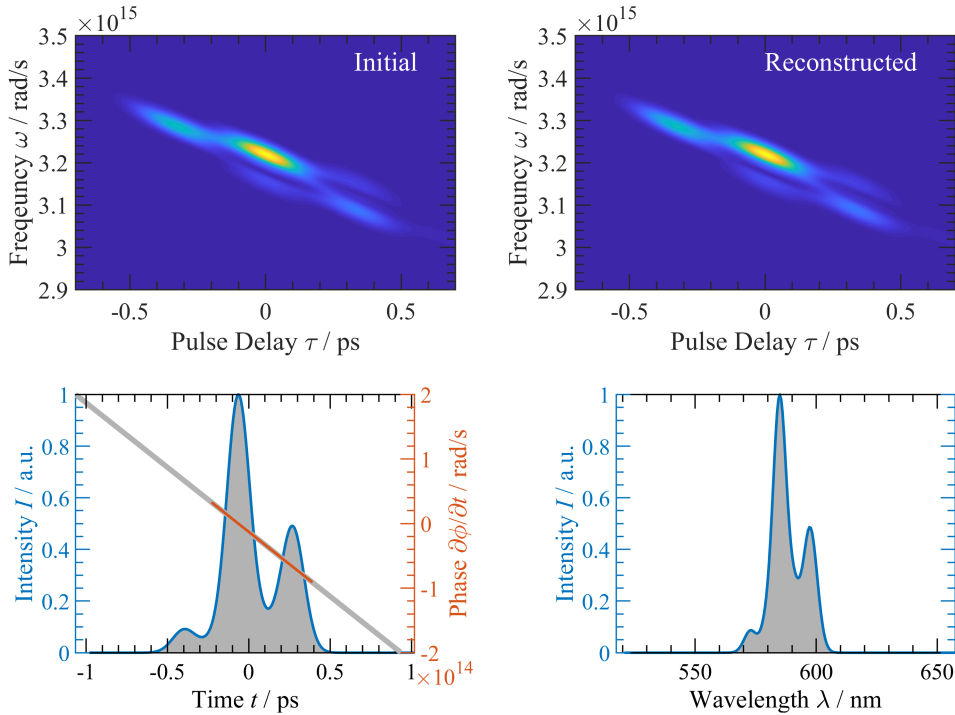


Figure 4.2: Test of the phase retrieval algorithm. A temporal pulse profile with a frequency chirp of $\partial\omega/\partial t = \partial^2\phi/\partial t^2 = -2 \times 10^{26} \text{ rad/s}^2$ at a central wavelength $\lambda_0 \approx 590 \text{ nm}$ and an according spectrum (all gray shaded) is used to calculate a FROG spectrogram (top left). The GP-algorithm is used with 1000 iterations to reconstruct the FROG spectrogram (top right) with temporal and spectral pulse profiles (blue lines) and the derivative of the temporal phase (red line). High intensities of the spectrogram are indicated by more yellowish colors.

4.1.3 Experimental results

The self-diffraction FROG from congruent, undoped lithium niobate is compared with the signal from dense flint glass (SFL6) or borosilicate glass (D263M). The sample thickness is smaller than $d \leq 300 \mu\text{m}$ to reduce the influence of group velocity dispersion, i.e., broadening of the pulse duration inside the medium. The measurements are done with a wavelength of $\lambda_0 \approx 540 \text{ nm}$ and two different pulse durations Δt . The latter was altered by the group velocity dispersion from a thick glass block.

Because lithium niobate shows a dependence on the light polarization \mathbf{E} , as well as on the orientation of the holographic grating vector \mathbf{K} in relation to the polar \mathbf{c} -axis, two different orientations are used: $E \perp c \parallel K$ and $E \parallel c \perp K$.

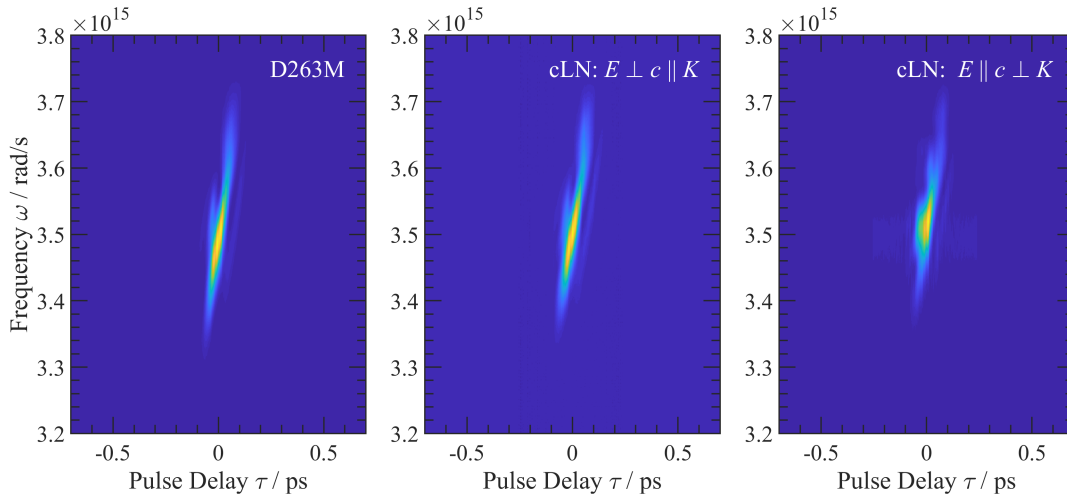


Figure 4.3: FROG spectrograms recorded from self-diffraction in a $200 \mu\text{m}$ thick D263M-glass and in a $280 \mu\text{m}$ thick congruent lithium niobate sample (cLN) at a central wavelength of $\lambda_0 = 540 \text{ nm}$ and a pulse duration of $\Delta t \approx 90 \text{ fs}$. High intensities of the spectrogram are indicated by more yellowish colors.

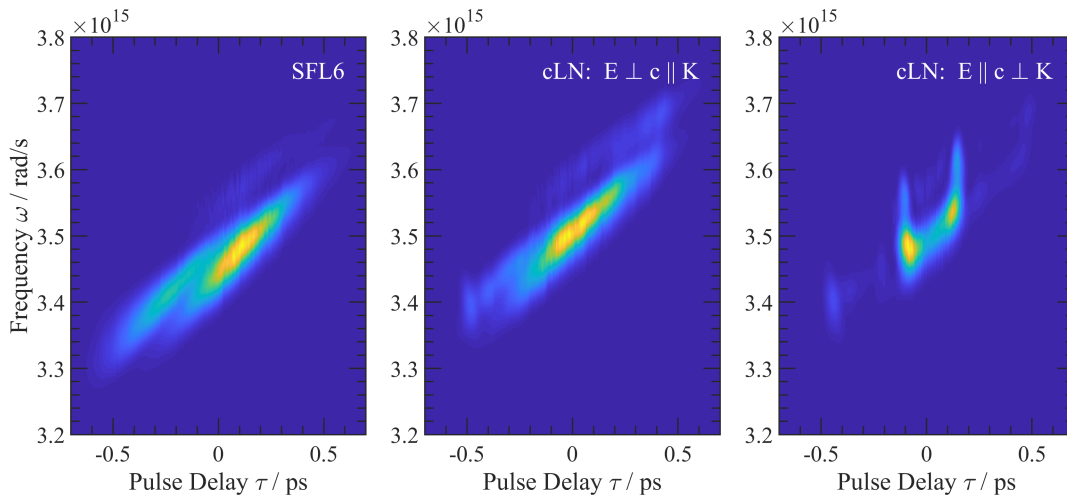


Figure 4.4: FROG spectrograms recorded from self-diffraction in a $180 \mu\text{m}$ thick SFL6-glass and in a $280 \mu\text{m}$ thick congruent lithium niobate sample (cLN) at a central wavelength of $\lambda_0 = 540 \text{ nm}$ and a pulse duration of $\Delta t \approx 610 \text{ fs}$. High intensities of the spectrogram are indicated by more yellowish colors.

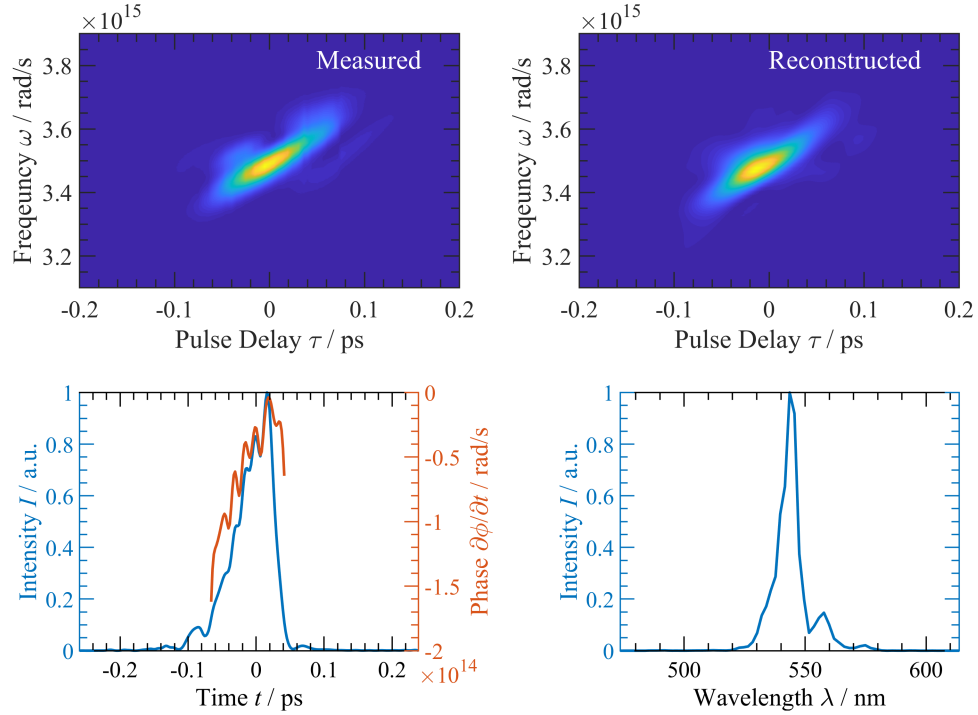


Figure 4.5: FROG spectrogram recorded from self-diffraction in a 200 μm D263M-glass with a central wavelength of $\lambda_0 = 540$ nm, with reconstruction of the temporal shape $I(t)$, phase derivative $\partial\phi/\partial t$ and its corresponding spectrum $I(\lambda)$. High intensities of the spectrogram are indicated by more yellowish colors.

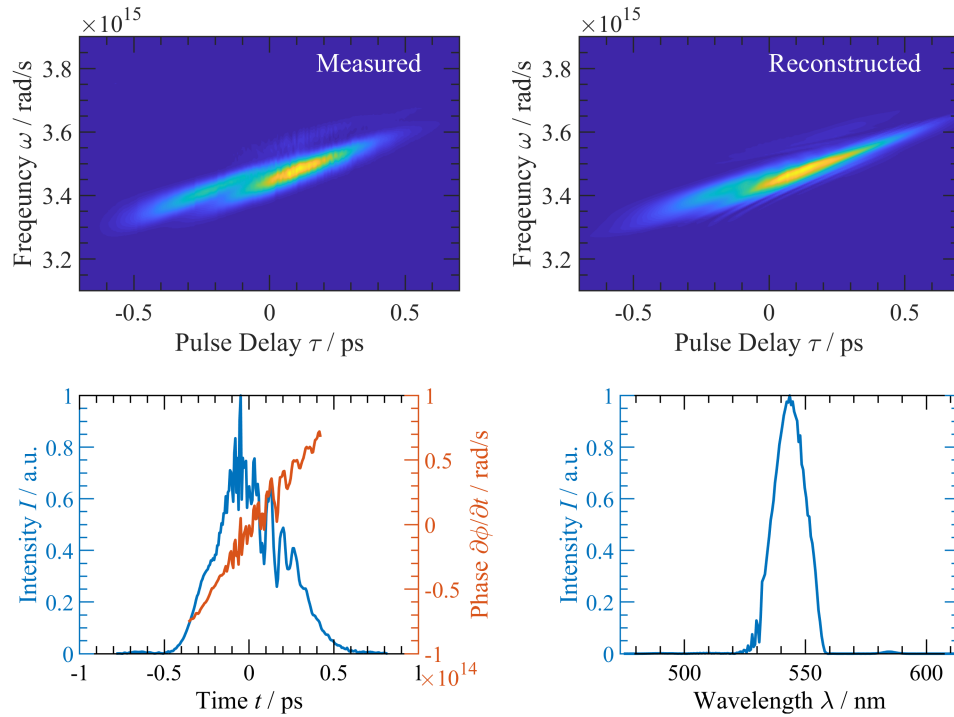


Figure 4.6: FROG spectrogram recorded from self-diffraction in a 180 μm SFL6-glass with a central wavelength of $\lambda_0 = 540$ nm, with reconstruction of the temporal shape $I(t)$, phase derivative $\partial\phi/\partial t$ and its corresponding spectrum $I(\lambda)$. High intensities of the spectrogram are indicated by more yellowish colors.

First of all, it is obvious that a shorter pulse causes a more narrow spectrogram [cf. Figs. 4.3 and 4.4]. All three measurements with short pulses are similar, while for longer pulses a distinct deviation becomes visible. For lithium niobate and the polarization setup $E \parallel c \perp K$ two areas with a signal stronger than the underlying diffraction signal can be observed at a pulse delay $|\tau| \approx 150$ fs. Two additional areas can be seen for larger pulse delays at $|\tau| \approx 450$ fs with a smaller contrast. The data from the second polarization setup $E \perp c \parallel K$ looks similar to the signal from the glass plate, although the above mentioned signal peaks are slightly visible as well. Different glasses are used for this measurements, however, the results only differ in their amplitude.

Because of these particularities in the spectrogram from lithium niobate, the data from the glass plates is analyzed with the phase retrieval algorithm to obtain the pulse shape. The results are depicted in Figs. 4.5 and 4.6. They show a good agreement between the initial and the reconstructed FROG spectrogram, but naturally this agreement is worse than the reconstruction of the test spectrogram. The deviation could originate from fluctuations of the pulse energy and pulse shape during the measurement, because several pulses are needed. Even after applying a noise reduction algorithm in the pulse delay dimension, the noise is clearly visible in the reconstructed pulse shape. Nevertheless, reasonable pulse shapes are obtained by the presented procedure.

4.1.4 Discussion

The results of the different samples can be well compared, because the transmission through the different optics and their GDD are preserved. Only the pulse energy is adapted to the strength of the nonlinear refraction, using a variable reflective neutral density filter. To obtain a preferably pure FROG measurement, media that only show a near-instantaneous Kerr-nonlinearity such as glasses are used. In contrast, lithium niobate is known for its metastable states such as small polarons, which can affect these measurements, leading to different results. Especially in Fig. 4.4, the deviation between glass and lithium niobate can be clearly seen when using slightly extended pulse durations. Therefore, it is consequent to conclude that lithium niobate is not suitable for FROG measurements even before applying the phase retrieval algorithm. It might be used with the polarization setup $E \perp c \parallel K$ with constraints, however, it is more appropriate to immediately use glass instead.

Nevertheless, a closer insight into the nonlinearities of lithium niobate is possible when using the pulse information gained from the FROG measurements in glass. For the further analysis, only the data for an extended pulse duration are used [cf. Fig. 4.4]. First, the spectrogram is integrated over the frequency to obtain a simple time dependent intensity $I(\tau)$ [Fig. 4.7(a)]. For a linear chirp the pulse delay τ is proportional to a detuning Ω between the instantaneous frequencies of the two interacting pulses. Second, the pulse delay is multiplied with the chirp coefficient $\partial^2\phi/\partial t^2$ for rescaling. The results are depicted in Fig. 4.7(b), whereas only absolute values of the detuning are indicated so that two lines are obtained for each measurement. It should be noted, that the position of zero pulse delay is chosen so that the peaks occur at the same absolute value. Within this assumption at least three peaks for the polarization $E \parallel c \perp K$ and at least one peak for $E \perp c \parallel K$ are clearly visible.

The frequency detuning causes the grating to laterally move in time and tilt

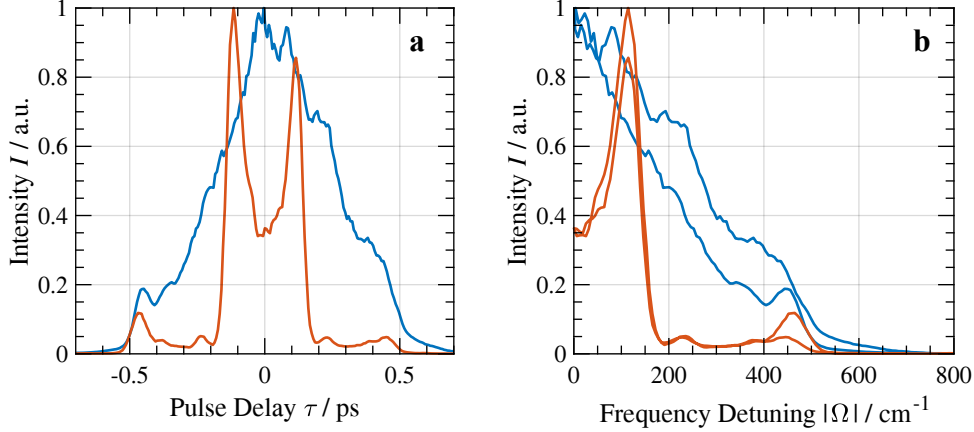


Figure 4.7: Spectral integrated self-diffraction signal $I(\tau)$ (a) and same data rescaled to a frequency detuning $\Omega = \tau \cdot \partial^2 \phi / \partial t^2 = \tau \cdot 1.86 \times 10^{26}$ rad/s (b). The data for lithium niobate shown in Fig. 4.4 are evaluated with a frequency chirp obtained from analyzing the measurement in glass [Fig. 4.6]. The polarization is set to $E \perp c \parallel K$ (blue) and $E \parallel c \perp K$ (red).

the orientation of the grating vector (see section 4.2). Peaks of the first non-Bragg diffraction signal can be attributed mainly to two contributions, (i) phase matching and (ii) diffraction efficiency. Generally, for a positive or negative detuning the grating vector tilts in different directions. When the phase matching condition is as sharp as the peaks, it should make a remarkable difference if the sign of the detuning is changed. Moreover, differences between a positive and negative detuning are visible only in a smaller signal for the whole branch. An overview of the phase matching of the first off-Bragg diffraction order is given in Fig. 4.8 in dependence of the frequency detuning and for different angles 2θ between the two beams. The depicted angle values are given for the geometry outside the medium and no temporal dependence is considered. One can clearly see a shift of perfect phase matching $\Delta k = 0$ to a non-zero detuning when increasing the angle 2θ . This corresponds to a lowered signal for one branch but defined peaks cannot be explained.

The diffraction efficiency is mainly based on the near-instantaneous nonlinear response of the refractive index n . So, another explanation could be based on an

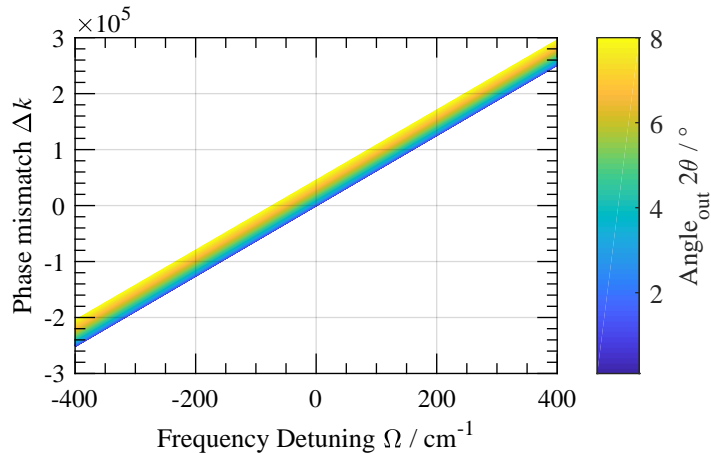


Figure 4.8: Phase mismatch Δk of the first off-Bragg diffraction order in dependence of a frequency difference Ω between the recording beams. Different angles 2θ between the two beams outside the sample are shown colorized. The central wavelength is $\lambda = 540$ nm.

increased modulation of n due to the detuning and some kind of resonance. The spectral range is comparable to phonon modes, but the results in Fig. 4.7(b) barely coincide with known Raman measurements for a light polarization along the polar c -axis [37, 39]. The frequency detuning enables difference-frequency generation in the terahertz frequency range, which could subsequently be used to excite phonons. This process would be accompanied by the conversion of photons to the lower frequency. Furthermore, terahertz photons can couple to phonons with an equal frequency, what is commonly described as phonon-polaritons [60–62]. Within these references, polaritons are analyzed by their wavevector and frequency to obtain a dispersion relation in transient grating measurements. They also show how the polaritons causes a deviation between measured and expected phonon frequencies for particular wavevectors. In comparison, the frequency peaks obtained in this work seem to coincide with reference [60], but the wavevector is not well defined in this self-diffraction experiment. Furthermore, the photo-excitation of polarons or additional absorption centers in general are not considered in these references. In principle, a coupling between additional phonons and polarons cannot be excluded. Nevertheless, the used method might be another tool to analyze the ultrafast response of nonlinear media in general.

4.2 Two color holography

In the previous section the diffraction from an ultrafast holographic grating recorded by two identical laser pulses was analyzed to obtain detailed pulse shapes. Now, the grating recording is changed from two identical (degenerated) to two initially detuned (non-degenerated) laser pulses to investigate the characteristics of dynamic gratings.

The author contributed to the following articles in the topic of two color holography. Abstracts are printed here with the friendly permission of the *Nature Publishing Group* and the *Optical Society of America* (OSA). Complete articles can be found in the attachment [A.2](#) and [A.3](#).

- S. Odoulov, A. Shumelyuk, H. Badorreck, S. Nolte, K.-M. Voit and M. Imlau. *Interference and holography with femtosecond laser pulses of different colours*, Nat. Comm. **6**, 5866, (2015); doi: 10.1038/ncomms6866.

Abstract: Interferometry and holography are two domains that are based on observation and recording of interference fringes from two light beams. While the aim of the first technique is to reveal and map the phase difference of two wave fronts, the main task of the second technique is to reconstruct one of the two recording waves via diffraction of the other wave from the recorded fringe pattern (hologram). To create fringes, mutually coherent waves from the same laser are commonly used. It is shown here that fringes can be observed and holograms can be recorded with ultrashort, sub-picosecond pulses even of different colour, generated in our experiment with two parametric amplifiers seeded, both by the same mode-locked Ti-sapphire laser. The appearance of permanent and transient gratings is confirmed by recording of an image-bearing hologram, by observation of two-beam coupling gain in a pump-probe experiment and by frequency conversion in Raman-Nath self-diffraction from a moving grating.

- H. Badorreck, A. Shumelyuk, S. Nolte, M. Imlau and S. Odoulov. *Doppler-shifted Raman-Nath diffraction from gratings recorded in LiNbO₃ with ultra-short laser pulses of different color*, Opt. Mater. Exp. **6**, 517–522, (2016), doi: 10.1364/OME.6.000517.

Abstract: Nominally undoped LiNbO₃ crystals feature a pronounced mixed (absorption/refraction) nonlinear response in the blue-green spectrum domain that is sufficient for the excitation of moving dynamic gratings and the observation of selfdiffraction with Doppler shifted higher orders. This type of Raman-Nath selfdiffraction can be successfully used for up- and down- frequency conversion as well as for characterization of the recording pulses.

4.3 Grating-assisted energy transfer

Within this study of frequency degenerated and non-degenerated grating recording, a pronounced increase of the pulse transmission is observed. The following publication reveals two different, grating based coupling mechanisms based on a frequency detuning and a difference in intensities.

The author contributed to the following article in the topic energy transfer from self-induced dynamic gratings. The abstract is printed here with the friendly permission of the *Optical Society of America* (OSA). The complete article can be found in the attachment [A.4](#).

- S. Nolte, B. Bourdon, F. Freytag, M. Imlau, A. Shumelyuk, and S. Odoulov
Dynamic-grating-assisted energy transfer between ultrashort laser pulses in lithium niobate,
Opt. Express **26**, 21558–21573, (2018), doi: 10.1364/OE.26.021558.

Abstract: Energy redistribution between two subpicosecond laser pulses of 2.5 eV photon energy is observed and studied in congruent, nominally undoped LiNbO₃, aiming to reveal the underlying coupling mechanisms. The dependences of pulse amplification on intensity, frequency detuning and pulse duration point to two different contributions of coupling, both based on self-diffraction from a recorded dynamic grating. The first one is caused by a difference in pulse intensities (transient energy transfer) while the second one originates from a difference in pulse frequencies. The latter appears when chirped pulses are mutually delayed in time. A quite high coupling efficiency has been observed in a 280 μm thin crystal: one order of magnitude energy amplification of a weak pulse and nearly 10% net energy enhancement of one pulse for the case of equal input intensities.

4.4 Diffraction of ultrashort lasers pulses from relief gratings

The above shown results expose a strong correlation between the pulse parameters and the ability of grating recording. To underline these findings, the diffraction from a static relief-grating is analyzed with different pulse shapes as well.

The author contributed to the following article in the topic of diffraction of ultrashort laser pulses from relief gratings. The abstract is printed here with the friendly permission of the *Optical Society of America* (OSA). The complete article can be found in the attachment [A.5](#)

- J. Eggert, B. Bourdon, S. Nolte, J. Rischmueller, and M. Imlau.
Chirp control of femtosecond-pulse scattering from drag-reducing surface-relief gratings,
Photon. Res. **6**, 542–548, (2018); doi: 10.1364/PRJ.6.000542.

Abstract: The role of chirp on the light–matter interaction of femto- and picosecond laser pulses with functional structured surfaces is studied using drag-reducing riblets as an example. The three-dimensional, periodic microstructure naturally gives rise to a mutual interplay of (i) reflection, (ii) scattering, and (iii) diffraction phenomena of incident coherent light. Furthermore, for femtosecond pulses, the structure induces (iv) an optical delay equivalent to a consecutive temporal delay of 230 fs in places of the pulse. These features enable studying experimentally and numerically the effect of tuning both pulse duration τ and spectral bandwidth $\Delta\omega$ on the features of the wide-angle scattering pattern from the riblet structure. As a result, we discovered a significant breakdown of fringes in the scattering pattern with decreasing pulse duration and/or increasing spectral bandwidth. This unique type of chirp control is straightforwardly explained and verified by numerical modeling considering the spectral and temporal interaction between different segments within the scattered, linearly chirped pulse and the particular geometric features of the riblet structure. The visibility of the fringe pattern can be precisely adjusted, and the off-state is achieved using $\tau < 230$ fs or $\Delta\omega > 2.85 \times 10^{13}$ rad/s.

Chapter 5

Conclusion & outlook

Concluding this work, self-induced holographic gratings need to be considered in every measurement with temporally synchronized femtosecond pulses, not only in the case of non-degenerated frequencies but also for frequency-degenerated pulses with a sufficiently short pulse duration. Accompanied by self-diffraction, dynamic fringes do not exclude the recording of a holographic grating. By pulse-shaping techniques the effect of the pulse duration, bandwidth and frequency chirp on the light-fringes are underlined. Furthermore, these dependencies are clarified by measurements on a relief grating, too. Because of a coupling between these dynamic gratings with particular resonances, energy transfer and a peaking diffraction efficiency can be observed. It seems reasonable from the frequency regime, the polarization dependence, a resonance-like signal, and similarities with Raman-based experiments, that phonon modes are involved in the interaction between the femtosecond pulses and the medium. Whereas phonon modes are already investigated in lithium niobate, they have been seldom studied in presence of small polarons and in the time scale below 1 ps.

The presented findings point towards a further detailed analysis of the phonon interaction with a dynamic holographic grating and/or the microscopic recording mechanism based on polarons or other metastable entities. In future experiments, phonons could be studied with transient grating techniques (energy transfer or self-diffraction), or in the impulsive excitation limit. Energy transfer might be used to determine time constants of microscopic transitions. By changing the wavevector geometry, the measured data could be assigned to specific phonon modes. This could be done either by changing the polarization setup, i.e., the orientation with respect to the crystal axes, or by changing the geometry of the impinging beams, e.g. to counter-propagating beams. Furthermore, the phonon frequency and the phonon number density commonly show a temperature dependence, whose influence on the measured signals should unambiguously underline the phononic origin. To the best knowledge, the effect of specific phonon modes onto the polaron formation is rarely investigated. In transient grating measurements, however, an immediate coupling between phonons and photons, which is described as a polariton, needs to be analyzed in detail as well.

Bibliography

- [1] A. Einstein. *Zur Quantentheorie der Strahlung*. Phys. Z. **18**, 121–128 (1917).
- [2] A. L. Schawlow, C. H. Townes. *Infrared and optical masers*. Physical Review **112**, 1940 (1958).
- [3] T. H. Maiman. *Stimulated optical radiation in ruby*. Nature **187**, 493 (1960).
- [4] A. J. Demaria, W. H. Glenn, M. J. Brienza, M. E. Mack. *Picosecond laser pulses*. Proceedings of the IEEE **57**, 2–25 (1969).
- [5] R. L. Fork, B. I. Greene, C. V. Shank. *Generation of optical pulses shorter than 0.1 psec by colliding pulse mode locking*. Applied Physics Letters **38**, 671–672 (1981).
- [6] M. Hentschel, R. Kienberger, C. Spielmann, G. A. Reider, N. Milosevic, T. Brabec, P. Corkum, U. Heinzmann, M. Drescher, F. Krausz. *Attosecond metrology*. Nature **414**, 509 (2001).
- [7] A. H. Zewail. *Femtochemistry: Atomic-scale dynamics of the chemical bond*. The Journal of Physical Chemistry A **104**, 5660–5694 (2000).
- [8] D. Gabor. *Nature A new microscopic principle* (1948).
- [9] R. W. Boyd. *Nonlinear optics*. Academic press (2003).
- [10] J. C. Diels, W. Rudolph. *Ultrashort laser pulse phenomena*. Elsevier (2006).
- [11] F. S. Chen, J. T. LaMacchia, D. B. Fraser. *Holographic storage in lithium niobate*. Applied Physics Letters **13**, 223–225 (1968).
- [12] K. Buse, A. Adibi, D. Psaltis. *Non-volatile holographic storage in doubly doped lithium niobate crystals*. Nature **393**, 665–668 (1998).
- [13] H. Li, F. Zhou, X. Zhang, W. Ji. *Picosecond Z-scan study of bound electronic Kerr effect in LiNbO₃ crystal associated with two-photon absorption*. Applied Physics B **64**, 659–662 (1997).
- [14] M. Imlau, H. Badorreck, C. Merschjann. *Optical nonlinearities of small polarons in lithium niobate*. Applied Physics Reviews **2**, 040606 (2015).
- [15] P. Reckenthaeler, D. Maxein, T. Woike, K. Buse, B. Sturman. *Separation of optical Kerr and free-carrier nonlinear responses with femtosecond light pulses in LiNbO₃ crystals*. Phys. Rev. B **76**, 195117 (2007).

-
- [16] F. Lüdtke, N. Waasem, K. Buse, B. Sturman. *Light-induced charge-transport in undoped LiNbO₃ crystals*. Appl. Phys. B **105**, 35–50 (2011).
- [17] Y. Qiu, K. B. Ucer, R. T. Williams. *Formation time of a small electron polaron in LiNbO₃: measurements and interpretation*. physica status solidi (c) **2**, 232–235 (2005).
- [18] S. Sasamoto, J. Hirohashi, S. Ashihara. *Polaron dynamics in lithium niobate upon femtosecond pulse irradiation: Influence of magnesium doping and stoichiometry control*. Journal of Applied Physics **105**, 083102 (2009).
- [19] O. Beyer, D. Maxein, T. Woike, K. Buse. *Generation of small bound polarons in lithium niobate crystals on the subpicosecond time scale*. Applied Physics B **83**, 527–530 (2006).
- [20] H. T. Hsieh, D. Psaltis, O. Beyer, D. Maxein, C. von Korff Schmising, K. Buse, B. Sturman. *Femtosecond holography in lithium niobate crystals*. Optics letters **30**, 2233–2235 (2005).
- [21] F. Träger. *Springer handbook of lasers and optics*. Springer Science & Business Media (2007).
- [22] R. S. Weis, T. K. Gaylord. *Lithium niobate: summary of physical properties and crystal structure*. Applied Physics A **37**, 191–203 (1985).
- [23] T. Volk, M. Wöhlecke. *Lithium niobate: defects, photorefraction and ferroelectric switching*. Springer Science & Business Media (2008).
- [24] O. Beyer, D. Maxein, K. Buse, B. Sturman, H. T. Hsieh, D. Psaltis. *Femtosecond time-resolved absorption processes in lithium niobate crystals*. Optics letters **30**, 1366–1368 (2005).
- [25] O. Beyer, D. Maxein, K. Buse, B. Sturman, H. T. Hsieh, D. Psaltis. *Investigation of nonlinear absorption processes with femtosecond light pulses in lithium niobate crystals*. Physical Review E **71**, 056603 (2005).
- [26] F. Freytag, P. Booker, G. Corradi, S. Messerschmidt, A. Krampf, M. Imlau. *Picosecond near-to-mid-infrared absorption of pulse-injected small polarons in magnesium doped lithium niobate*. Optical Materials Express **8**, 1505–1514 (2018).
- [27] D. Emin. *Polarons*. Cambridge University Press (2013).
- [28] D. Berben, K. Buse, S. Wevering, P. Herth, M. Imlau, T. Woike. *Lifetime of small polarons in iron-doped lithium–niobate crystals*. Journal of applied physics **87**, 1034–1041 (2000).
- [29] P. Herth, T. Granzow, D. Schaniel, T. Woike, M. Imlau, E. Krätzig. *Evidence for Light-Induced Hole Polarons in LiNbO₃*. Physical review letters **95**, 067404 (2005).
- [30] C. Merschjann, D. Berben, M. Imlau, M. Wöhlecke. *Evidence for two-path recombination of photoinduced small polarons in reduced LiNbO₃*. Physical review letters **96**, 186404 (2006).

-
- [31] O. F. Schirmer. *O⁻ bound small polarons in oxide materials*. Journal of Physics: Condensed Matter **18**, R667 (2006).
- [32] C. Merschjann, B. Schoke, M. Imlau. *Influence of chemical reduction on the particular number densities of light-induced small electron and hole polarons in nominally pure LiNbO₃*. Physical Review B **76**, 085114 (2007).
- [33] O. F. Schirmer, M. Imlau, C. Merschjann, B. Schoke. *Electron small polarons and bipolarons in LiNbO₃*. Journal of Physics: Condensed Matter **21**, 123201 (2009).
- [34] C. Merschjann, B. Schoke, D. Conradi, M. Imlau, G. Corradi, K. Polgar. *Absorption cross sections and number densities of electron and hole polarons in congruently melting LiNbO₃*. Journal of Physics: Condensed Matter **21**, 015906 (2009).
- [35] B. Sturman, E. Podivilov, M. Gorkunov. *Origin of stretched exponential relaxation for hopping-transport models*. Physical review letters **91**, 176602 (2003).
- [36] D. Maxein, S. Kratz, P. Reckenthaeler, J. Bückers, D. Haertle, T. Woike, K. Buse. *Polarons in magnesium-doped lithium niobate crystals induced by femtosecond light pulses*. Applied Physics B **92**, 543 (2008).
- [37] W. D. Johnston Jr, I. P. Kaminow. *Temperature dependence of Raman and Rayleigh scattering in LiNbO₃ and LiTaO₃*. Physical Review **168**, 1045 (1968).
- [38] M. D. Fontana, P. Bourson. *Microstructure and defects probed by Raman spectroscopy in lithium niobate crystals and devices*. Applied Physics Reviews **2**, 040602 (2015).
- [39] S. Sanna, S. Neufeld, M. Rüsing, G. Berth, A. Zrenner, W.G. Schmidt. *Raman scattering efficiency in LiTaO₃ and LiNbO₃ crystals*. Physical Review B **91**, 224302 (2015).
- [40] H. J. Eichler, P. Günter, D. W. Pohl. *Laser-induced dynamic gratings*. Springer (2013).
- [41] H. Kogelnik. *Coupled wave theory for thick hologram gratings*. Bell Syst. Tech. J. **48**, 2909–2947 (1969).
- [42] P. Yeh. *Two-wave mixing in nonlinear media*. Quantum Electronics, IEEE Journal of **25**, 484–519 (1989).
- [43] P. Yeh. *Introduction to photorefractive nonlinear optics*. Wiley-Interscience (1993).
- [44] N. Kukhtarev, V. Markov, S. Odulov. *Transient energy transfer during hologram formation in LiNbO₃ in external electric field*. Opt. Commun. **23**, 338–343 (1977).
- [45] V. L. Vinetskii, N. V. Kukhtarev, S. G. Odulov, M. S. Soskin. *Dynamic self-diffraction of coherent light beams*. Soviet Physics Uspekhi **22**, 742 (1979).

- [46] C.-T. Chen, D. M. Kim, D. von der Linde. *Efficient hologram recording in $\text{LiNbO}_3\text{:Fe}$ using optical pulses*. Applied Physics Letters **34**, 321–324 (1979).
- [47] F. Jermann, K. Buse. *Light-induced thermal gratings in $\text{LiNbO}_3\text{:Fe}$* . Applied Physics B **59**, 437–443 (1994).
- [48] M. Imlau, H. Brüning, B. Schoke, R.-S. Hardt, D. Conradi, C. Merschjann. *Hologram recording via spatial density modulation of $\text{Nb}_{\text{Li}}^{4+/5+}$ antisites in lithium niobate*. Optics express **19**, 15322–15338 (2011).
- [49] H. Brüning, V. Dieckmann, B. Schoke, K.-M. Voit, M. Imlau, G. Corradi, C. Merschjann. *Small-polaron based holograms in LiNbO_3 in the visible spectrum*. Optics express **20**, 13326–13336 (2012).
- [50] U. Megerle, I. Pugliesi, C. Schrieber, C.F. Sailer, E. Riedle. *Sub-50 fs broadband absorption spectroscopy with tunable excitation: putting the analysis of ultrafast molecular dynamics on solid ground*. Applied Physics B **96**, 215–231 (2009).
- [51] S. Ruhman, B. Kohler, A. G. Joly, K. A. Nelson. *Intermolecular vibrational motion in CS_2 liquid at $165 < T < 300$ K observed by femtosecond time-resolved impulsive stimulated scattering*. Chemical physics letters **141**, 16–24 (1987).
- [52] S. Ruhman, A. G. Joly, K. A. Nelson. *Coherent molecular vibrational motion observed in the time domain through impulsive stimulated Raman scattering*. IEEE journal of quantum electronics **24**, 460–469 (1988).
- [53] L. Dhar, J. A. Rogers, K. A. Nelson. *Time-resolved vibrational spectroscopy in the impulsive limit*. Chemical Reviews **94**, 157–193 (1994).
- [54] S. A. Kovalenko, A. L. Dobryakov, J. Ruthmann, N. P. Ernsting. *Femtosecond spectroscopy of condensed phases with chirped supercontinuum probing*. Physical Review A **59**, 2369 (1999).
- [55] P. Kukura, S. Yoon, R. A. Mathies. *Femtosecond stimulated Raman spectroscopy*. Analytical chemistry **78**, 5953–9 Sep 2006.
- [56] K. W. DeLong, R. Trebino, D. J. Kane. *Comparison of ultrashort-pulse frequency-resolved-optical-gating traces for three common beam geometries*. JOSA B **11**, 1595–1608 (1994).
- [57] R. Trebino, K. W. DeLong, D. N. Fittinghoff, J. N. Sweetser, M. A. Krumbügel, B. A. Richman, D. J. Kane. *Measuring ultrashort laser pulses in the time-frequency domain using frequency-resolved optical gating*. Rev. of Scientific Instruments **68**, 3277–3295 (1997).
- [58] R. Trebino. *Frequency-resolved optical gating: the measurement of ultrashort laser pulses*. Springer Science & Business Media (2012).
- [59] R. Trebino. *Ultrafast Optics Group Website* (08/2018): <http://frog.gatech.edu/code.html>.
- [60] H. J. Bakker, S. Hunsche, H. Kurz. *Investigation of anharmonic lattice vibrations with coherent phonon polaritons*. Phys. Rev. B **50**, 914 (1994).

- [61] U. T. Schwarz, M. Maier. *Frequency dependence of phonon-polariton damping in lithium niobate*. Physical Review B **53**, 5074 (1996).
- [62] D. P. Kien, J. C. Loulergue, J. Etchepare. *Nonlinear response to polariton waves driven in perovskites by femtosecond pulses*. Optics communications **101**, 53–59 (1993).

Appendix A

Publications

- A.1 Scanning nonlinear absorption in lithium niobate over the time regime of small polaron formation

Scanning nonlinear absorption in lithium niobate over the time regime of small polaron formation

Holger Badorreck, Stefan Nolte, Felix Freytag, Pia Bäune, Volker Dieckmann, and Mirco Imlau*

School of Physics, Osnabrueck University,
Barbarastr. 7, 49076 Osnabrueck, Germany

[*mimlau@uos.de](mailto:mimlau@uos.de)

Abstract: Nonlinear absorption is studied in presence of small polaron formation in lithium niobate using the z -scan technique and ultrashort laser pulses with pulse durations of 70 – 1,000 fs. A model for the analysis of the transmission loss as a function of pulse duration is introduced that considers (i) the individual contributions of two-photon and small polaron absorption, (ii) the small polaron formation time and (iii) an offset time between the optical excitation of free carriers by two-photon absorption and the appearance of small polarons. It is shown that the model allows for the analysis of the experimentally determined z -scan data with high precision over the entire range of pulse durations using a two-photon absorption coefficient of $\beta = (5.6 \pm 0.8) \text{ mm/GW}$. A significant contribution by small polaron absorption to the nonlinear absorption is uncovered for pulse durations exceeding the characteristic small polaron formation time of ≈ 100 fs. It can be concluded that the small polaron formation time is as short as (70 – 110) fs and the appearance of small polaron formation is delayed with respect to two-photon absorption by an offset of about 80 fs.

© 2015 Optical Society of America

OCIS codes: (190.4180) Multiphoton processes; (190.4720) Optical nonlinearities of condensed matter; (320.7110) Ultrafast nonlinear optics; (320.7130) Ultrafast processes in condensed matter, including semiconductors; (160.3730) Lithium niobate.

References and links

1. M. Fejer, G. Magel, D. H. Jundt, and R. Byer, "Quasi-phase-matched second harmonic generation: tuning and tolerances," *IEEE J. Quantum Electron.* **28**, 2631–2654 (1992).
2. O. A. Louchev, H. H. Hatano, N. Saito, S. Wada, and K. Kitamura, "Laser-induced breakdown and damage generation by nonlinear frequency conversion in ferroelectric crystals: Experiment and theory," *J. Appl. Phys.* **114**, 203101 (2013).
3. O. F. Schirmer and D. von der Linde, "Two-Photon and X-Ray-Induced Nb^{4+} and O^- Small Polarons in LiNbO_3 ," *Appl. Phys. Lett.* **33**, 35 (1978).
4. D. Emin, *Polarons* (Cambridge University Press, Cambridge, 2013).
5. C. Merschjann, B. Schoke, D. Conradi, M. Imlau, G. Corradi, and K. Polgar, "Absorption cross sections and number densities of electron and hole polarons in congruently melting LiNbO_3 ," *J. Phys. Chem. Sol.* **21**, 015906 (2009).
6. Y. Qiu, K. B. Ucer, and R. T. Williams, "Formation time of a small electron polaron in LiNbO_3 : measurements and interpretation," *Phys. Stat. Sol. C* **2**, 232 (2005).
7. S. Sasamoto, J. Hirohashi, and S. Ashihara, "Polaron dynamics in lithium niobate upon femtosecond pulse irradiation: Influence of magnesium doping and stoichiometry control," *J. Appl. Phys.* **105**, 083102 (2009).

8. O. Beyer, D. Maxein, K. Buse, B. Sturman, H. T. Hsieh, and D. Psaltis, "Investigation of nonlinear absorption processes with femtosecond light pulses in lithium niobate crystals," *Phys. Rev. E* **71**, 056603 (2005).
9. O. Beyer, D. Maxein, T. Woike, and K. Buse, "Generation of small bound polarons in lithium niobate crystals on the subpicosecond time scale," *Appl. Phys. B* **83**, 527–530 (2006).
10. H. Yochum, K. Ucer, R. Williams, P. Sheldon, V. Nagirnyi, V. Denks, L. Grigorjeva, D. Millers, and E. Kotomin, "Short-pulse excitation and spectroscopy of KNbO_3 , LiNbO_3 and KTiOPO_4 ," *Rad. Eff. Def. Sol.* **150**, 271–276 (1999).
11. M. Imlau, H. Badorreck, and C. Merschjann, "Optical nonlinearities of small polarons in lithium niobate," *Appl. Phys. Rev.* **2**, 040606 (2015).
12. D. Maxein and K. Buse, "Interaction of Femtosecond Laser Pulses with Lithium Niobate Crystals: Transmission Changes and Refractive Index Modulations," *J. Holography Speckle* **5**, 1–5 (2009).
13. A. Seilmeier and W. Kaiser, "Generation of tunable picosecond light pulses covering the frequency range between 2700 and 32,000 cm^{-1} ," *Appl. Phys. A* **23**, 113 (1980).
14. R. DeSalvo, A. Said, D. Hagan, E. Van Stryland, and M. Sheik-Bahae, "Infrared to ultraviolet measurements of two-photon absorption and n_2 in wide bandgap solids," *IEEE J. Quantum Electron.* **32**, 1324 (1996).
15. H. Li, F. Zhou, X. Zhang, and W. Ji, "Picosecond Z-scan study of bound electronic Kerr effect in LiNbO_3 crystal associated with two-photon absorption," *Appl. Phys. B* **64**, 659 (1997).
16. R. Ganeev, I. Kulagin, A. Rysanyansky, R. Tugushev, and T. Usmanov, "Characterization of nonlinear optical parameters of KDP, LiNbO_3 and BBO crystals," *Opt. Commun.* **229**, 403–412 (2004).
17. O. Beyer, D. Maxein, K. Buse, B. Sturman, H. T. Hsieh, and D. Psaltis, "Femtosecond time-resolved absorption process in lithium niobate crystals," *Opt. Lett.* **30**, 1366 (2005).
18. M. Sheik-Bahae, A. A. Said, T. H. Wei, D. J. Hagan, and E. W. Van Stryland, "Sensitive Measurement of Optical Nonlinearities Using A Single Beam," *IEEE J. Quantum Electron.* **26**, 760 (1990).
19. A. A. Said, M. Sheik-Bahae, D. J. Hagan, T. H. Wei, J. Wang, J. Young, and E. W. Van Stryland, "Determination of Bound-electronic and Free-carrier Nonlinearities In ZnSe, GaAs, CdTe, and ZnTe," *J. Opt. Soc. Am. B* **9**, 405 (1992).
20. S. Redfield and W. J. Burke, "Optical Absorption Edge of LiNbO_3 ," *J. Appl. Phys.* **45** (1974).
21. H. Badorreck, School of Physics, Osnabrueck University, Barbarastr. 7, 49076 Osnabrueck, Germany, A. Shumelyuk, S. Nolte, M. Imlau, and S. Odoulov are preparing a manuscript to be called "Selfdiffraction from moving gratings recorded in LiNbO_3 with ultra-short laser pulses of different colors."
22. A. Othonos, "Probing ultrafast carrier and phonon dynamics in semiconductors," *J. Appl. Phys.* **83**, 1789–1830 (1998).
23. M. Garcia-Lechuga, J. Siegel, J. Hernandez-Rueda, and J. Solis, "Imaging the ultrafast Kerr effect, free carrier generation, relaxation and ablation dynamics of Lithium Niobate irradiated with femtosecond laser pulses," *J. Appl. Phys.* **116**, 113502 (2014).
24. O. F. Schirmer, O. Thiemann, and M. Wöhlecke, "Defects in LiNbO_3 — I. Experimental Aspects," *J. Phys. Chem. Solids* **52**, 185 (1991).
25. O. F. Schirmer, "O⁻ bound small polarons in oxide materials," *J. Phys. Condens. Matter* **18**, R667 (2006).
26. O. F. Schirmer, M. Imlau, C. Merschjann, and B. Schoke, "Electron small polarons and bipolarons in LiNbO_3 ," *J. Phys. Condens. Matter* **21**, 123201 (2009).
27. B. Faust, H. Müller, and O. F. Schirmer, "Free small polarons in LiNbO_3 ," *Ferroelectrics* **153**, 297 (1994).
28. Y. Li, W. G. Schmidt, and S. Sanna, "Intrinsic LiNbO_3 point defects from hybrid density functional calculations," *Phys. Rev. B* **89**, 094111 (2014).
29. Y. Li, S. Sanna, and W. G. Schmidt, "Modeling intrinsic defects in LiNbO_3 within the Slater-Janak transition state model," *The Journal of Chemical Physics* **140**, 234113 (2014).
30. K. Ogusu and K. Shinkawa, "Optical nonlinearities in silicon for pulse durations of the order of nanoseconds at 1.06 μm ," *Opt. Express* **16**, 14780–14791 (2008).
31. P. B. Chapple, J. Staromlynska, J. A. Hermann, T. J. McKay, and R. G. Mcduff, "Single-Beam Z-Scan: Measurement Techniques and Analysis," *J. Nonlinear Opt. Phys. Mater.* **06**, 251–293 (1997).
32. M. Sheik-Bahae, D. J. Hagan, and E. W. Van Stryland, "Dispersion and band-gap scaling of the electronic Kerr effect in solids associated with two-photon absorption," *Phys. Rev. Lett.* **65**, 96–99 (1990).
33. O. F. Schirmer, M. Imlau, and C. Merschjann, "Bulk photovoltaic effect of $\text{LiNbO}_3\text{:Fe}$ and its small-polaron-based microscopic interpretation," *Phys. Rev. B* **83**, 165106 (2011).

1. Introduction

Lithium niobate, LiNbO_3 (LN), acts as a reference material in the field of nonlinear optics and experiences increasing attention as frequency converter due to its sound second-order nonlinearity $\chi^{(2)}$, chemical and mechanical stability as well as availability [1]. For efficient conversion, LN is exposed to very intense, short and ultra-short laser pulses; at high intensities, how-

ever, the problem of nonlinear absorption arises due to a predominant contribution of third order nonlinearities $\chi^{(3)}$, in particular two-photon absorption (TPA). Besides limiting the conversion efficiency, TPA plays a major role in irreversible bulk laser-induced damage mechanisms of ferroelectric crystals by heating as well as via the generation of free carriers [2]. In LN the subsequent formation of small polarons from optically excited free carriers must be considered [3], as well, i.e. carriers that become trapped with strong coupling within a self-induced distortion of the surrounding unit cell [4]. As we are dealing with lithium niobate grown from the congruently melting composition, the term *small polarons* applies to the small free polaron ($\text{Nb}_{\text{Nb}}^{4+}$) placed at a regular lattice site and, due to the non-stoichiometric crystal structure bounded by an antisite defect, the small bound polaron ($\text{Nb}_{\text{Li}}^{4+}$) as well as the small hole polaron (O^-). The contribution of small polarons to the nonlinear absorption is determined by their broad band (≈ 1 eV) and pronounced absorption features [5] and characterized by a transient absorption with lifetimes in the regime from μs to ms at room temperature, thus commonly exceeding the pulse duration. Nonlinear interactions of small polarons with short, intense laser pulses in LN have been already addressed by different research groups [6–9]. However, the dependency of nonlinear absorption on incident laser pulses with different pulse durations has not been studied, so far, which is the topic of this work. The pulse duration dependency is of particular interest for nonlinear optical applications using sub-ps laser pulse durations that fall in the time regime of small polaron formation; the latter has been estimated to values much below 400 fs [6, 7, 9–11]. Without this knowledge, nothing is known about the individual contribution of TPA and small polaron absorption to the transmission loss of a propagating (ultra-)short laser pulse. Furthermore, it remains unclear to what extent pulse durations exist where the contribution of small polaron absorption becomes negligible.

In LN, first efforts have been made to separate optically excited carriers from the Kerr third order nonlinearity by means of grating recording [12] or transient absorption [8], demonstrating the impact of carrier dynamics in the time regime subsequent to the incident ultrashort laser pulse (240 fs). Furthermore, the two-photon absorption coefficient β has been determined using various pulse durations in the range of 80 fs – 55 ps yielding values of β between 1.5 and 5.2 mm/GW in the green spectral range (Refs. [7, 13–17], cf. review [11]).

We here study the dependency of nonlinear absorption on the duration of incident (ultra-)short laser pulses in lithium niobate by systematically scanning the transmission loss over the time regime of $70 \text{ fs} < \tau < 1,000 \text{ fs}$ by means of z -scan technique. For analysis, the differential equation for the intensity decrease of a propagating laser pulse along the crystal coordinate is derived. The temporal interplay of non-instantaneous processes with rise/relaxation times in the sub-ps time regime are considered: TPA, free carrier relaxation, small polaron formation and cascaded carrier excitation. The model extensions are motivated by a significant deviation – increasing for longer pulse durations – between experimental data and data analysis based on TPA (cf. original work from Sheik-Bahae [18]), but also TPA with free-carrier absorption [19]. Using our model for analysis, the experimental findings are described over the entire range of pulse durations with high precision. A deconvolution of the individual contributions – particularly of small polaron and two-photon absorption – to nonlinear absorption along the time coordinate becomes possible. We discuss the obtained temporal evolution of the small polaron impact from the viewpoint of a more precise estimate for the small polaron formation time, the existence of an offset of small polaron appearance upon the incident laser pulse as proposed by Qiu et al. [6] and pulse durations that are insignificantly affected by small polaron formation. It can be concluded, that the pulse duration dependency of nonlinear absorption yields important information for the area of nonlinear applications with intense, (ultra-)short laser pulses of LN, but also of the variety of nonlinear optical materials showing small polaron formation in general.

2. Modeling

2.1. Temporal evolution of optically excited carriers in lithium niobate

For our study, we refer to the potential scheme depicted in Fig. 1, particularly describing the interplay of two-photon and small polaron absorption. In what follows, the configuration coordinate

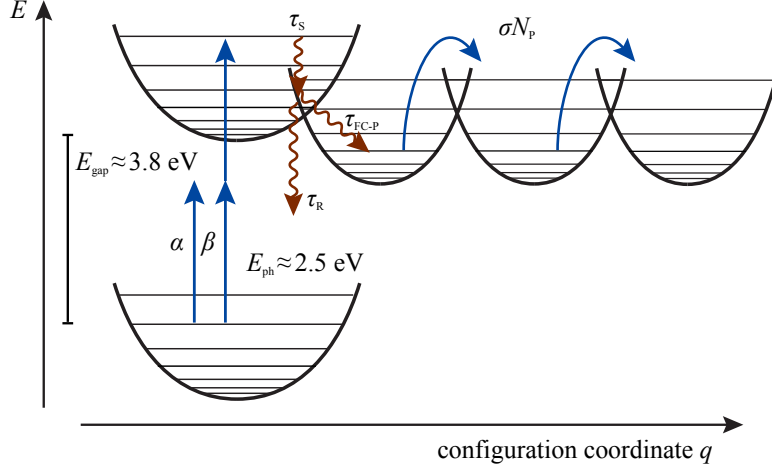


Fig. 1. Potential diagram of the band-to-band excitation by one-photon (α) and two-photon (β) absorption with photon energies of $E_{\text{ph}} = 2.5$ eV, electron-phonon cooling process with time constant τ_S , relaxation to the ground state (τ_R) and subsequent formation of small polarons ($\tau_{\text{FC-P}}$) in lithium niobate. Absorption cross section σ and number density of polarons N_P determine the absorption triggered by optically induced transport of small polarons [11].

dinate q will be identified as spatial displacements of carriers in the real crystal lattice in the nanoscopic regime as well as the time axis covering the sub-ps regime.

We focus our considerations on the absorption of incident (ultra-)short sub-ps laser pulses with a photon energy of $E_{\text{ph}} = 2.5$ eV via one-photon and two-photon absorption in a nominally undoped LN crystal. The probability of the former is small because of the large band gap of lithium niobate ($\alpha = 20 \text{ cm}^{-1}$ at ≈ 3.8 eV [20]), i.e. the LN crystal is transparent for this photon energy at low incident laser intensities. At the contrary, two-photon absorption dominates the nonlinear absorption at elevated intensities. For the regime of sub-ps laser pulses, the TPA coefficient β is reported to values of $\beta = 5.2 \text{ mm/GW}$ (80 fs, 400 nm, Mg-doped LN) [7] and $\beta = 3.5 \text{ mm/GW}$ (240 fs, ≈ 480 nm, nominally undoped LN) [17]. The response time of TPA being related to bound electrons is nearly instantaneous; an estimate of $\tau_{\text{TPA}} \approx 5$ fs has been deduced from degenerate recording of TPA gratings for LN crystals [21], such that $\tau_{\text{TPA}} \ll \tau$ for all pulse durations (70 – 1,000 fs) in our study. The temporal dynamics of TPA will thus be neglected in the differential equations given in the theoretical subsection below.

With TPA, free carriers far from the thermal equilibrium (hot carriers) are generated by means of valence-to-conduction band excitation. Energy relaxation to the lowest levels of the conduction band occurs preliminary via the emission of phonons; for semiconductors, this electron-phonon cooling process is characterized by a relaxation time of $\tau_S \approx 100$ fs [22]. For LN, $\tau_S = 80$ fs has been calculated for relaxation from an energetic level 0.5 eV above the conduction band minimum ($T=296$ K) [6]. By experimental means, ultrafast pump-probe spectroscopy with LN did not show indications of an energy relaxation of hot carriers, so

far [6,8], whereas the time-resolved measurement of the reflectivity of a lithium niobate surface reveals a delayed signal with $\tau_S = 600$ fs that has been attributed to free electron generation [23].

In the next step, the carrier may either relax to the ground state by recombination with a hole and a characteristic time constant τ_R . Or carrier localization occurs followed by strong vibrational coupling, i.e. a small polaron is formed with characteristic time constant τ_{FC-P} (*small polaron formation time*). In LN, $\tau_{FC-P} \approx 100$ fs for small free Nb_{Nb}^{4+} polarons (room temperature) [6,7] and $\tau_{FC-P} < 400$ fs for small bound Nb_{Li}^{4+} polarons [9].

If the pulse duration exceeds the temporal regime until small polaron formation, the optical excitation from a small polaron must be considered, as well, and the carrier relaxes repeatedly into a small polaron. We assume that this process can be repeated several times over the incident pulse duration, i.e. cascaded excitation occurs [11].

In a similar way, the remaining holes in the valence band become localized as O^- hole polarons in the vicinity of lithium vacancies [3,24,25]. In the following, however, we will not distinguish between the particular types of small electron and hole polarons [24,26,27], because of probing at a single photon energy and the overlap of the absorption features of small free and bound electron and small hole polarons [5]. All types of small polarons result from the intrinsic defect structure of $LiNbO_3$ that – although complex – has been modeled from first principles in very recent articles by *Li et al.* [28,29]. We, thus, use LN crystals grown from the congruently melting composition in our experimental study.

2.2. Transfer to z -scan technique

The starting point for the determination of the nonlinear absorption composed by TPA and small polaron absorption is the z -scan technique. It has been developed originally for the analysis of near-instantaneous third order nonlinearities, particularly of the two-photon coefficient β and the nonlinear index of refraction n_2 [18]. A nonlinear optical sample is shifted (*scanned*) along the z -coordinate through the focus of a laser pulse with spatial and temporal Gaussian intensity profile. The transmission as a function of z is expressed by

$$T(z) = \frac{1}{q(z)\sqrt{\pi}} \int_{-\infty}^{\infty} \ln(1 + q(z)\exp(-s^2)) ds \quad (1)$$

with $q(z) = \beta I d_{\text{eff}} / (1 + z^2/z_0^2)$, the peak intensity I , the two-photon absorption coefficient β , the effective sample thickness d_{eff} and integration constant s . The additional impact of free-carrier absorption to the transmission was derived in Ref. [19]; Ogusu et al. [30] introduced the appearance of a transient free carrier absorption with silicon as an example. Based on these theoretical concepts, we need to add the characteristic time of electron-phonon relaxation τ_S , i.e. a temporal offset prior to small polaron formation, as a particular feature of small polaron dynamics. Then, the change of the pulse intensity through a sample as a function of the propagation depth L , radius r and time t is given by:

$$\frac{\partial I(L, r, t)}{\partial L} = -[\alpha + \beta I(L, r, t) + \sigma N_P(L, r, t)] I(L, r, t). \quad (2)$$

Here, α is the one-photon absorption coefficient, and σ and N_P are the absorption cross section and number density of small polarons. The temporal evolution of the latter is modeled according to Fig. 1 by considering the number density of free carriers N_{FC} , the subsequent electron-phonon cooling (τ_S), carrier recombination (τ_R) and/or small polarons formation (τ_{FC-P}) during pulse duration (τ) via:

$$\frac{\partial N_P(L, r, t)}{\partial t} = \frac{N_{FC}(L, r, t - \tau_S)}{\tau_{FC-P}} \quad (3)$$

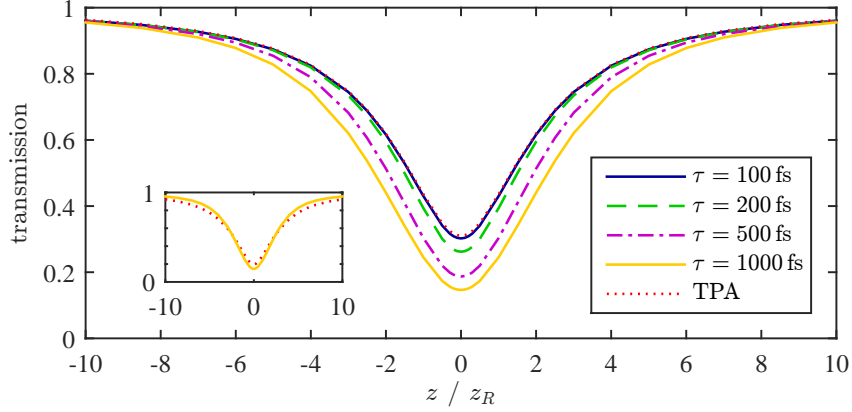


Fig. 2. Numerical solution of Eq. (2) as a function of pulse duration (100 fs – 1,000 fs) and the following model parameters: $\alpha = 0 \text{ m}^{-1}$, $\beta = 5 \text{ mm/GW}$, $\tau_S = 100 \text{ fs}$, $\tau_{\text{FC-P}} = 100 \text{ fs}$, $\tau_R = 100 \text{ fs}$, $\sigma = 100 \cdot 10^{-22} \text{ m}^2$, and peak intensity $I = 8.6 \text{ PW/m}^2$ at $z = 0$. E.g., this results in a maximum polaron number density of $N_P = 1.7 \cdot 10^{17} \text{ mm}^{-3}$ at the center of the pulse with maximum intensity for $\tau = 1,000 \text{ fs}$. For comparison the red dotted graph representing Eq. (1) is also shown. The inset highlights the change in the shape of the transmission traces exemplarily for a pulse duration of 1,000 fs and a fitted graph using the original z -scan theory Eq. (1) with an TPA-coefficient increased by a factor of 2.2 in comparison to the main figure.

with the temporal evolution of free carriers:

$$\frac{\partial N_{\text{FC}}(L, r, t)}{\partial t} = \frac{\alpha I(L, r, t)}{h\nu} + \frac{\beta I^2(L, r, t)}{2h\nu} - \frac{N_{\text{FC}}(L, r, t - \tau_S)}{\tau_R} - \frac{N_{\text{FC}}(L, r, t - \tau_S)}{\tau_{\text{FC-P}}} \quad (4)$$

Differential equation (2) is solved numerically with spatial and temporal Gaussian distribution of the input intensity for data analysis; Fig. 2 highlights the impact of pulse duration on the transmission of a z -scan measurement. For numerical solution, the following model parameters are used: $\alpha = 0 \text{ m}^{-1}$, $\beta = 5 \text{ mm/GW}$, $\tau_S = 100 \text{ fs}$, $\tau_{\text{FC-P}} = 100 \text{ fs}$, $\tau_R = 100 \text{ fs}$ and the pulse duration is varied from 100 fs to 1,000 fs while the peak intensity I at $z = 0$ is kept constant at 8.6 PW/m^2 . The plots show the characteristic drop of the transmission while scanning along the z -coordinate with a minimum transmission at $z = 0$, and are mirror symmetric to $z = 0$. The additional contribution of non-instantaneous absorption processes results in a pronounced increase of the transmission loss in the order of several tens of percentage, i.e. the increase of nonlinear absorption by small polaron formation, with increasing pulse duration is obvious. For comparison, the result of Eq. (1) considering the action of TPA, only, is depicted in addition (red curve). The numerical solution Eq. (2) converges to the result of Eq. (1) for pulse durations equal to the electron-phonon cooling rate, $\tau \simeq \tau_S$, or below. Thus, it is possible to estimate the characteristic time constants of small polaron formation from z -scan experiments as a function of pulse duration, if τ is in the order of τ_S . It is important to note, that the analysis of nonlinear absorption using Eq. (1) and pulse durations exceeding τ_S will result in an overestimate of the TPA coefficient β . This is due to the fact, that the numerical solutions not only show an increase in the transmission loss, but also a change in the shape of $T(z)$ (cf. inset of Fig. 2). A limit of the numerical analysis is that it is not possible to distinguish between several types of small bound polarons; this, however, may be solved by performing a systematic study at different photon energies of the incident pulse.

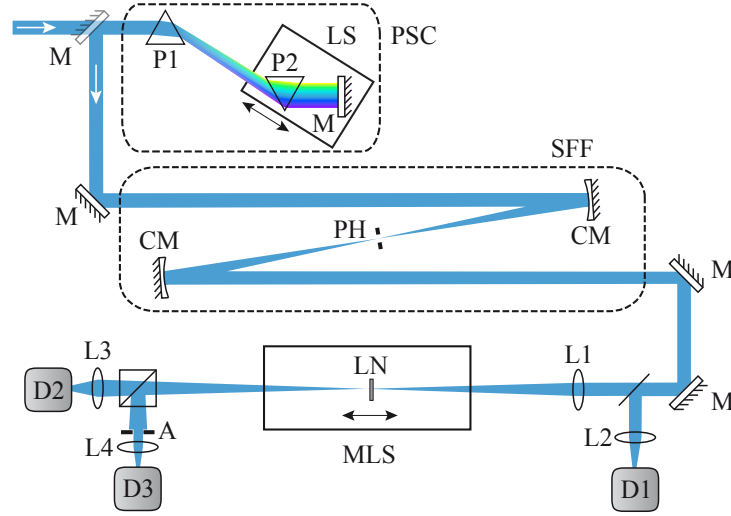


Fig. 3. Sketch of the optical setup composed by a prism stretcher/compressor (PSC) (P1; P2 on a linear stage LS), a spatial frequency filter (SFF) (CM: concave mirrors with $f = 500$ mm, PH: pinhole with diameter of $100\ \mu\text{m}$) and a common configuration for z -scan technique: L1: lens ($f = 150$ mm), LN: lithium niobate crystal, MLS: motorized linear stage, L2-L4: lenses ($f = 50$ mm), D1-D3: Si-PIN detectors (photosensitive area \gg beam spot), A: aperture with diameter of 4 mm. Incident pulses obey a maximum pulse energy of $150\ \mu\text{J}$ at 2.5 eV (center wavelength: 488 nm) and are adjusted in intensity by a neutral density filter. The repetition rate of 250 Hz is reduced to 12.5 Hz using a Chopper wheel. The pulse duration can be varied with PSC from 70 fs – $1,000$ fs.

3. Experimental section

3.1. Setup and lithium niobate samples

The systematic scan of the nonlinear absorption over the time regime of 70 fs – $1,000$ fs has been performed using the common z -scan technique described in Ref. [18] with an incident laser pulse of spatial and temporal Gaussian profile that – as an original feature – has been compressed/stretched to the desired pulse duration. The extended setup, as depicted schematically in Fig. 3, is composed by (i) a prism pulse stretcher/compressor, (ii) a spatial frequency filter, and (iii) the common z -scan configuration. An optical parametric amplifier (Coherent Inc., model: OPerA solo) pumped by a regeneratively amplified Ti^{3+} :Sapphire laser (Coherent Inc., model: Libra-F HE) serves as the source for ultrashort laser pulses (pulse energy maximum: $150\ \mu\text{J}$ at 2.5 eV, center wavelength: 488 nm). A neutral density filter is used for intensity adjustment. The repetition rate of 250 Hz is reduced to 12.5 Hz using a Chopper wheel, in order to avoid cumulative absorption from pulse to pulse due to long-lived small polarons (maximum characteristic lifetime ≈ 3 ms at room temperature, see e.g. Ref [11]). The pulses first enter a prism pulse stretcher/compressor that allows for tuning the pulse duration by means of adjustment of prism P2 and mirror M using a linear stage (LS). A spectral width of $\Delta\lambda = 5$ nm is obtained, equal with a bandwidth limited pulse duration of $\tau \approx 70$ fs. For the purpose of our study, the pulse duration is varied up to $1,000$ fs and characterized by means of a scanning autocorrelator (APE, model pulseCheck 15). After the stretcher/compressor, the pulses enter a spatial frequency filter that consists of two concave mirrors (focal length: 500 mm), avoiding chromatic aberration, and a pinhole (diameter $d = 100\ \mu\text{m}$). Astigmatism is minimized by a small angle of incidence of approximately 2 degree. The pulse spatial radius is determined to ($r = 2.0 \pm 0.1$) mm. Both,

M^2 and r , are required for the calculation of beam waist and intensity of each pulse as a function of position z . A nearly spatial ($M^2 = 1.1 \pm 0.1$) and temporal Gaussian beam profile is verified using beam profile measurements and an autocorrelator, thus, fulfilling the experimental conditions of the z -scan technique to a great extent [31]. The as-prepared pulses are focused by lens L1 ($f = 150$ mm) and propagate through the lithium niobate crystal LN. The position of LN can be shifted along the direction of pulse propagation (z -coordinate) by means of a motorized linear stage (MLS). Incident and transmitted pulse energies are detected using biased Si-PIN detectors D1-D3 (Thorlabs, *DET10a*). The detectors D2 and D3 are equipped with opened and closed apertures, respectively, thus allowing for the determination of both nonlinear absorption and nonlinear index of refraction. Lenses L2-L4 focus the pulses to a spot size less than the photosensitive area of the detector.

All studies were performed with thin a -cut plates (aperture 8×6 mm², thickness $d = (260 \pm 10)$ μ m) of nominally pure LN grown from a congruently melting composition (Crys-Tec GmbH). The thickness ensures that the sample is much thinner than the Rayleigh length, avoiding asymmetric z -scan traces and effects of the group velocity dispersion (GVD). Front and back surfaces are carefully polished to optical grade nearly plane parallel (wedge below 5 arcmin). The one-photon absorption coefficient is determined to $\alpha = (0.16 \pm 0.1)$ cm⁻¹ for extraordinary ($\mathbf{e} \parallel c$) light polarisation and $\lambda = 488$ nm.

3.2. Experimental results

The experimentally determined z -scan traces are plotted in Fig. 4, exemplarily, for four pulse durations: (a) (70 ± 10) fs, (b) (220 ± 10) fs, (c) (430 ± 10) fs and (d) (840 ± 30) fs, all for a constant pulse energy of (270 ± 30) nJ and at a center wavelength of $\lambda = 488$ nm. The upper parts of the figures show the transmission T obtained from the signal ratio of diodes D2 and D1 as a function of z -coordinate from -15 mm to +15 mm. The travel range is chosen such that one-photon absorption dominates the transmission at ± 15 mm; the transmission is normalized to unity at $|z| > 15$ mm and shows a pronounced drop by scanning over the focus of the incident pulse. The minimum of transmission is used to define the position $z = 0$; all data sets are almost mirror-symmetric to $z = 0$. Qualitatively, the shape of the z -scan traces are comparable with each other for all pulse durations, and are characterized by a very low noise. A closer inspection reveals that the shape becomes narrower with increasing τ , which is a sign of higher order nonlinearities as discussed above (cf. inset of Fig. 2). In addition, and because of the adjustment of a constant pulse energy for all pulse durations, the varying peak intensity yields an increase of the transmission with increasing τ from $T \approx 20\%$ at 70 fs to $T \approx 45\%$ at 840 fs.

The data plots are analyzed by numerical solution of Eqs. (2) to (4). Fitting was performed iteratively by optimizing the squared error between fit and experimental data and the same model parameters for all data sets; the fitting results are shown as green curves in Fig. 4(a)-(d) with the following model parameters: a two-photon absorption coefficient of $\beta = (5.6 \pm 0.8)$ mm/GW, a small polaron absorption cross section of $\sigma = (210 \pm 70) \times 10^{-22}$ m², and characteristic times for electron-phonon relaxation of $\tau_S = 80$ fs, for interband relaxation of $\tau_R = 100$ fs and for small polaron formation of $\tau_{FC-P} = 100$ fs. A high degree of agreement is obvious from the inspection by eye over the entire range of scanning. The lower plots of Fig. 4(a)-(d) highlight the squared error of the fits with respect to the experimental data as a function of z with values much below 0.1% throughout the data set, typically below 0.03%. For comparison, the data sets have been also analyzed using Eq. (1), i.e. the z -scan theory considering two-photon absorption, only, yielding the red curves in Fig. 4(a)-(d). For the shortest pulse duration of 70 fs, the data can be modeled by the z -scan theory with very good coincidence, expressed by a squared error of below 0.1%. From this data set, the fit yields a two-photon absorption coefficient of $\beta = (5.8 \pm 0.8)$ mm/GW (for the nonlinear refractive index n_2 we obtained a value of about

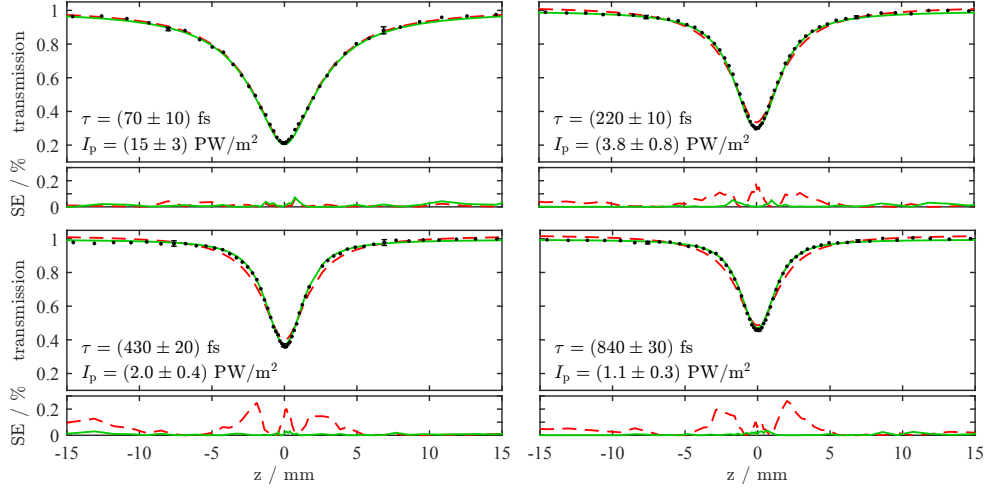


Fig. 4. (Upper parts): Experimentally determined transmission as a function of scanning coordinate z for four pulse durations: (a) (70 ± 10) fs, (b) (220 ± 10) fs, (c) (430 ± 10) fs and (d) (840 ± 30) fs, all for a constant pulse energy of (270 ± 30) nJ and at a center wavelength of $\lambda = 488$ nm. The results of our numerical fitting procedure according to Eqs. (2) to (4) are shown as green lines with the following model parameters: a two-photon absorption coefficient of $\beta = (5.6 \pm 0.8)$ mm/GW, a small polaron absorption cross section of $\sigma = (210 \pm 70) \times 10^{-22}$ m², and characteristic times for electron-phonon relaxation of $\tau_S = 80$ fs, for interband relaxation of $\tau_R = 100$ fs and for small polaron formation of $\tau_{FC-p} = 100$ fs. For comparison, fitting of Eq. (1) to the experimental data is shown as red dashed line. The error of a single measuring point is indicated by the errorbars for selected points. (Lower parts): squared error of the fits with respect to the experimental data as a function of z . It is noteworthy, that the amount of polaronic absorption, e.g. in (d) is about 45% at $z = 0$; the fit with Eq. (1) would result in an overestimate for β of about 15 mm/GW.

5×10^{-20} m²/W). For longer pulse durations, a deviation of the original TPA theory to the experimentally determined traces becomes obvious and is more pronounced with increasing pulse duration (exceeding a squared error of $\approx 0.2\%$). The evolution of *mean* squared errors (MSE) between fit and data set is plotted for both theoretical approaches in Fig. 5 for all measured pulse durations. Again, the plot highlights the excellent agreement of our model approach with the experimental data over the entire regime of pulse durations; a minimum value of mean squared error $MSE_{\min} = (1.5 \pm 0.1) \times 10^{-4}$ is reached throughout the pulse durations. The original z -scan theory describes the data with high precision in the regime of the shortest pulse durations (below 100 fs), as well. However, a characteristic rise of MSE of Eq. (1) becomes obvious for pulse durations ≥ 100 fs with a development that can be best described by a single-exponential growth function. We thus have fitted the function

$$MSE(t) = MSE(t = \infty) \times \left[1 - \exp\left(\frac{-(t - t_{\text{offset}})}{\tau_{\text{exp}}}\right) \right] + MSE_{\min} \quad (5)$$

to the data set yielding the following parameters: saturation amplitude $MSE(t = \infty) = (4 \pm 0.1) \times 10^{-4}$, characteristic time constant $\tau_{\text{exp}} = (137 \pm 8)$ fs, temporal offset of $t_{\text{offset}} = (86 \pm 5)$ fs, and minimum value of mean squared error $MSE_{\min} = (1.5 \pm 0.1) \times 10^{-4}$.

4. Discussion

From the experimental viewpoint, a very high quality of transmission traces are collected using the applied optical setup that represents an extension of the common z -scan technique. In particular, the important conditions of a Gaussian spatial profile is obtained, using a spatial frequency filter, and a Gaussian temporal profile is verified by autocorrelation measurements. A diode-pumped, regeneratively amplified Ti:Sa-laser system obeys an excellent beam profile and pointing stability and, thus, is ideally suited for generation of harmonic, Gaussian pulses by means of an optical parametric amplifier. The RMS noise of the pulse energy at the OPAs' output ($\ll 5\%$) could be reduced successfully by selection of incident pulses with equal pulse energy using diode D1. The disadvantage of this procedure is the extended measurement time, which is further enlarged by the low pulse repetition rate of 12.5 Hz and the two dimensional parameter range (z, τ) of our particular study. However, all these efforts are justified considering the outmost marginal deviations between the model approaches typically of below 0.03% (cf. Fig. 4).

As a superior result, a more detailed insight to the underlying physics of nonlinear absorption in lithium niobate is obtained, and clear evidence for small polaron formation and its contribution to nonlinear absorption is found. From the dependency of the shape of the z -scan trace as a function of pulse duration and its analysis, it is possible to derive a set of important material parameters that will be discussed in the following. First, the two-photon absorption coefficient $\beta = (5.6 \pm 0.8) \text{ mm/GW}$ is obtained from the complex numerical fitting procedure, that uses a single set of parameters for all pulse durations. Thus, the transmission is described throughout the regime of pulse durations from 70 fs – 1,000 fs with the same TPA coefficient – a result that is to be expected as β is a material parameter independent on τ . Considering the high quality of the numerical fits, a reliable value of β with an error of $\approx 15\%$ occurs for the LN crystal under investigation. Nearly the same value ($\beta = (5.8 \pm 0.8) \text{ mm/GW}$) is obtained using the original z -scan theory at the shortest pulse duration of $(70 \pm 10) \text{ fs}$, that underlines the reliability of the numerical fits.

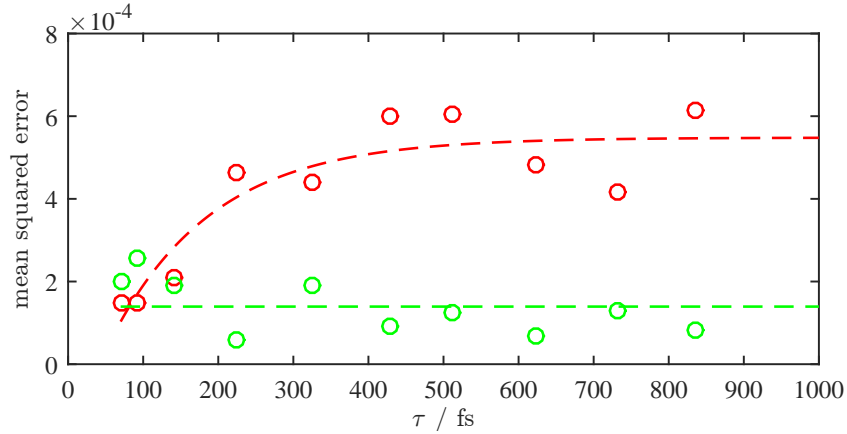


Fig. 5. Mean squared error between fit and experimental data for both, the numerical solution of our model approach according to Eqs. (2) to (4) (green), and the original z -scan theory using Eq. (1) (red). The dashed lines represent best fits with constant minimum value of the mean squared error $\text{MSE}_{\min} = (1.5 \pm 0.1) \times 10^{-4}$ (green) and a fit with Eq. (5) to the data points (red) with saturation amplitude $\text{MSE}(t = \infty) = (4 \pm 0.1) \times 10^{-4}$, characteristic time constant $\tau_{\text{exp}} = (137 \pm 8) \text{ fs}$, temporal offset of $\tau = (86 \pm 5) \text{ fs}$, and minimum value of mean squared error $\text{MSE}_{\min} = (1.5 \pm 0.1) \times 10^{-4}$.

bility of the obtained value. Moreover, it is an important (first) anchor for proving the action of our model approach as nonlinear absorption persists solely from TPA for pulse durations much below the small polaron formation time. The TPA value itself is much larger than the state-of-the-art knowledge in literature. For comparable pulse durations and photon energies, values of $\beta = 5.2 \text{ mm/GW}$ (80 fs, 400 nm, Mg-doped LN) [7] and $\beta = 3.5 \text{ mm/GW}$ (240 fs, $\approx 480 \text{ nm}$, nominally undoped LN) [17] are reported. Besides the possibility, that this difference may be attributed to the impact of small polaron absorption according to our model approach, we like to emphasize the role of stoichiometry on the TPA coefficient. It is well established, that the position of the band gap energy is strongly dependent on the crystals' stoichiometry. Being an absorption process of higher order, the transition probability for TPA is expected to change in accordance with the linear absorption feature [32]. Therefore, differences in the TPA coefficient may be due to differences in stoichiometry of the studied LN crystals, which seems to be very likely to us.

New insights are revealed to the relaxation dynamics of optically excited free carriers, characterized by τ_S . First evidence for this intermediate process was presented by Qiu et al. [6] performing time-resolved fs-absorption spectroscopy in Mg-doped LN crystals. As a remarkable characteristic of the small polaron formation dynamics, a temporal offset was discovered prior to the rise of small polaron absorption. No change of the transmission was observed during this temporal offset. A similar observation is reported in the work of Beyer et al. [8] using 240 fs laser pulses. Here, we also need to take into account a temporal offset prior to small polaron formation. In advance of the results of Qiu et al. [6], the time of the incident pulse does not need to be determined which is a particular feature of the approach of pulse duration scanning; the time constant τ_S is equal to the pulse duration where the transmission trace starts to alter its shape. Therefore, the temporal offset $\tau_S = 80 \text{ fs}$ can be determined with appealing precision. The lack of free-carrier absorption prior to carrier-phonon relaxation may be attributed either to the fact that the photon energy of the probing pulse is insensitive to the free-carrier absorption cross section or the carrier-phonon relaxation time τ_S falls much below the pulse duration ($\tau_S \ll (70 \pm 10) \text{ fs}$ in our case). However, the latter is unlikely because the carrier-phonon relaxation time exceeds 10^{-13} s in most semiconductors and for common optical phonon modes as pointed out in Ref. [22]. Further studies, particularly with shorter pulse durations need to be performed for clarification.

From the rise of the nonlinear absorption as a function of pulse duration we further obtain the small polaron formation time of $\tau_{\text{FC-P}} = 100 \text{ fs}$ in the numerical modeling procedure. This value is in good coincidence with the formation times obtained by transient absorption measurements [6, 7, 9]. Combining, however, our result on the presence of an offset time of $\tau_S = 80 \text{ fs}$ and the transient data from Sasamoto et al. using also very short, 80 fs pump and probe laser pulses [7], it is possible to conclude an upper limit of $\tau_{\text{FC-P}} \approx 100 \text{ fs}$. It is because the transmission loss due to two-photon absorption and due to small polaron absorption can not be resolved on the temporal axis in pump-probe experiments and overlap with each other.

It should be noted, that the small polaron formation time $\tau_{\text{FC-P}}$ is only related to small bound polarons ($\sigma_{\text{Nb}_{\text{Li}}^{4+}} = 4.0 \cdot 10^{-22} \text{ m}^2$, $\sigma_{\text{O}^-} = 4.1 \cdot 10^{-22} \text{ m}^2$ at 2.5 eV [5]). Due to the negligible absorption of small free polarons at our probing wavelength ($\sigma_{\text{Nb}_{\text{Nb}}^{4+}} = 0.8 \cdot 10^{-22} \text{ m}^2$ at 2.5 eV [5]), this type of polarons is (nearly) not detected in this experiment. Assuming, that the lattice relaxation of small free polarons is part of the small bound polaron formation path, the corresponding time constant must be considered as a part of τ_S . However, for a deeper insight a study at different wavelengths including the spectral range of small free polaron absorption is required.

Another parameter obtained from our study is the small polaron absorption cross section σ that is by more than one order of magnitude higher than the values published by Merschjann

et al. [5]. We note that it is not possible to find a converging numerical solution using Merschjann's value as fixed fitting parameter, even by neglecting relaxation of excited carriers to the ground state ($\tau_R = \infty$ results in a value of $\sigma \approx 110 \cdot 10^{-22} \text{m}^2$, still exceeding Merschjann's value by more than one magnitude). One explanation for the striking difference is an oversimplification of our model approach presented in section 2. In particular, the dynamics of holes with the possibility of O^- small hole polaron formation in LN [25] has been disregarded. As stated above, such holes obey nearly the same absorption cross section at a photon energy of 2.5 eV as it is the case for small bound $\text{Nb}_{\text{Li}}^{4+}$ polarons, although the maxima of the respective absorption features are fairly different (2.5 eV for O^- and 1.6 eV for $\text{Nb}_{\text{Li}}^{4+}$). Due to two-photon interband excitation it is reasonable to assume that the number density of optically generated electron $N_{p,e}$ and hole polarons $N_{p,h}$ is identical, $N_{p,e} = N_{p,h}$. As a consequence, it is necessary to exchange the factor σN_p in Eq. (2) by the sum $(\sigma_{p,e} N_{p,e} + \sigma_{p,h} N_{p,h}) = 2 \sigma_{p,e} N_{p,e}$. This means, that by considering small hole polarons, our numerical analysis is running with twice the polaron density. To counterbalance this value to correctly describe the experimentally determined contribution of small polaron absorption, the absorption cross section $\sigma_{p,e}$ needs to be reduced by a factor of two. Still, however, $\sigma_{p,e}$ exceeds the literature value. It is thus likely, that the larger value of σ may be attributed to a larger variety of different small polaron species. As individual types of small polarons are not resolved by our study, further pulse duration dependencies using different photon energies are required for a more quantitative analysis of this aspect. We like to add, that there is a severe difference in the boundary conditions of small polaron absorption between the study of Merschjann et al. [5] and the present one: Merschjann's cross sections were determined using pump-probe experiments, i.e. under the conditions of no light, whereas small polarons are inspected during the presence of a strong pump in our study, i.e. with light. Considering the presence of specific charge transport phenomena in LN, particularly of bulk photovoltaic currents [33], a difference in the absorption features of small polarons with and without light illumination can not be excluded.

It is noteworthy that all parameters discussed above and obtained from the rather complex numerical solution of Eqs. (2) to (4) show a correlation with each other. Particularly, the ratio between $\tau_{\text{FC-P}}$ and τ_R is not independent from other model parameters and directly impacts the density numbers N_{FC} and N_p as well as the polaron absorption coefficient σ . As a consequence, the characteristic times can be varied in a limited regime, only. The offset time τ_S can be varied between 70 fs and 90 fs while the polaron formation time is limited to $70 \text{ fs} < \tau_{\text{FC-P}} < 110 \text{ fs}$. At the same time, it is very reasonable that the increase of the number of fitting parameters in general results in the optimization of fitting functions. However, in the present case, the extension of the original z -scan theory by small polaron absorption is justified by the striking deviation of the transmission traces between theory and experimental data with increasing pulse duration. As this deviation rises after a characteristic offset time, the data plot of Fig. 5 showing the mean squared error as a function of pulse duration, can be applied also for the determination of the offset time τ_S yielding $\tau_S = t_{\text{offset}} = (86 \pm 5) \text{ fs}$ – in accordance with the numerical results of our model approach.

5. Summary and conclusion

The pulse duration dependency of nonlinear absorption has been studied in lithium niobate by means of z -scan technique over the time regime of 70 – 1,000 fs and has been analyzed from the viewpoint of small polaron formation using a numerical approach. It is shown, that the transmission loss of (ultra-)short laser pulses propagating through LN crystals can be described with remarkable precision and can be attributed to the complex interplay of near-instantaneous nonlinearities, particularly of two-photon and small-polaron absorption. Surprisingly, very minor

alterations in the shape of the well-known transmission traces of the z -scan technique result in severe changes in the set of nonlinear optical coefficients; for instance, using the original z -scan theory, the TPA coefficient β may be overestimated by a factor of three in the regime of long pulse durations.

Besides the precise determination of β or the absorption cross section of small polarons under illumination σ , the amount of information on the underlying photophysical processes obtained from our study is unexpectedly high: the proposed offset of transient absorption features during the time regime of electron-phonon cooling has been verified by experimental means and could be determined to (80 ± 10) fs. Furthermore, a more accurate regime of the small polaron formation time of 70 – 110 fs has been obtained.

These results are of utmost importance for the physics and microscopic modeling of the small polaron approach in LN [25, 26] and the further understanding of the small-polaron based bulk photovoltaic effect [33]. But also for the field of applications in nonlinear photonics as frequency converter – particularly in the growing field of ultrafast laser systems. In more general, the presented theoretical model and the experimental approach of pulse duration scanning can be transferred to the wide field of oxide materials showing small polaron formation and can be applied in the area of ultrafast lasers.

Acknowledgments

The authors gratefully acknowledge discussion from G. Corradi, L. Kovács (SZFKI, Hungary), and from A. Büscher. Financial support by the Deutsche Forschungsgemeinschaft, DFG (project numbers: IM 37/5-2, INST 190/137-1 FUGG, INST 190/165-1) is gratefully acknowledged.

A.2 Interference and holography with femtosecond laser pulses of different colours

ARTICLE

Received 28 Jun 2014 | Accepted 14 Nov 2014 | Published 5 Feb 2015

DOI: 10.1038/ncomms6866

Interference and holography with femtosecond laser pulses of different colours

Serguey Odoulov¹, Alexandr Shumelyuk¹, Holger Badorreck², Stefan Nolte², Kay-Michael Voit² & Mirco Imlau²

Interferometry and holography are two domains that are based on observation and recording of interference fringes from two light beams. While the aim of the first technique is to reveal and map the phase difference of two wave fronts, the main task of the second technique is to reconstruct one of the two recording waves via diffraction of the other wave from the recorded fringe pattern (hologram). To create fringes, mutually coherent waves from the same laser are commonly used. It is shown here that fringes can be observed and holograms can be recorded with ultrashort, sub-picosecond pulses even of different colour, generated in our experiment with two parametric amplifiers seeded, both by the same mode-locked Ti-sapphire laser. The appearance of permanent and transient gratings is confirmed by recording of an image-bearing hologram, by observation of two-beam coupling gain in a pump-probe experiment and by frequency conversion in Raman-Nath self-diffraction from a moving grating.

¹Optical Quantum Electronics Department, Institute of Physics, National Academy of Sciences, 46, Prospekt Nauki, 03 650 Kyiv, Ukraine. ²Department of Physics, Osnabrueck University, D-49076 Osnabrueck, Germany. Correspondence and requests for materials should be addressed to S.O. (email: odoulov@iop.kiev.ua) or to M.I. (email: mirco.implau@uni-osnabrueck.de).

The idea of wavefront recording and reconstruction, known today as holography, was formulated by Gabor¹. His proof-of-principle experiment was done with the light of a high pressure mercury lamp; it was necessary, however, to wait more than a decade for the invention of lasers to ensure holographic recording with really high quality of image reconstruction. A source of coherent radiation is necessary to form the interference pattern of the object wave and reference wave, that could be replicated in the recording material as a hologram. The important requirement to the light source is also its sufficiently large coherence length to ensure high enough contrast of fringes formed by different components of the object wave with the reference wave. Thus, it is universally accepted now that to record a hologram, both waves—object and reference—should be generated from the same laser, which emits, preferably, a single longitudinal TEM₀₀ mode.

In this article, we report on experiments aiming the holographic grating recording with two laser sources that generate, in addition, light with considerably different optical frequencies, more precisely blue and green light. The success of this counterintuitive experiment is ensured by using ultrashort, ≈ 100 fs pulses from two different optical parametric amplifiers (OPAs). In our particular experiment, the fringes formed by a blue beam with a green one are moving with a speed only three times smaller than light velocity. With 100 fs pulses, however, the displacement of the fringe pattern as a whole is less or comparable with one fringe spacing and the fringe contrast averaged over the pulse duration is still quite high.

The field of femtosecond holography is already well-established today by the successful demonstration of static holograms recording (see, for example, refs 2–5). So far, the recording was performed in a traditional way by beams from the same femtosecond laser, the spectral content of the two recording beams being identical. Also, starting from papers of Froehly *et al.*⁶ the so called ‘spectral holography’^{6–8} (and later ‘spectral nonlinear optics’⁹) was used for recording, reconstruction and processing of temporal envelopes of the short pulses. In a series of papers initiated by a publication of Buse *et al.*¹⁰, light with the wavelength other than that necessary for grating recording was used to improve the holographic sensitivity of the medium (some researchers called it ‘two-colour holography’). In all above papers, as also in similarly oriented other papers, the recording of permanent holographic gratings by beams with considerably different frequencies was never considered.

Our interest in grating recording with beams of different colour is motivated by its possible impact on the field of ultrafast optics, where the interaction of two or more ultrashort laser pulses within an optical medium is a common situation. The researchers face it in fundamental studies and in different applications, from frequency conversion to sensitive measurements of nonlinear constants of optical materials used in this domain.

At present, the absolute majority of papers that treat nonlinear interaction of two short pulses with different photon energies focus on a coupling that depends on the integral intensities, I_{pu} and I_{pr} (subscripts pu and pr mark pump and probe pulses, respectively). These intensities are different for different frequencies ω , depend on time t and propagation coordinate z . However, the interference of the pulse fields, that is, the small scale variations of total intensity in transverse direction x is disregarded in the case of different pulse frequencies. This can result in unexpected experimental observations or lead to misinterpretation of the obtained data sets, because the self-diffraction from the grating, which might be recorded by these fringes, brings by itself an additional direct beam coupling. The unusual result of our pump-probe experiments with LiNbO₃ crystal described below, in the beginning of the next section, serves as a

representative example. An example of possible application of the considered phenomenon, the frequency (up and down) conversion, is demonstrated, which is because of the Raman–Nath diffraction from the the moving grating recorded by pulses of different colours.

Results

Manifestation of self-diffraction in pump-probe experiments.

When trying to clarify the formation dynamics of small electron (or hole) polarons¹¹ in LiNbO₃, the normalized probe pulse transmission $\Delta T/T$ was measured in a range $-500 \text{ fs} \leq \Delta t \leq 1,000 \text{ fs}$ of the probe pulse delay times. These measurements have been performed within a broad spectral range of probe wavelength variation, $400 \text{ nm} \leq \lambda \leq 900 \text{ nm}$, with the intention to cover spectral manifestations of the small polarons, the pump wavelength being fixed at 490 nm.

Figure 1 shows the normalized probe pulse transmission $\Delta T/T$ as a function of the probe pulse delay time Δt with respect to the pump pulse. For large wavelength detunings (much larger than the full-width at half maximum (FWHM) of the pulse spectral content $\approx 5 \text{ nm}$) the measured dependence shows a well-known dip at $\Delta t = 0$, which is due to the two-photon absorption (blue data dots, see, for example, ref. 12). The unusual and intuitively unexpected feature is the observation of a probe pulse enhancement, instead of depletion, within a considerably large wavelength interval in the vicinity of total degeneracy. The amplification of the probe pulse with the wavelength 493 nm is shown in Fig. 1 by green dots.

The inset to the Fig. 1 gives the wavelength detuning dependence of a formally introduced exponential gain factor $\gamma = (1/\ell)\ln T$ (ℓ is the sample thickness). It suggests that the gain becomes large enough to overcome the two-photon absorption within the detunings range of $-3 \text{ nm} \leq \Delta\lambda \leq +8 \text{ nm}$. The processes of optical parametric amplification can be excluded in explanation of these findings, instead, the probe amplification by means of self-diffraction from a grating recorded by the pump and probe beams^{13,14} seems to be very probable. Several facts support this hypothesis, among them, the absence of gain in the case of cross-polarized pump and probe pulses and characteristic changes in the spectra of the amplified probe, with a signature of the pump pulse spectrum. Thus, the inertial grating recording with pulses that differ in wavelengths about 5 nm or more must be considered. The question arises, is such a recording possible at all and, if yes, how large the allowed frequency detuning can be.

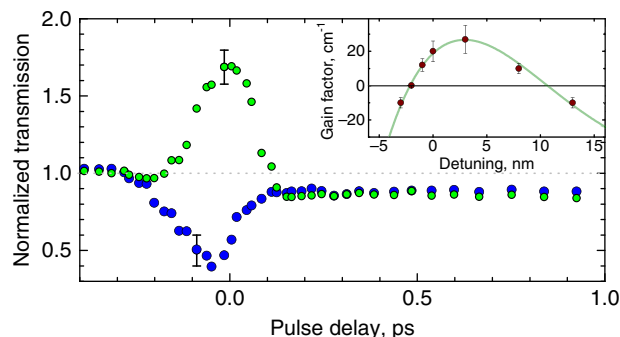


Figure 1 | Pump-probe experiment with LiNbO₃. The probe beam transmission versus time delay of the probe pulse with respect to the pump pulse. The wavelengths of the probe pulse are 485 nm and 493 nm for blue and green dots, respectively, the pump wavelength is ≈ 490 nm. The inset shows the detuning dependence of the net gain factor (amplification minus absorption) for probe and pump pulses matched in time.

These fundamental questions are addressed qualitatively and analytically below.

Qualitative considerations and estimates. After seminal publication¹, it became clear that to record a hologram the two light beams should be mutually coherent. One definition of mutual coherence relates it to the observable visibility of interference fringes formed by two beams that overlap in space^{15,16}. For continuous wave radiation, the observation of a high contrast fringe pattern is possible if both beams are nearly monochromatic and have identical frequencies. If two coherent light waves (1 and 2) have different frequencies, the fringe pattern that they form moves with the velocity $v = \Omega/K$ that depends on frequency detuning of the waves, $\Omega = \omega_2 - \omega_1$, and spatial frequency K ($\mathbf{K} = \mathbf{k}_2 - \mathbf{k}_1$, $\mathbf{k}_{1,2}$ being the recording beam wave vectors). Taking, for example, blue and green light waves with wavelengths 489 and 500 nm which intersect at an angle of 4° , we get the fringe velocity $v \approx 10^8 \text{ m s}^{-1}$. Figure 2 shows the structure of static fringes for the conventional case of hologram recording (for example, two red beams from continuous wave He-Ne laser) and moving fringes in case of interference of beams of two different colours.

Only the nonlinear processes with instantaneous response can follow the fringes that move with a velocity that is comparable with the velocity of light. Forty years ago the possibility to record

a dynamic hologram in a medium with ultrafast response was suggested by Denisjuk¹⁷. He called this effect ‘holography with intensity waves’. Nowadays, it can be implemented, for example, with two-photon absorption gratings^{18,19}, which will be discussed in the last section of this paper. The main objective of the present paper is, however, to prove that different colour recording of a holographic grating is possible in any medium, regardless how long is its response time, including media for permanent grating recording. To perform such a recording, we propose to take a snapshot of the moving fringes with a very short exposure time. A simple calculation allows for estimating the distance of fringe displacement $\Delta l = v\tau$ within the pulse duration τ . If this displacement is smaller or comparable with the fringe spacing $\Lambda = 2\pi/K$ the recorded fringe pattern will not be smeared out completely. This gives a hope that femtosecond lasers can be used for holographic grating recording by beams of different colours. The quantitative criteria for getting sufficiently high contrast of the pattern integrated over the pulse duration are derived in the next section.

Evaluation of the modulation depth. To calculate the modulation depth for a time-integrated fringe pattern as a function of the detuning frequency, we consider the interference of two pulses within the plane waves approximation. The electric field of two

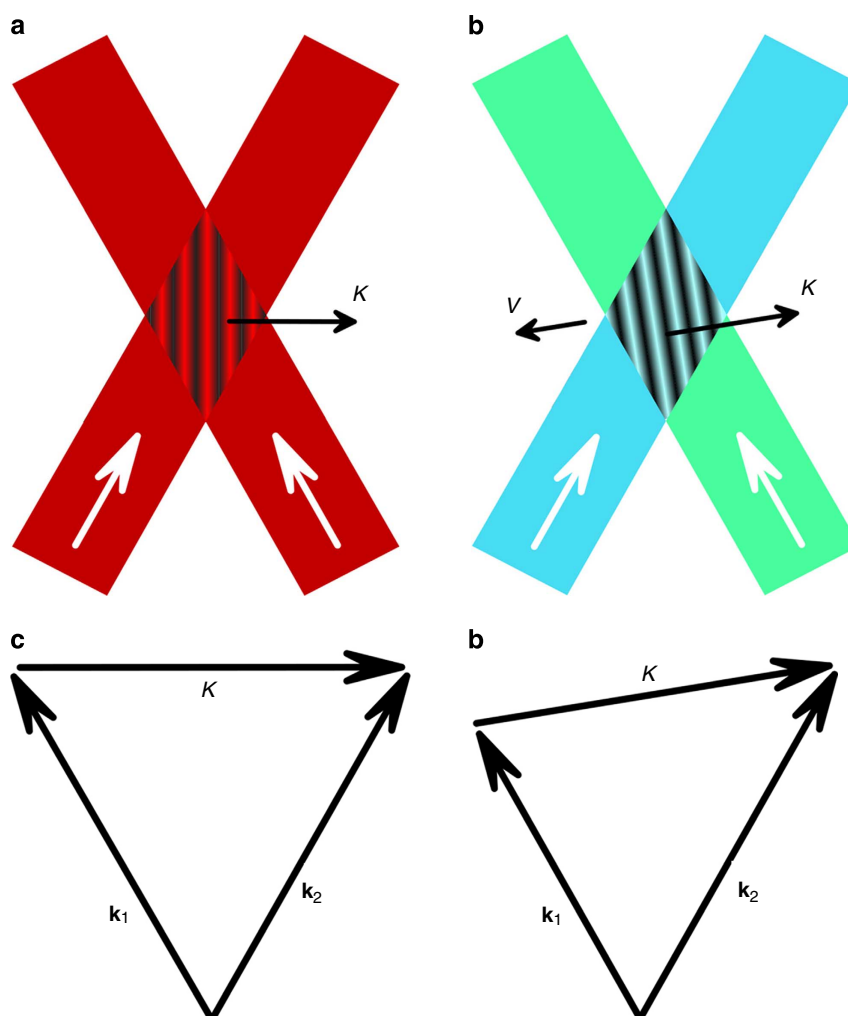


Figure 2 | Interference of two waves with identical and with different frequencies. Static fringes from two beams with (a) identical frequency spectrum and (b) fringes from beams of different colour that move with the velocity v . The relevant wavevector diagrams (c,d) are shown below the fringe patterns.

waves is

$$\begin{aligned} E_1(\mathbf{r}, t) &= a_1 f(t) \exp(-i\omega_1 t) \exp(-i\mathbf{k}_1 \mathbf{r}), \\ E_2(\mathbf{r}, t) &= a_2 f(t) \exp(-i\omega_2 t) \exp(-i\mathbf{k}_2 \mathbf{r}) \end{aligned} \quad (1)$$

with the amplitudes $a_{1,2}$, temporal shape $f(t)$, angular frequencies $\omega_{1,2}$ and wavevectors $\mathbf{k}_{1,2}$. The pulse duration $\tau = \tau_1 = \tau_2$ is defined by the FWHM of the intensity profiles $I_{1,2}(\mathbf{r}, t) = |E_{1,2}(\mathbf{r}, t)|^2$. The intensity distribution of the total field in time and space gives then a moving fringe pattern that is represented by

$$\begin{aligned} I(\mathbf{r}, t) &= |E_1 + E_2|^2 \\ &= (a_1^2 + a_2^2) f^2(t) + a_1 a_2 f^2(t) \exp(-i\Omega t + i\mathbf{K}\mathbf{r}) + \text{c.c.} \\ &= f^2(t) [a_1^2 + a_2^2 + 2a_1 a_2 \cos(\Omega t + \mathbf{K}\mathbf{r})]. \end{aligned} \quad (2)$$

Here $\Omega = \omega_2 - \omega_1$ denotes the frequency detuning and $\mathbf{K} = \mathbf{k}_2 - \mathbf{k}_1$ denotes the wavevector of the sinusoidal pattern. The pattern moves with the velocity $v = \Omega/K$ ($K = |\mathbf{K}|$) along \mathbf{K} , and its fringe contrast is given by $m = 2a_1 a_2 / (a_1^2 + a_2^2)$.

In our experiments, this fringe pattern is generated with ultrashort laser pulses ($\tau \approx 100$ fs), and the pulse duration is most often much shorter than the temporal response of the detectors used (digital camera, holographic emulsion and human eye). For single-pulse interference, this yields a time-integrated pattern of energy density per unit area:

$$\mathcal{E}(\mathbf{r}) = \int_{-\infty}^{+\infty} I(t, \mathbf{r}) dt. \quad (3)$$

Note, that $\mathcal{E}(\mathbf{r})$ depends on the temporal shape $f^2(t)$, thus on τ , as well as on the detuning frequency Ω . The modulation depth of the energy distribution $\mathcal{E}(\mathbf{r})$ is analyzed below by assuming three common $f(t)$ shapes: rectangular, Gaussian and hyperbolic secant. A rectangular pulse can be expressed by $f^2(t) = \text{rect}[t/\tau, -\tau/2]$ with an intensity that does not change within the total pulse duration τ . This particular shape of $I(t)$ simplifies the integration of equation (3)

$$\begin{aligned} \mathcal{E}(\mathbf{r}) &= \int_{-\tau/2}^{+\tau/2} I(t, \mathbf{r}) dt \\ &\propto a_1^2 + a_2^2 + 2a_1 a_2 \frac{\sin(\Omega\tau/2)}{\Omega\tau/2} \cos(\mathbf{K}\mathbf{r}), \end{aligned} \quad (4)$$

and allows to determine the modulation depth of the energy density pattern \bar{m} as a function of Ω and τ :

$$\bar{m}(\Omega, \tau) = \frac{2a_1 a_2}{a_1^2 + a_2^2} \frac{\sin(\Omega\tau/2)}{\Omega\tau/2} = m \frac{\sin(\Omega\tau/2)}{\Omega\tau/2}. \quad (5)$$

The two-dimensional plot of $\bar{m}(\Omega, \tau)$ is illustrated in Fig. 3a. The largest $\bar{m} = 1$ is reached, naturally, for $\Omega = 0$, whatever is the pulse duration τ . The detuning range within which the modulation depth is still high (the width of the central white stripe in Fig. 3a) depends, however, on pulse duration and increases quite strongly with decreasing τ . (It should be noted that for extremely short pulses (< 5 fs) the \bar{m} estimate according equation (5) is senseless because the fringe pattern width in \mathbf{K} -direction becomes comparable or smaller than the fringe spacing $2\pi/K$).

For any arbitrary τ (or arbitrary nonzero Ω) the frequency detuning dependence (or pulse length dependence) of \bar{m} shows additional maxima typical to sinc function. The \bar{m} -values of these maxima, as it follows from equation (5), are inversely proportional to the product $\Omega\tau$.

The sinc-like behaviour vanishes, however, completely under the assumption of a pulse temporal profile with a bell-shaped

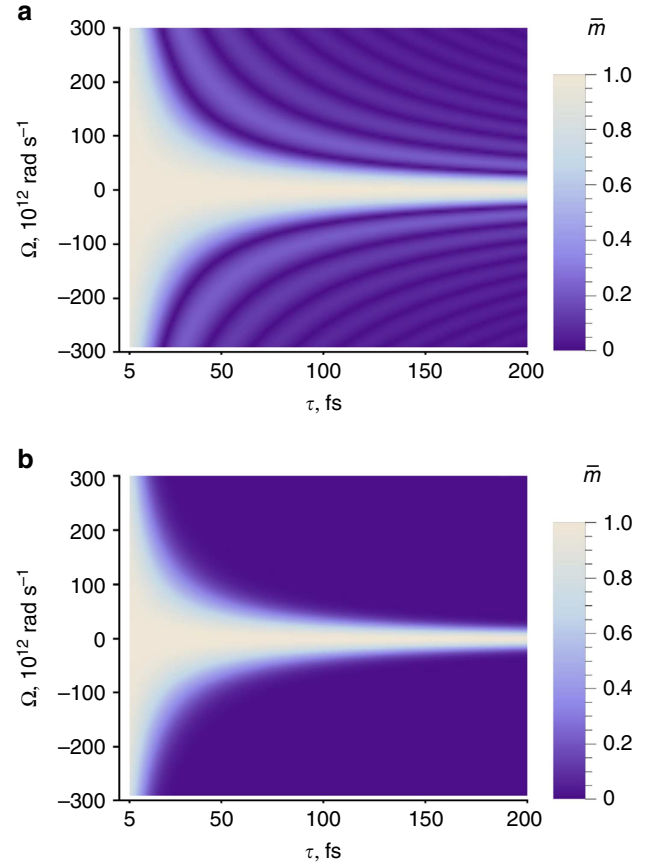


Figure 3 | Calculated modulation depth averaged over the pulse duration.

Modulation depth as a function of frequency detuning Ω and pulse duration τ for (a) rectangular and (b) Gaussian pulse profiles. The interaction of pulses with identical amplitudes is assumed.

function, particularly, for a Gaussian profile:

$$f^2(t) = \exp[-4 \ln(2) \cdot (t/\tau)^2] \quad (6)$$

or hyperbolic secant profile:

$$f^2(t) = \text{sech}^2[2 \cosh^{-1}(\sqrt{2}) \cdot t/\tau], \quad (7)$$

τ being the FWHM in both cases. Integration of equation (3) then yields:

$$\begin{aligned} \bar{m}(\Omega, \tau) &= \frac{2a_1 a_2}{a_1^2 + a_2^2} \exp\left(-\frac{\tau^2 \Omega^2}{16 \ln(2)}\right) \\ &= m \exp\left(-\frac{\tau^2 \Omega^2}{16 \ln(2)}\right) \end{aligned} \quad (8)$$

and

$$\bar{m}(\Omega, \tau) = m \frac{\pi\tau\Omega}{4 \sinh^{-1}(1)} \text{csch}\left(\frac{\pi\tau\Omega}{4 \sinh^{-1}(1)}\right). \quad (9)$$

Figure 3b shows the $\bar{m}(\Omega, \tau)$ plot for a Gaussian profile, the plot for a hyperbolic secant profile is qualitatively similar. The characteristic difference between the modulation depth of rectangular, Gaussian and sech pulses is highlighted in Fig. 4 for a fixed detuning of $\Omega = 3 \times 10^{13} \text{ rad s}^{-1}$ as a double-logarithmic plot. The modulation depth for Gaussian and sech pulses drop as a function of pulse duration in a similar way, while the decay for rectangular pulses is not so strong and is characterized by an oscillatory behaviour.

From the viewpoint of our pump–probe experiment described above ($\Omega \approx 3 \times 10^{13} \text{ rad s}^{-1}$ and $\tau \approx 100 \text{ fs}$), it becomes clear that the modulation depth is $\overline{m}(\Omega, \tau) \approx 0.4$ for a Gaussian pulse (≈ 0.6 for a rectangular pulse), that is, a fringe pattern with sufficiently high modulation depth is present and is able to cause the recording of a grating.

Note, that the generalization to the case of repetitive rate excitation is natural, provided the phase difference of waves in equation (1) does not change from one pulse to the other. The modulation depth is not affected by the number of pulses N because all terms in equation (3) are multiplied to the same number of pulses N .

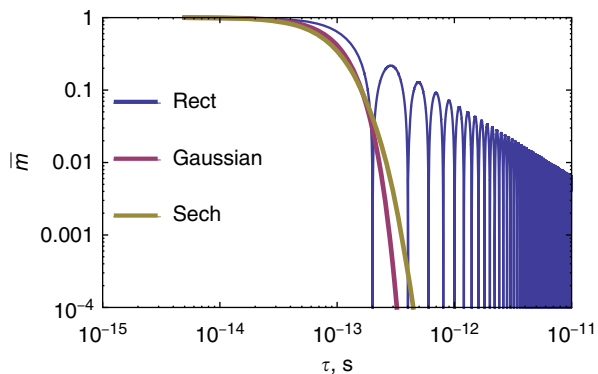


Figure 4 | Effect of the pulse temporal profile on modulation depth. Comparison of the modulation depth as a function of pulse duration τ for rectangular, Gaussian and hyperbolic secant pulses. A fixed frequency detuning of $\Omega = 3 \times 10^{13} \text{ rad s}^{-1}$ and equal intensities of two pulses are assumed.

Visualization of interference fringes. The visual observation of two-colour beam interference becomes possible by adjusting a small angle between the beams. We note that the fringe velocity v depends on the fringe spacing Λ , but the condition $v\tau/\Lambda \leq 1$ does not impose any restriction to Λ . Thus, the observable fringe contrast should be independent of the angle between the recording beams, and a fringe spacing can be adjusted to be large enough for detection with the naked eye.

The schematic representation of the experiment on fringe observation and grating recording is shown in the upper left corner of Fig. 5. The temporal overlap of pulses from two OPAs on a diffusing white screen is ensured with an optical delay line. With this arrangement, it is possible to observe a fringe pattern on the screen and to register its image.

The very first attempt revealed distinct fringes for quite different wavelengths, that were visible both with single shot and in repetition rate operation mode. An example is shown in Fig. 5 that represents fringes from the beams with 17 nm wavelength detuning. Care is taken to get a uniform transverse intensity distribution in both beams and a good superposition of the spots with nearly equal diameter. The two beams were identically linearly polarized, perpendicularly to the drawing of Fig. 5. The full angle between the beams was deliberately chosen here to be nearly 0.5° to increase the fringe spacing.

The described observation is a purely ‘linear optic’ effect, any kind of nonlinearity is not involved here. The beams interfere only when they are superposed in space and in time. If the observation screen is moved so that the light spots are completely separated, the fringes are no more visible.

The fact that a fringe pattern could be observed with naked eye at 1 kHz repetition rate proves that spatial position of fringes remains the same from one pulse to the other, at least during the

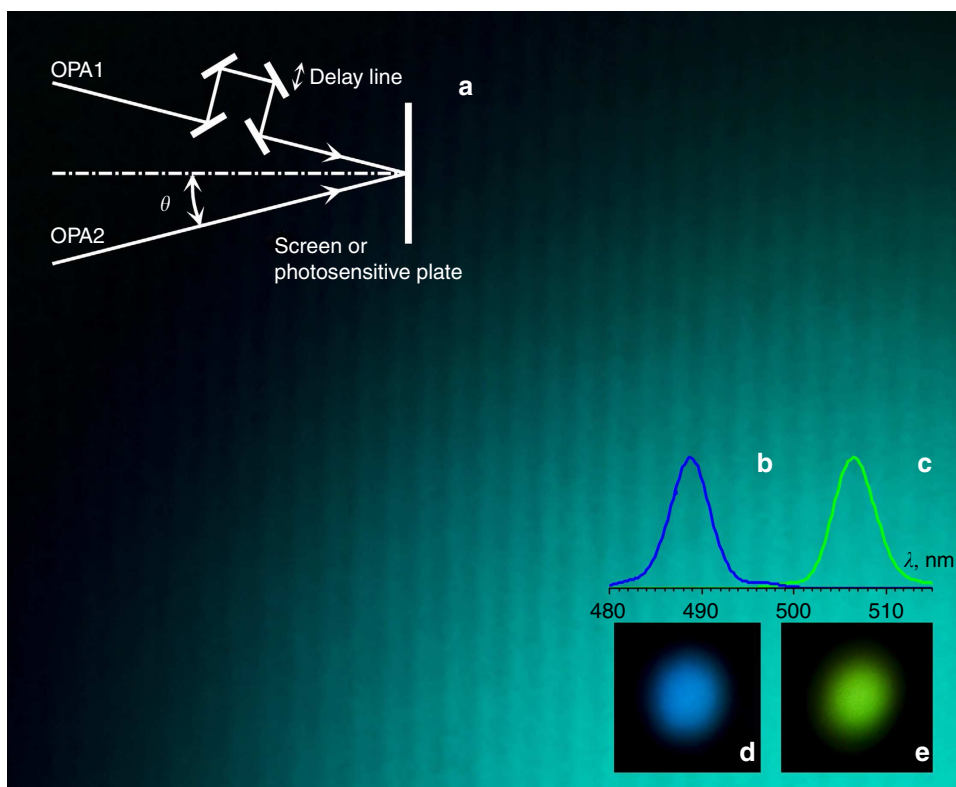


Figure 5 | Observation of fringe pattern from light beams of different colours. The background image shows a fragment of a fringe pattern from single-pulse light beams with $\lambda = 489$ and 506 nm . The geometry of fringe observation (a) is shown in upper left corner. The net difference in colours of two beams is clearly seen from measured spectra (b,c), and from near-field distributions (d,e).

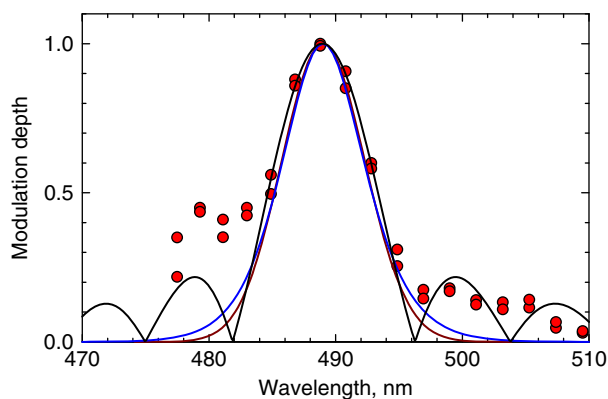


Figure 6 | Wavelength detuning dependence of the modulation depth.

Dots represent the data measured with a fixed wavelength, 488 nm, of one beam and the wavelength variable within the range 475–510 nm for the other beam. Solid lines represent the dependences calculated within the assumption of the rectangular (black), Gaussian (deep red) and hyperbolic secant (blue) temporal envelopes of the interfering pulses.

physiological limit of the human eye response (about 0.04 s). Later this was confirmed when recording the grating with several consecutive pulses: the contrast of the recorded pattern did not deteriorate as compared with single-pulse recording. Such a feature could be expected as one and the same mode-locked Ti:Sapphire laser is initially feeding the two channels in which the recording beams are formed. For both recording beams, the phase of every new pulse in train is not arbitrary and the effective phase difference is preserved from pulse to pulse.

It should be underlined, however, that for the case of single-pulse experiment no restrictions are imposed for the light sources that provide two interfering beams: they can be the two completely independent lasers with the outputs of different colour, that in common sense would be considered completely mutually incoherent. The only necessary condition for fringe observation is the spatial and temporal overlap of output ultrashort pulses and their polarization adjustment. In case of repetition rate experiment, there are a few additional requirements—the repetition rates of the two beams should be exactly the same and the coherence time of each beam should be longer than the total time of fringe recording (or fringe observation). As it was mentioned above, these conditions were met in full with the femtosecond laser system used in our experiment.

Modulation depth versus wavelength detuning. The digitized image like that shown in Fig. 5 allows for evaluating the recorded fringe modulation depth $\bar{m} = (I_{\max} - I_{\min}) / (I_{\max} + I_{\min})$. These measurements were done for a series of fringe patterns that have been taken with the fixed wavelength of one OPA $\lambda_1 = 489$ nm and variable wavelength of the other OPA. The processing of digitized images and extraction of \bar{m} from the raw data are described in the Methods section.

Measurement of fringe contrast. Figure 6 shows the detuning dependence of the fringe contrast (dots). The accuracy of \bar{m} estimate is high for small frequency detunings, the uncertainty increases up to $\approx 30\%$ for largest measured detunings, where the modulation depth becomes small.

The attempts to fit the measured data with functions calculated in previous section for different intensity profiles of the recording pulses are given by the solid lines: black line represents a $\text{sinc}(\Omega\tau/2)$ dependence for rectangular pulses; the fit yields

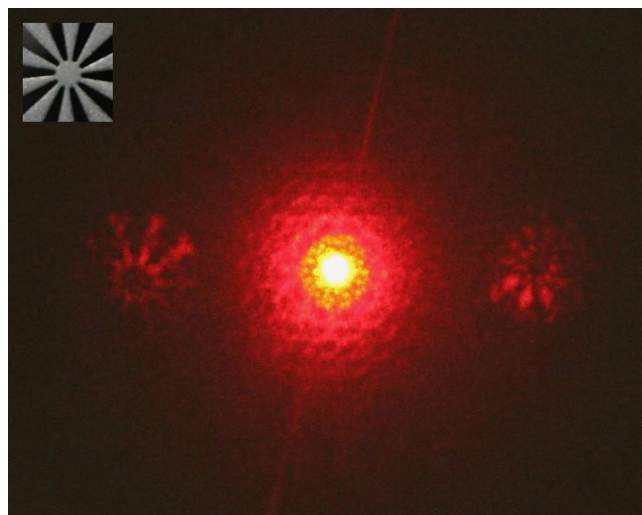


Figure 7 | Image reconstruction from a hologram recorded with pulses of different colour.

Readout with a He-Ne laser of the hologram written by femtosecond pulses with 489 and 501 nm wavelengths. The inset in the upper left corner shows the amplitude mask installed in one of the two beams during recording; grey color marks the areas with zero transmission.

$\tau \approx 110$ fs for the pulse duration. The fitting of functions calculated for Gaussian and hyperbolic secant profiles gives a somewhat smaller pulse duration, about 80 fs. In all cases, however, the estimated values are in reasonable agreement with the directly measured pulse duration of about 100 fs.

Grating recording and hologram recording. The fringe pattern that can be seen with the eye can also be recorded with a photosensitive medium. Such an imprint of fringes represents a plane wave hologram. They were recorded using conventional silver halid photo emulsions with standard chemical development and subsequent bleaching procedure. For close wavelengths of the two recording beams, the ± 2 diffraction orders are clearly seen and the diffraction efficiency in the first order is a few per cent.

In the limit of small phase modulations the diffraction efficiency η depends quadratically on fringe contrast \bar{m} (ref. 20). Thus the decrease of \bar{m} with the increasing detuning (see Fig. 6) should inhibit diffraction. Just this behaviour was observed experimentally.

We also registered a hologram in a photoemulsion with an image-bearing beam. The amplitude mask shown in the upper left corner of Fig. 7 was installed in one of the two recording beams (green beam), which is loosely focused. The angle between the recording beams was increased to 4° to ensure that the carrier spatial frequency K of a hologram was larger than the spatial frequency content of the image. Figure 7 shows the reconstructed images, the pseudoscopic on the left side and orthoscopic on the right side from the central spot, which represents the transmitted readout beam from the He-Ne laser. The reconstructed images are quite noisy, however one can recognize unambiguously the original pattern.

Discussion

It is shown in this paper that the contrast of time average interference pattern of two short light pulses of different colour can be remarkably high at least for frequency detuning $|\Omega| \leq 2\pi/\tau$. As it follows from the data of Fig. 6, the experimental detuning dependence of the modulation depth has rather extended, slightly waving wings. When comparing this result with calculations, one can see that the measured values of \bar{m} for $|\Omega| \geq 2\pi/\tau$ are obviously

larger than that expected for Gaussian and hyperbolic secant temporal profiles. This may point to a pulse shape that is certainly not rectangular but doesn't also have smoothly decaying wings typical for Gaussian and hyperbolic secant functions. The evident asymmetry of $\bar{m} = \bar{m}(\Delta\lambda)$ dependence can be attributed to the changes of pulse shape and width with the detuning.

It should be noted that the problem of effective fringe visibility can be considered not only in time domain, what we did above, but also in the frequency domain. Obviously, a considerable reduction of the pulse duration leads to the broadening of its spectrum. Even a slight spectral overlap of the two pulses may lead to the appearance of a fringe pattern with finite modulation depth.

For the case of transform limited pulses, the pulse-bandwidth product is $\Delta\nu \times \tau = \kappa$. The factor κ is close to unity and depends on the particular pulse shape, for Gaussian pulses $\kappa = 2\ln(2)/\pi$ holds²¹. Therefore, the modulation depth for Gaussian pulses (see equation (8)) can be rewritten in terms of the detuning frequency Ω and the spectral width $\Delta\omega$ of the pulses (with $\nu = \omega/2\pi$):

$$\bar{m}(\Omega, \Delta\omega) = m 2^{-\left(\Omega/\Delta\omega\right)^2}. \quad (10)$$

Taking the experimental conditions $\lambda_1 = 489$ nm, $\lambda_2 = 506$ nm and $\tau = 100$ fs, we get $\Omega/\Delta\omega \approx 4.7$ for an assumed Gaussian shape, which indicates a small overlap which is due to the extended wings of gaussian pulses as it is shown in right hand side of Fig. 5.

Summarizing, we claim that with 100 fs pulses a recording of holographic grating is possible if the frequencies of two pulses differ up to 4% of the mean optical frequency (larger detunings are allowed for shorter pulses). Of course, when read out with one of the two recording beams, a recorded static hologram can not reproduce the wavelength of the other beam. With some distortions it can reproduce, however, the recorded wavefront.

For classical holography the described phenomenon is rather unexpected and obviously new. It can bring new technical solutions for static hologram recording of ultrafast processes, including new variations of Nils Abramson's light-in-flight holography^{2,22}.

We believe, however, that our result will have a major impact in nonlinear wave mixing and nonlinear spectroscopy. The appearance of transient or permanent grating recorded by two interacting waves may strongly influence the interpretation of pump-probe experiments. Our results described above prove that a direct coupling from such a grating because of self-diffraction affects both the intensity and the spectrum of the probe beam. We limited ourselves in the present paper by consideration of permanent gratings only, as an ultimate case of recording in a material with the infinite storage time. In fact, a vast variety of χ^3 nonlinearities with response times ranging from practically zero to infinity can respond to the described moving fringe pattern, thus bringing particular types of coupling.

Apart from the coupling because of self-diffraction, the transient gratings can be revealed through the appearance of higher (non Bragg) orders in case of Raman-Nath diffraction. In media with instantaneous response (other ultimate case compared with described above) the higher orders of diffraction should be upshifted and downshifted in frequency exactly by the frequency difference of the recording waves Ω . Our preliminary experiments with different colour recording of two-photon absorption gratings, that are currently in progress and will be published separately, confirmed the possibility of building such a tunable frequency converter. Figure 8 shows an example of up and downconversion to $\Delta\lambda \approx 25$ nm with self-diffraction from the moving two-photon absorption grating in a thin sample of LiNbO₃. The severe fundamental restriction on the diffraction efficiency for amplitude gratings²⁰ resulted in only 0.01 conversion efficiency in this demonstration experiment. A

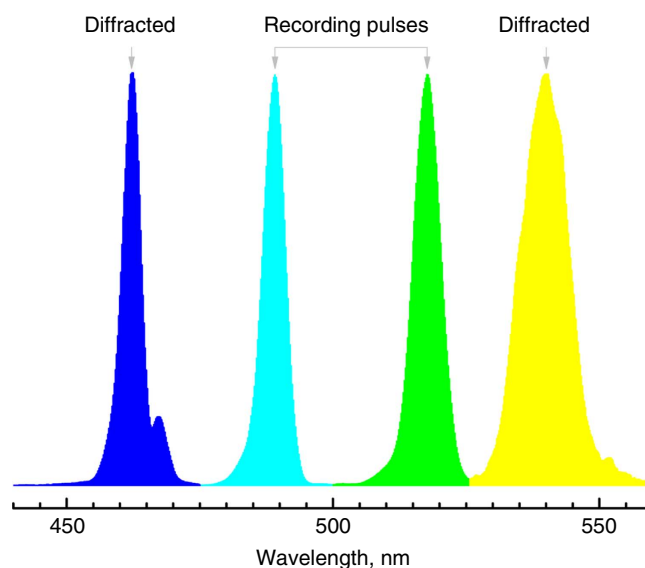


Figure 8 | Frequency conversion via self-diffraction from a moving dynamic grating. Spectra of the transmitted recording pulses and ± 1 diffraction orders. The thin two-photon absorption dynamic grating is recorded in a 200- μm thick sample of LiNbO₃ by beams that differ by ≈ 25 nm in wavelength and impinge upon the sample at a full angle of $\approx 4^\circ$.

considerable improvement of efficiency is expected with purely phase moving gratings, profiting from the dominant real part of χ^3 nonlinearities.

A hologram recording in Leith-Upatnieks geometry, with an oblique reference wave, is demonstrated in this article. Taking into account that even in dense media the spatial width of 100 fs pulse is not $< 10 \mu\text{m}$, the reflection gratings and Lippman-type (reflection) holograms can be recorded by counterpropagating light pulses, too. This allows also for considering different applications based on nonlinear backward wave four wave mixing with ultrashort pulses.

Dynamic grating techniques have been used successfully in the past for the development of autocorrelation-type measurements of femtosecond pulse duration³. With pulses of different colour, this technique can be extended for cross-correlation experiments. The studies of gratings with instantaneous response recorded by pulses of different colours will be profitable for evaluation of a frequency chirp in ultrashort pulses, that is, the short pulse characterization will be another domain to apply the described phenomenon.

Finally, this work will trigger new attempts to reconsider the definition of coherence for pulsed radiation. In particular, the question will be discussed—can the blue pulse and green pulse from two different lasers be considered mutually coherent?

Methods

Laser system and optical set-up. The femtosecond laser system used in the experiment consists of several separate devices in chain; Fig. 9 shows it schematically. A mode-locked Ti³⁺:Al₂O₃ oscillator generates the initial train of femtosecond pulses with a spectrum centred at wavelength $\lambda = 802$ nm. Chirped-pulse amplification is used to reach a maximum pulse energy of (4 ± 0.1) mJ at a repetition rate of 1 kHz. By tuning the compressor grating (C), the pulse duration is adjusted to (100 ± 10) fs, as determined by interferometric auto correlation (Gaussian shape approximation, A.P.E., model: Pulse Check PD 15 ps). The pulses then enter two OPAs (OPA (1) and OPA (2)) with input pulse energies of ≈ 2.5 mJ and ≈ 1.5 mJ, respectively, after passing a telescope and a 65:35 beam splitter.

Both OPAs use a supercontinuum source of Al₂O₃ for the signal generation, and a double-stage parametric amplifier scheme (non-collinear and collinear optical amplifier) for signal amplification. Pulses in the blue-green spectral range (470–520 nm) are obtained within a sum-frequency mixing scheme. At the OPA

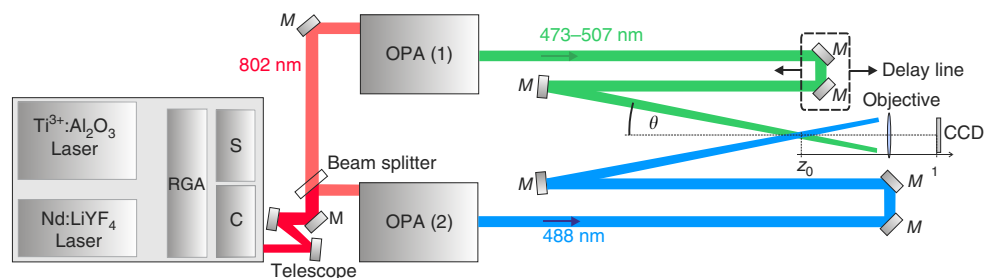


Figure 9 | Experimental set-up. Femtosecond pulses from a $\text{Ti}^{3+}:\text{Al}_2\text{O}_3$ laser are stretched (S) to the picosecond length, regenerative amplified (RGA) using a $\text{Ti}^{3+}:\text{Al}_2\text{O}_3$ that is pumped by a Q-switched Nd:LiYF₄ laser ($\lambda = 527$ nm) and compressed (C) to pulses with 100 ± 10 fs duration and 4 mJ energy (Coherent Inc., LIBRA-HE). The amplified femtosecond pulses serve as a pump for two optical parametric amplifiers (OPA, Coherent Inc., OPerA Solo) to generate femtosecond-laser pulses in the blue-green spectral range via sum-frequency conversion. The optical path lengths of the frequency-detuned pulses is adjusted by a delay line. The pulses are superimposed at a small angle in air, so that the fringe pattern could be imaged onto a screen with lens L.

output, pulse energies up to 150 μJ are available with pulse durations < 100 fs. The optical paths of the frequency-detuned pulses are matched by using an optical delay line in one of the beams.

For the generation of a fringe pattern, the pulses are superimposed at an angle of a few degrees in air at position z_0 . The pattern is imaged by a lens (magnification factor: $\times 50$) onto a screen and grabbed by a digital camera. A metallic mask was placed in one of the two beam paths to demonstrate holographic image recording with a holographic emulsion (Slavich, PFG-03M) at z_0 . The exposed films were chemically processed and reconstructed by a He-Ne laser.

Pump-probe experiment. The transmittance of a 200- μm thick y -cut sample of a nominally undoped LiNbO_3 crystal was tested with the an ≈ 100 -fs probe pulse in presence of pump pulse with the same duration. The average intensities of the pump and probe pulses were 5.6 PW cm^{-2} and 0.7 TW cm^{-2} , respectively. Both pulses, probe and pump, are identically and linearly polarized along the crystal c -axis, they impinge upon the sample in a plane normal to this axis, to avoid a photorefractive grating formation. The spectrum of the pump pulse is fixed at 490 nm while the wavelength of the probe pulse is tunable. The 100 μm beam waist of the probe pulse is roughly 1.5 times smaller than that of the pump pulse. For the wavelength range used in the experiment, even with relatively small full angle between the beams ($\approx 2.5^\circ$) at least 10 interference fringes are expected within the area where two beams overlap.

No cumulation effects have been observed; the measurements are done either within a single short pulse or by averaging the data of consecutive 10 pulses.

Measurements of fringe contrast. To extract the data on fringe contrast from the digitized image of interference pattern, two problems must be solved. First, one needs to be sure that the recording device (digital camera in our case) works within the intensity range where its response to the intensity is linear. Second, for any particular pattern to be processed it is necessary to know the intensity ratio of two interfering beams.

Initially the intensity ratio of two waves with identical frequencies was adjusted to be 1:1, it was, however, changing when the frequency of one wave was tuned. Thus, there are two reasons for decreasing the measured modulation depth with the detuning frequency, one is related to variation of the intensity ratio and the other is related to the fringe pattern motion.

Whole-measurement procedure was as follows. At first, the two beams were superposed in a best way on a white screen. Then, the digital camera with the removed lens was installed so that its sensitive matrix appeared in a plane of white screen, just in the maximum of the intensity spatial distribution. The matrix dimension, $17 \times 22 \text{ mm}^2$, was roughly 10 times smaller than the FWHM of the interfering beams. The linearity of camera response was ensured by appropriate choice of neutral density filters. To find the intensity ratio of the recording waves, the three measurements were done for every new frequency detuning: the measurements of each interfering beam separately and the measurement of fringes from two superposed beams. Figure 6 shows the recalculated detuning dependence of the fringe contrast (dots), which is due to the fringe motion only.

References

- Gabor, D. A new microscopic principle. *Nature* **161**, 777–778 (1948).
- Abramson, N. Femtosecond imaging: motion picture of short pulses. *Nat. Photonics* **5**, 389–390 (2011).
- Brubaker, R. M., Wang, Q. N., Nolte, D. D., Harmon, E. S. & Melloch, M. R. Steady-state four-wave mixing in photorefractive quantum wells with femtosecond pulses. *J. Opt. Soc. Am. B* **11**, 1038–1044 (1994).
- Horowitz, M., Fischer, B., Barad, Y. & Silberberg, Y. Photorefractive effect in a BaTiO_3 crystal at the 1.5 μm wavelength regime by two-photon absorption. *Opt. Lett.* **21**, 1120–1122 (1996).

- Hsieh, H.-T. *et al.* Femtosecond holography in lithium niobate crystals. *Opt. Lett.* **30**, 2233–2235 (2005).
- Froehly, C., Colombbeau, B. & Vampouille, M. Shaping and analysis of picosecond light pulses. *Prog. Opt.* **20**, 63–153 (1983).
- Weiner, A. M., Leaird, D. E., Reitze, D. H. & Paek, E. G. Femtosecond spectral holography. *IEEE J. Quant. Electron.* **28**, 2251–2261 (1992).
- Oba, K., Sun, P.-C. & Fainman, Y. Nonvolatile photorefractive spectral holography. *Opt. Lett.* **23**, 915–917 (1998).
- Mazurenko, Y. T. *et al.* Ultrafast time-to-space conversion of phase by the method of spectral nonlinear optics. *Opt. Lett.* **21**, 1753–1755 (1996).
- Buse, K., Adibi, A. & Psaltis, D. Non-volatile holographic storage in doubly doped lithium niobate crystals. *Nature* **393**, 665–668 (1998).
- Imlau, M. *et al.* Hologram recording via spatial density modulation of $\text{Nb}_{\text{Li}}^{4+/5+}$ antisites in lithium niobate. *Opt. Exp.* **19**, 15322–15338 (2011).
- Kang, I., Krauss, T. & Wiese, F. Sensitive measurement of nonlinear refraction and two-photon absorption by spectrally resolved two-beam coupling. *Opt. Lett.* **22**, 1077–1079 (1997).
- Eichler, H. J., Günter, P. & Pohl, D. W. *Laser Induced Dynamic Gratings* (Springer-Verlag, 1986).
- Vinetsky, V. L., Kukhtarev, N. V., Odoulov, S. G. & Soskin, M. S. Dynamic self-diffraction of coherent light beams. *Sov. Phys. Usp.* **22**, 742–756 (1979).
- Mandel, L. & Wolf, E. *Optical Coherence and Quantum Optics* (Cambridge University Press, 1995).
- Glauber, R. *Quantum Optics and Electronics* (Gordon and Breach, 1965).
- Denisjuk, Y. On reconstructive abilities of the running intensity waves when recording the dynamic 3D holograms. *Sov. Phys. Tech. Phys.* **44**, 131–133 (1974).
- Shumelyuk, A. *et al.* Self-diffraction from two-photon absorption gratings in $\text{Sn}_2\text{P}_3\text{S}_6$. *Opt. Lett.* **37**, 4065–4067 (2012).
- Imlau, M., Dieckmann, V., Badorreck, H. & Shumelyuk, A. Tin hypophosphite: nonlinear response in the sub-100 fs time domain. *Opt. Mater. Exp.* **1**, 953–961 (2011).
- Collier, R. J., Burckhardt, C. B. & Lin, L. H. *Optical Holography* (Academic Press, 1971).
- Menzel, R. *Photonics: Linear and Nonlinear Interactions of Laser Light and Matter*, 2nd edn (Springer Science & Business Media, 2007).
- Abramson, N. Light-in-flight recording by holography. *Opt. Lett.* **3**, 121–123 (1978).

Acknowledgements

We thank Professor Dr Eckhard Krätzig and Dr Javid Shirdel for fruitful discussions. Financial support of Deutsche Forschungsgemeinschaft via projects IM37/5-2, INST 190/137-1 FUGG and INST 190/165-1 and of the Alexander von Humboldt Stiftung via Research Award to S.O. is gratefully acknowledged.

Author contributions

S.O. and M.I. formulated the idea and initiated the project; A.S. conceived the experiment; A.S., H.B., S.N. and M.I. carried out the experiment; S.O., A.S., H.B. and K.-M.V. made calculations; S.O. and M.I. wrote the paper. All authors discussed the results and contributed to the final manuscript.

Additional information

Competing financial interests: The authors declare no competing financial interests.

Reprints and permission information is available online at <http://npg.nature.com/reprintsandpermissions/>

How to cite this article: Odoulov, S. *et al.* Interference and holography with femtosecond laser pulses of different colours. *Nat. Commun.* 6:5866 doi: 10.1038/ncomms6866 (2015).

A.3 Doppler-shifted Raman-Nath diffraction from gratings recorded in LiNbO_3 with ultra-short laser pulses of different color

Doppler-shifted Raman-Nath diffraction from gratings recorded in LiNbO₃ with ultra-short laser pulses of different color

Holger Badorreck,¹ Alexandr Shumelyuk,² Stefan Nolte,¹
Mirco Imlau¹ and Serguey Odoulov^{2,*}

¹*School of Physics, Osnabrück University, D-49076 Osnabrück, Germany*

²*Institute of Physics, National Academy of Sciences, 03 650 Kyiv, Ukraine*

[*odoulov@iop.kiev.ua](mailto:odoulov@iop.kiev.ua)

Abstract: Nominally undoped LiNbO₃ crystals feature a pronounced mixed (absorption/refraction) nonlinear response in the blue-green spectrum domain that is sufficient for the excitation of moving dynamic gratings and the observation of selfdiffraction with Doppler shifted higher orders. This type of Raman-Nath selfdiffraction can be successfully used for up- and down- frequency conversion as well as for characterization of the recording pulses.

© 2016 Optical Society of America

OCIS codes: (320.2250) Femtosecond phenomena; (090.0090) Holography.

References and links

1. M. Horowitz, B. Fischer, Y. Barad, and Y. Silberberg, "Photorefractive effect in a BaTiO₃ crystal at the 1.5- μ m wavelength regime by two-photon absorption," *Opt. Lett.* **21**, 1120–122 (1996).
2. Hung-Te Hsieh, D. Psaltis, O. Beyer, D. Maxein, C. von Korff Schmising, K. Buse, and B. Sturman, "Femtosecond holography in lithium niobate crystals," *Opt. Lett.* **30**, 2233–2235 (2005).
3. A. Shumelyuk, M. Imlau, V. Dieckmann, H. Badorreck, A. Grabar, and S. Odoulov, "Self-diffraction from two-photon absorption gratings in Sn₂P₂S₆," *Opt. Lett.* **37**, 4065–4067 (2012).
4. S. Odoulov, A. Shumelyuk, H. Badorreck, S. Nolte, K.-M. Voit and M. Imlau, "Interference and holography with femtosecond laser pulses of different colours," *Nat. Commun.* 6:5866 doi: 10.1038/ncomms6866 (2015).
5. H. Crespo, J. T. Mendonca, and A. Dos Santos, "Cascaded highly nondegenerate four-wave-mixing phenomenon in transparent isotropic condensed media," *Opt. Lett.* **25**, 829–831 (2000).
6. J. L. Silva, R. Weigand, and H. M. Crespo, "Octave spanning spectra and pulse synthesis by nondegenerate cascaded four-wave mixing," *Opt. Lett.* **34**, 2489–2491 (2009).
7. Jinping He, Jun Liu, and Takayoshi Kobayashi, "Tunable multicolored femtosecond pulse generation using Cascaded Four-Wave Mixing in bulk materials," *Appl. Sci.* **4**, 444–467 (2014).
8. S. Cabuk and A. Mamedov, "A study of the LiNbO₃ and LiTaO₃ absorption edge," *Tr. J. of Physics* **22**, 41–45 (1986).
9. M. Sheik-Bahae, D. J. Hagan, and E. W. Van Stryland, "Dispersion and band-gap scaling of the electronic Kerr effect in solids associated with two-Photon Absorption," *Phys Rev. Lett.* **65**, 97–99 (1990).
10. H. Badorreck, S. Nolte, F. Freytag, P. Bäune, V. Dieckmann, and M. Imlau, "Scanning nonlinear absorption in lithium niobate over the time regime of small polaron formation," *Opt. Mat. Express* **5**, 2729–2741 (2015).
11. M. Imlau, V. Dieckmann, H. Badorreck, and A. Shumelyuk, "Tin hypophosphite: Nonlinear response in the sub-100 fs time domain," *Opt. Mater. Express* **1**, 953–951 (2011).
12. M. Imlau, H. Brüning, B. Schoke, R.-S. Hardt, D. Conradi, and C. Merschjann, "Hologram recording via spatial density modulation of Nb_{Li}^{4+/5+} antisites in lithium niobate," *Opt. Express* **19**, 15322–15328 (2011).
13. C. M. Cirloganu, L. A. Padilha, D. A. Fishman, S. Webster, D. J. Hagan, and E. W. Van Stryland, "Extremely nondegenerate two-photon absorption in direct-gap semiconductors," *Opt. Express* **19**, 22951–22960 (2011).
14. A. Fishman, C. M. Cirloganu, S. Webster, L. A. Padilha, M. Monroe, D. J. Hagan, and E. W. Van Stryland, "Sensitive mid-infrared detection in wide-gap semiconductors using extreme nondegenerate two-photon absorption," *Nat. Photonics* **5**, 561–565 (2011).

15. M. Imlau, H. Badorreck, and C. Merschjann, "Optical nonlinearities of small polarons in lithium niobate," *Appl. Phys. Rev.* **2**, 040606 (2015).
16. Pochi Yeh, "Two-Wave Mixing in Nonlinear Media," *IEEE J. Quant. Electron.* **25**, 484–519 (1989).
17. H.J. Eichler, P. Günter, and D. Pohl, *Laser-induced Dynamic Gratings*, Springer Series in Optical Sciences, vol. **50**, Springer Verlag, Berlin, Heidelberg, 1986.
18. R. Brubaker, Q. Wang, D. Nolte, E. Harmon, and M. Melloch, "Steady-state four-wave mixing in photorefractive quantum wells with femtosecond pulses," *J. Opt. Soc. Am. B* **11**, 1038–1044 (1994).
19. R. Trebino, *Frequency-Resolved Optical Gating: The Measurement of Ultrashort Laser Pulses* (Kluwer Academic Publishers, 2000).

1. Introduction

The experimental observation of Doppler-shifted selfdiffraction from a moving dynamic grating recorded in nominally undoped LiNbO₃ by beams with considerably different optical frequencies is described in this paper. The recording of holographic gratings, both permanent [1] and dynamic [2, 3] with ultrashort laser pulses in crystals like LiNbO₃ is not a new phenomenon. In majority of previous works the recording beams featured, however, identical spectra, i.e., the wave mixing was degenerate in frequency. The main difference of our approach is in the use of pulses with large frequency detuning Ω . As distinct from recently published results on permanent hologram recording with femtosecond pulses of different colors [4], a pronounced third-order nonlinearity of LiNbO₃ allows for creating of a grating that moves together with light fringes even if their velocity is comparable to the velocity of light.

A similar self-diffraction has been reported earlier for some glasses and crystals [5–7], where it was treated in terms of nonlinear optics as Cascaded Four Wave Mixing (CFWM) and nonlinear refraction responsible for wave coupling. Surprisingly, this effect was never reported, to our best knowledge, for well studied classical nonlinear crystal LiNbO₃, an important material in nonlinear photonics and widely used in ultrafast optical parametric oscillators/amplifiers. Our first aim is therefore to clarify what can be expected from LiNbO₃ in this respect. Here, pronounced two photon absorption (TPA) is involved in addition to nonlinear refraction. By choosing the recording photons with energy 2.5 eV, i.e., in the vicinity of 0.7 of band gap energy $E_g \approx 3.63$ eV [8] we come close to the wavelength range in which, according to the data of [9] the nonlinear refraction n_2 is expected to be considerably reduced (with the following change of its sign for larger frequencies). As a result, we do not observe the cascades of diffraction orders even in case of nearly ideal estimated phase matching conditions. At most, six additional beams become visible at ultimate intensities of the recording pulses, three with upshifted and three with downshifted frequencies. This can be explained by a mixed, absorption/refraction nonlinear response of LiNbO₃ in the green-blue spectral range, with relatively high contribution of two-photon absorption. Such explanation is confirmed by estimates of the diffraction efficiencies that can be expected with the known data on real and imaginary parts of $\chi^{(3)}$ susceptibility of our LiNbO₃ samples [10], obtained in z -scan measurements.

Our second aim is to show that the reported Raman-Nath selfdiffraction from a moving grating in LiNbO₃ provides a powerful tool of frequency conversion and can be used efficiently for the characterization of the recording pulses themselves (pulse duration, frequency chirp).

2. Experiment and discussion

A standard two-beam geometry of transmission grating recording is shown in Fig. 1. Two unexpanded recording beams with $\simeq 2.5$ mm spots are generated in two OPAs pumped by the same mode locked Ti:Sapphire laser; they consist of trains of $\simeq 120$ fs pulses with 1 kHz (or 1 Hz) repetition rate, the single pulse energy being in the range from 40 to 80 μ J. The major part of experimental results presented below are obtained with a fixed wavelength of one of the two pulses $\lambda_1 = 489$ nm (frequency $\omega_1 = 3.85 \times 10^{15}$ rad/s) and tunable wavelength of the other

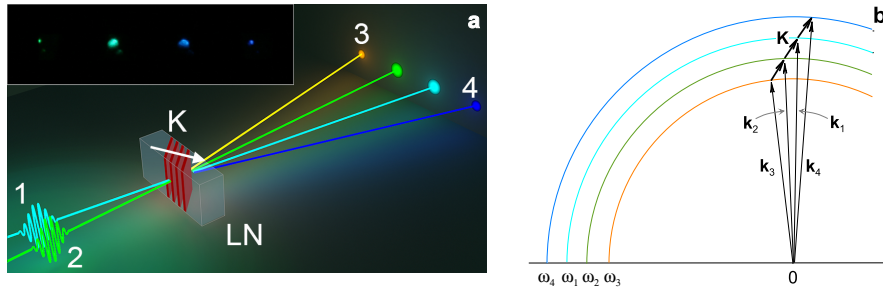


Fig. 1. (a) Experimental geometry: the incident beams 1 and 2 create a moving grating in the LiNbO₃ sample (LN), two diffracted beams 3 and 4 appear at the output in addition to transmitted beams 1 and 2. These beams form four colored spots in the far-field pattern shown in the upper left inset to this picture. (b) Schematic presentation of the wavevector diagram. The fragments of circles show the *xy*-crosssections of Ewald surfaces for the uniaxial crystal LiNbO₃, with radii equal to $k_i = \omega_i n_i / c$ for waves of different colors.

pulse. The description of the femtosecond laser system is given in [4, 11].

The plane parallel *y*-cut samples of nominally undoped LiNbO₃ (see for details [12]) have the polar axis *z* normal to the propagation plane of all beams, sample thickness being 200 μm. The electric field vectors of both recording beams are parallel to the crystal *z*-axis. The beams impinge upon the sample symmetrically, making in air $\pm 2^\circ$ with respect to the normal of the input face. Most often the measurements are done with single fs pulses. For long term exposure of the sample in 1 Hz repetition rate operation mode no cumulative effects are observed. This allows for averaging over numerous consecutive pulses what is important in case of weak signals. With the described arrangement we observe quite pronounced self-diffraction into ± 1 diffraction orders (much weaker ± 2 and ± 3 orders can be seen for highest intensities of the recording beams). The far-field pattern (inset to Fig. 1) gives a representative example, with clearly visible diffraction spots; their spectra measured with Ocean Optics USB4000 spectrometer show obvious Doppler shifts.

The observed phenomenon can be interpreted as follows. Two waves with wavevectors $\mathbf{k}_1, \mathbf{k}_2$ and frequencies ω_1, ω_2 create a periodic dynamic fringe pattern with vector

$$\mathbf{K} = \mathbf{k}_1 - \mathbf{k}_2, \quad (1)$$

which is moving with velocity $v = \Omega / K$ (see, e.g., [4]). Here Ω is the frequency difference $\Omega = \omega_1 - \omega_2$ and K is the spatial frequency $K = |\mathbf{K}|$. In a medium with third order nonlinearity $\chi^3(\omega_1, \omega_1, \omega_2, -\omega_2) \neq 0$, moving fringes lead to the appearance of a moving grating of refractive index or two-photon absorption, or both. This grating can be revealed by the emerging additional waves with wavevectors $\mathbf{k}_3, \mathbf{k}_4$, which meet the phase matching conditions that are equivalent to the conditions of diffraction from a grating with grating vector \mathbf{K} (Eq. (1)):

$$\mathbf{k}_3 = \mathbf{k}_2 - \mathbf{K}, \quad \mathbf{k}_4 = \mathbf{k}_1 + \mathbf{K}, \quad (2)$$

what is shown in the wavevector diagram of Fig. 1(b). It should be underlined that both, the nonlinear index change and nonlinear absorption result from processes which are nondegenerate in frequency. They can, however, be comparably strong as degenerate process. It has been demonstrated convincingly in studies of extremely nondegenerate two-photon absorption in semiconductor crystals [13, 14].

As distinct from diffraction from a static grating, the diffraction from the moving grating

brings also changes in frequencies of diffracted waves,

$$\omega_3 = \omega_2 - \Omega, \quad \omega_4 = \omega_1 + \Omega, \quad (3)$$

what can be regarded as a consequence of the Doppler shift because of grating motion.

Figure 2(a) represents the experimentally measured frequencies of the twodiffracted waves as functions of frequency variation ω_2 for the fixed frequency $\omega_1 = 3.85 \times 10^{15}$ rad/s. Within the experimental error bars these dependences are linear and the measured data are close to straight lines, as plotted using Eq. (3). The dotted lines show a fixed frequency ω_1 of the recording beam 1, and adjustable frequency ω_2 of the recording beam 2.

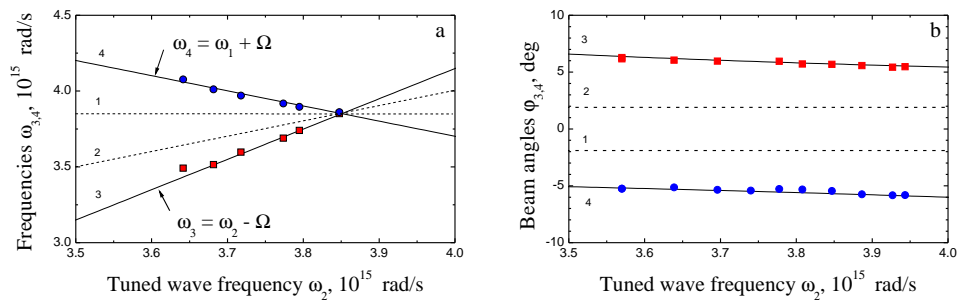


Fig. 2. Frequencies (a) and propagation angles (b) of four beams behind the sample versus frequency detuning of beam 2. Vertically polarized light beams impinge upon the 200 μm -thick γ -cut LiNbO₃ plate in a plane parallel to the polar axis.

The propagation angles for the diffracted beams 3 and 4 can be found from Eq. (2). The calculated frequency detuning dependence of these angles are shown in Fig. 2(b) together with the experimental data. Once more, a satisfactory agreement of measured and calculated values can be stated. The dashed lines show fixed angles of the recording beams propagation.

For monochromatic cw waves that record a 3D grating the higher orders of diffraction are usually not phase matched and would not appear. For the recording with 120 fs pulses the restrictions imposed by phase matching are less rigid. Because of the relatively small effective thickness d the angular selectivity of the grating is rather poor and the tolerance $|\Delta\mathbf{K}| = 2\pi/d$ in meeting phase matching conditions of Eq. (2) is high. On the other hand, for transmission gratings with small spatial frequency (small angles between the recording beams) the spectral selectivity $\Delta\omega/\omega$ is quite soft, too, and covers transform limited temporal spectra of the recording pulses.

With the crystal dispersion taken into account, the calculations (see, e.g., Eq. (1) in [5]) show that nearly exact phase matching can be achieved for four consecutive diffraction orders with increasing temporal frequencies if the full crossing angle between the recording waves is reduced to 1° . This should result in the development of Cascaded FWM which was not observed, however, neither for 1° nor for other crossing angles. We believe it is a consequence of the large contribution of two-photon absorption to the recorded dynamic grating responsible for self-diffraction. A TPA grating with moderate contrast can produce by definition only ± 1 and ± 2 diffraction orders. On the other hand, the presence of TPA inhibits the grating which is due to the optical Kerr effect because it decreases the light intensity within the LiNbO₃ sample.

By using z -scan technique the nonlinear refraction constant n_2 and TPA coefficient β in samples cut from the same LiNbO₃ crystal have been estimated [11]. The measured values are $n_2 \approx 5 \times 10^{-20}$ m²/W and $\beta \approx 5.8$ mm/GW. The rough estimates of additive contributions to overall diffraction efficiency $\eta_{Kerr} \approx (\pi n_2 I_0 d / \lambda)^2$ and $\eta_{TPA} \approx (\beta I_0 d / 2)^2$ show that the contribution from the optical Kerr effect is much smaller than that from the nonlinear absorption

$\eta_{Kerr}/\eta_{TPA} \approx 0.01$. We want to note, that possible effects of free carriers and/or small polarons are not considered for the value of n_2 [15], which however does not change the presence of a mixed grating here.

We experimentally estimate also the conversion efficiency η of wave 2 into wave 3 (and 1 into 4). The values fall below 10^{-2} but they remain practically independent of the recording waves detuning within the range of $\Omega \approx 2 \cdot 10^{14}$ rad/s. It is known that any finite relaxation time of the nonlinear grating results in a diffracted intensity spectrum of Lorentzian type $\eta \propto [1/(1 + \Omega^2 \tau^2)]^2$ (see, e.g., [16]). Thus, a hypothetic inherent characteristic lifetime of the two-photon absorption grating at least much smaller than the reciprocal detuning range $1/\Omega$, i.e., $\tau_{TPA} \ll 5$ fs can be theoretically estimated.

3. Potential for pulse characterization

The dynamic gratings recording can be useful for the characterization of the recording pulses [17–19]. The four-wave mixing in photorefractive crystal has been successfully used to build a correlator that allows for estimating the femtosecond pulse duration [18]. We show that dynamic gratings in LiNbO₃ can be used for such measurements; they can provide in addition an information about the frequency chirp within the pulse, in a similar way as it is done in Rick Trebino’ FROG technique [19].

To perform such measurements the response of self-diffraction to a deliberately introduced time delay $\Delta t = t_1^0 - t_2^0$ between the recording pulses is studied (subscripts ’0’ mark the pulse maxima). The time delay is controlled with an optical delay line in the recording beam 1 with larger frequency. Thus taking pulse 2 as a reference with $t_2^0 = 0$ we have positive Δt for delayed pulse 1. Figure 3 shows time delay dependences of diffracted orders intensities and frequencies.

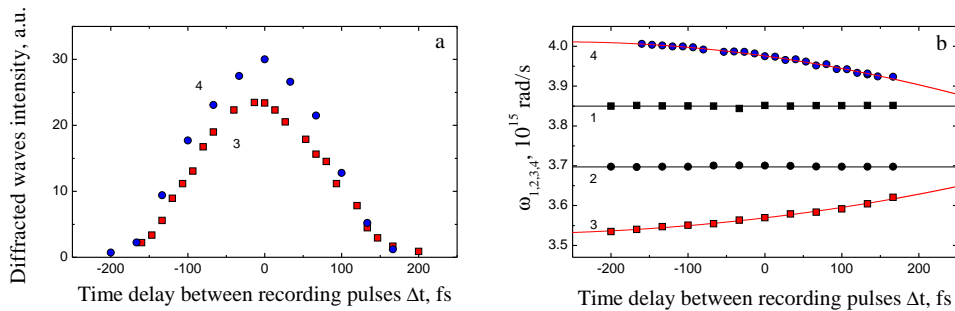


Fig. 3. Intensities (a) and spectral positions (b) of the diffracted pulses 3, 4 versus time delay between the recording pulses with the wavelengths $\lambda_1 = 489$ nm and $\lambda_2 = 509$ nm.

The characteristic bell shaped dependence of the intensity (Fig. 3(a)) reveals information about the pulse duration (see, e.g., [17–19]). For Gaussian shape of the recording pulses the FWHM of the diffraction efficiency should be $\sqrt{2}$ larger than the FWHM of the pulse itself [18].

The dependence of the diffracted beams frequencies on the mutual pulse delay proves that the instantaneous frequencies within the recording pulses change in time, i.e., pulses are chirped. Let’s consider that the central frequencies of the diffracted pulses 3,4 in Fig. 3(b) can be described by a Taylor series expansion up to second order:

$$\omega_{3,4}(\Delta t) = \omega_{3,4}(0) + \frac{d\omega_{3,4}}{d(\Delta t)} \cdot \Delta t + \frac{d^2\omega_{3,4}}{d(\Delta t)^2} \cdot (\Delta t)^2 + \dots \quad (4)$$

Here $d\omega/d(\Delta t)$ and $d^2\omega_{3,4}/d(\Delta t)^2$ are the linear and the second order pulse chirp components.

We assume, in first approximation, only a dominating linear chirp for the frequencies $\omega_1(t - \Delta t)$ and $\omega_2(t)$, the chirp being identical for both pulses because of their common origin. Then the frequency difference $\omega_1 - \omega_2$ is independent of the running time t for any arbitrary time delay Δt and remains constant during pulse propagation inside the sample. The higher orders of diffraction 4 and 3 will be upshifted and downshifted in frequency just for $\omega_1 - \omega_2$ which is a function of pulse delay Δt . This allows to deduce the relationship between the frequency difference of higher diffraction orders $\Omega_{4-3} = \omega_4 - \omega_3$ and the chirp parameter $d\omega/dt$ of the incident pulses 1,2

$$\frac{d\omega}{dt} = -\frac{1}{3} \frac{d\Omega_{4-3}}{d(\Delta t)} = -\frac{1}{3} \left(\frac{d\omega_4}{d(\Delta t)} - \frac{d\omega_3}{d(\Delta t)} \right). \quad (5)$$

The comparison of experimental data of Fig. 3(b) with the above considerations brings us to the conclusion that we are dealing with positively chirped pulses, $d\omega/dt > 0$. By extracting a linear term of a polynomial fit in Fig. 3(b) the absolute value of the linear chirp is estimated to be $d\omega/dt \simeq (0.16 \pm 0.02) \cdot 10^{27}$ rad/s². Taking the second order term in Eq. (4) into account, information on higher order chirp coefficients can be obtained, too. The chirp measured in this experiment is the inherent feature of the recording pulses themselves, it could be increased or partially compensated for by using two-grating pulse compressor.

In the limiting case of frequency degenerate recording beams, $\omega_1 = \omega_2$, the described technique is identical to the self-diffraction based implementation of FROG [19]. Working with recording pulses that are non-degenerate in frequency ensures an obvious advantage: the signal-to-noise ratio of the diffracted pulses can be largely improved by profiting from spectral filtering in addition to spatial (angular) filtering typical to all self-diffraction techniques. A single-shot variation of this technique is possible if traditional spectrometers with an input slit are used instead of the Ocean Optics spectrometer with small circular input aperture.

4. Summary and conclusions

The superposition of two pulses of different color in LiNbO₃ sample results in the appearance of Doppler-shifted diffracted beams, even in the spectral range of pronounced two-photon absorption. As a remarkable feature, the diffracted beams, upshifted and downshifted in frequency, are observed up to ± 3 order, however with no cascading to the higher diffraction orders. Using the language of transient gratings the phenomenon can be explained by the recording of a mixed nonlinear absorption and nonlinear refraction grating, that moves at a velocity close to the velocity of light. It becomes possible to explain the appearance of symmetric diffraction orders in +/- directions, to evaluate the diffraction efficiency and estimate, for the first time for LiNbO₃ the upper limit of the grating relaxation time to be less than 5 fs. Straightforwardly, the findings are applied for simple measurements of the chirp of incident recording beam.

Our results highlight the importance of two-photon absorption nonlinearity and explain the inhibition, in the used frequency range, of Cascaded FWM. It is not excluded, that the latter will emerge in the frequency range with negligible two-photon absorption, in the near infrared.

The described phenomenon is treated in terms of recording and self-diffraction from the dynamic grating which is moving with high velocity and brings therefore Doppler shift for diffracted waves. The purpose is not simply to introduce other language to the field; we are convinced that being extended to strongly nondegenerate interactions it will provide new important results in future, especially related to nonlinear coupling of beams with different colors.

Acknowledgments

Financial support of Deutsche Forschungsgemeinschaft, DFG (IM37/5-2, INST 190/137-1 FUGG, INST 190/165-1 FUGG) and Alexander von Humboldt Stiftung (S. Odoulov Research Award) is gratefully acknowledged. We thank Prof. Dr. Eckhard Krätzig and Dr. Javid Shirdel for fruitful discussions.

A.4 **Dynamic-grating-assisted energy transfer between ultrashort laser pulses in lithium niobate**

Dynamic-grating-assisted energy transfer between ultrashort laser pulses in lithium niobate

STEFAN NOLTE,¹ BJOERN BOURDON,¹ FELIX FREYTAG,¹ MIRCO IMLAU,^{1,*} ALEXANDR SHUMELYUK,² AND SERGUEY ODOULOV²

¹*Department of Physics, Osnabrueck University, Barbarastrasse 7, D-49076 Osnabrueck, Germany*

²*Institute of Physics, National Academy of Sciences, 03650 Kyiv, Ukraine*

*mimlau@uni-osnabrueck.de

Abstract: Energy redistribution between two subpicosecond laser pulses of 2.5 eV photon energy is observed and studied in congruent, nominally undoped LiNbO₃, aiming to reveal the underlying coupling mechanisms. The dependences of pulse amplification on intensity, frequency detuning and pulse duration point to two different contributions of coupling, both based on self-diffraction from a recorded dynamic grating. The first one is caused by a difference in pulse intensities (transient energy transfer) while the second one originates from a difference in pulse frequencies. The latter appears when chirped pulses are mutually delayed in time. A quite high coupling efficiency has been observed in a 280 μm thin crystal: one order of magnitude energy amplification of a weak pulse and nearly 10% net energy enhancement of one pulse for the case of equal input intensities.

© 2018 Optical Society of America under the terms of the [OSA Open Access Publishing Agreement](#)

1. Introduction

The intensity coupling of two light waves that propagate in a nonlinear medium (two-beam coupling) is one of the basic phenomena of dynamic holography [1]. This type of coupling has attracted the interest of researchers since the discovery in 1980's of unidirectional intensity transfer between two waves that are recording a shifted phase grating in a nonlinear optical crystal (see, e.g., [2, 3]). A new type of coherent light wave amplification became possible, various dynamic-grating-based coherent optical oscillators were designed and used as self-starting phase conjugate mirrors [4].

In the early stage of the dynamic holography, emphasis was put on the intensity coupling of continuous waves (cw), both in theory and in experiment. Quite quickly the developed approaches were extended for the description of the interaction of light pulses. The term "two-beam coupling" was still used to define the interaction of pulses (see, e.g., [5–7]), but it became often replaced by "pulse energy transfer" [8–12] or "energy exchange" [13]. The researchers dealing with pump-probe techniques were facing the problem of so called "coherent peaks" [14, 15], which is a consequence of pump and probe pulse coupling via a dynamic grating, too [16]. It should be mentioned that the fundamental phenomenon of gain in stimulated Rayleigh-wing scattering had been treated well before the appearance of femtosecond lasers [17–21], but never in terms of diffraction from a grating. A comprehensive analysis of pulse coupling is given in the review article [22] and textbooks [23, 24]. More than a hundred original publications that consider different aspects of grating-assisted interaction of pulses have been published.

The self-diffraction of the recording pulses themselves, or diffraction of an auxiliary probe pulse from the developing instantaneous or inertial grating, are still studied nowadays [25]. It has been used for the characterization of the pulses themselves [26, 27], plasma filament control in air [6] and nonlinear liquids [11], nonlinear spectroscopy of the materials themselves [7, 13], frequency conversion [28, 29], etc. The subpicosecond pulses even allowed, quite counter-intuitively, for grating recording with light being strongly nondegenerate in frequency [30]. Both, dynamic

and permanent gratings were recorded. The recording of static holograms with image bearing pulses proved to be possible with subpicosecond pulses of different color, with further image reconstruction by a cw laser beam [30].

Commonly, the description of grating-assisted pulse interaction is based on the solution of coupled wave equations for a spatial variation of slowly varying complex amplitudes (see, e.g., [2, 3, 22–24]). While these equations are nearly always the same, the material equations, which are necessary to calculate the temporal dynamics of interaction, depend on the particular nonlinear medium and the particular type of nonlinearity involved. The present work is an experimental study in which the measured dependences are compared with predictions of already existing theories that describe particular coupling processes. We conduct this study to estimate the strength of the coupling of subpicosecond pulses in LiNbO₃ and to reveal the types of underlying wave mixing process(es) that is (are) responsible for an energy redistribution between the interacting pulses. Lithium niobate was the first crystal in which a photorefractive nonlinearity and grating-assisted intensity redistribution of the recording waves have been discovered [4, 31]. Apart from the instantaneous high-frequency Kerr nonlinearity [32] and two-photon absorption (TPA) nonlinearity [33], several inertial nonlinear responses have been revealed, too. They include photoexcitation of free carriers [34, 35], and the formation of various kinds of polarons [36]. The identification of the physical process of nonlinearity that is responsible for the investigated pulse coupling will be, however, the topic of a separate study.

The structure of the present paper is as follows. After this *Introduction*, the section *Experimental technique* presents the description of chirped femtosecond laser pulses, the nonlinear optical crystal itself, and the experimental setup. The third section, the *Experimental results*, consists of four parts, devoted to particular sets of measurements. In subsection 3.1 a small signal amplification is studied, with a weak probe pulse which interacts with a stronger pump pulse, both pulses being perfectly matched in time. Subsection 3.2, on the opposite, focuses on the interaction of pulses of equal energies that become detuned in frequencies being temporally mismatched. In subsection 3.3 the effect of the pulse duration is analyzed for the interaction of identical pulses. Finally, in the last subsection 3.4, a possible influence of extended temporal spectra of ultrashort pulses on their energy coupling is analyzed. In the *Discussion* section it is shown that the major contribution to energy transfer between subpicosecond pulses in congruent, nominally undoped LiNbO₃ is due to two different coupling processes: (i) quasi steady-state coupling of waves of equal intensity with mutually shifted frequencies and (ii) transient, non-steady-state coupling of waves of different intensities but with identical spectra. The first process was already proven to be responsible for the interaction of frequency-chirped pulses in gases, plasma and liquids (see, e.g., [6, 7, 11, 13]). Our study shows that it results in a quite strong pulse interaction in a solid-state material as well. The second process has never been considered, to the best of our knowledge, for the interaction of short pulses in spite of the fact that it was revealed long ago for interactions in photorefractive crystals [37] and media with a thermal nonlinearity [38, 39].

2. Experimental technique

All experiments in this paper are performed with a classical interaction geometry of two-beam coupling of co-propagating light beams which is also standard for pump-probe techniques. Figure 1 shows schematically the experimental setup used for our studies. Two ultrashort light pulses with equal central wavelengths of $\lambda = 488$ nm (or $\lambda = 590$ nm) impinge upon a LiNbO₃ sample with a full crossing angle in air of $2\theta < 5^\circ$. A relatively small angle can be set by the use of a single focusing lens (L) for both pulses to ensure a good spatial overlap of the femtosecond pulses. An optical delay line (DL) is installed in one of the two beams to adjust a temporal mismatch Δt between both pulses of up to several picoseconds.

The main measured characteristic in this paper is the normalized transmission $T_i = W_i/W_i^0$ for each of the two interacting pulses (subscripts pu and pr for pump and probe pulses, respectively).

Here, W_i denotes the transmitted pulse energy of one pulse in presence of the other pulse, while W_i^0 is the energy of the unaffected transmitted pulse, with no other pulse in the sample. The transmission T_i is measured as a function of different experimental parameters: total intensity of the two pulses I , pulse intensity ratio $R = I_{\text{pu}}/I_{\text{pr}}$, temporal delay between the two pulses Δt , and FWHM pulse duration τ_c . These data make it possible to evaluate a weak-probe gain G_{wp} (when the probe pulse propagates in presence of a stronger pump pulse) and a strong-probe gain G_{sp} (in case of energy transfer between pulses with equal energies), as it is explained in the next sections. The energies of the incident and transmitted pulses are measured with a laser power meter (*Coherent LabMax*) as well as biased silicon detectors (*Thorlabs DET10A*).

The y -cut sample of congruent, nominally undoped lithium niobate with plane parallel input/output faces has a thickness of $d \approx 280 \mu\text{m}$. At the particular wavelength of $\lambda = 488 \text{ nm}$ the pronounced two-photon absorption and small polaron absorption have been reported [36, 40]; the coefficients of two-photon absorption, $\beta_{\text{TPA}} \approx 5.6 \text{ mm/GW}$, and optical Kerr effect, $n_2 \approx 5 \cdot 10^{-20} \text{ m}^2/\text{W}$, are known from z -scan experiments [40].

The femtosecond pulses are generated by a mode-locked Ti:Sapphire laser (*Coherent, Libra*) that feeds two independently tunable Optical Parametric Amplifiers (OPA, *Coherent, OPerA-Solo*) [29, 30]. Pulses with central wavelengths of $\lambda = 488 \text{ nm}$ and spectral bandwidths of $\Delta\lambda = 4.7 \text{ nm}$ from only one OPA are used for frequency non-degenerated experiments, unless otherwise stated. The central wavelength and spectral bandwidth of the interacting pulses are monitored with a fiber spectrometer (*Ocean Optics, USB4000*).

To evaluate the peak intensity $I_{\text{pu,pr}}$ of a pulse with an energy W , its spatial and temporal profiles need to be known. Measurements of the transverse intensity distribution at the sample input face revealed a Gaussian-like shape of both beams with nearly identical radii of $r \approx 55 \mu\text{m}$ at the e^{-2} level of the peak intensity. The durations τ_c of the incident pulses are estimated with a commercial autocorrelator (*APE, pulseCheck PD15*) assuming a Gaussian temporal intensity profile with peak value:

$$I = \sqrt{\frac{16 \ln(2)}{\pi^3}} \frac{W}{r^2 \tau_c}. \quad (1)$$

The pulse energies W (and therefore the peak intensities I) of the two pulses were controlled by using variable neutral density filters (VFs) so that different ratios $R = I_{\text{pu}}/I_{\text{pr}}$ could be adjusted. The pulse duration could be changed within a range of $\tau_c = (80 - 830) \text{ fs}$ using a pulse

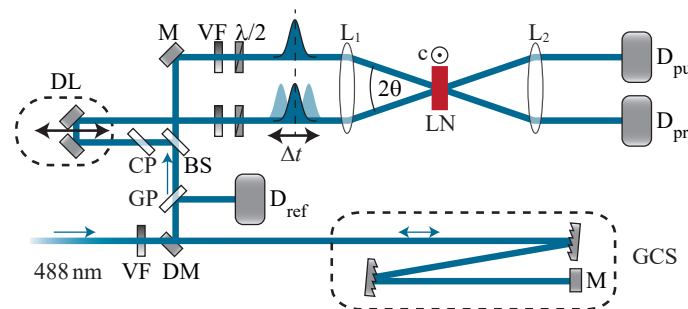


Fig. 1. Schematic of the experimental setup: variable neutral density filter (VF), double grating compressor/stretcher (GCS), glass plate (GP), 50/50 beamsplitter (BS), compensator plate (CP), optical delay line (DL), mirror (M), D-shaped mirror (DM), $\lambda/2$ -waveplate, lenses $f = 500 \text{ mm}$ ($L_{1,2}$), full crossing angle in air 2θ , lithium niobate sample (LN) with the polar c -axis normal to the plane of drawing, and silicon detectors (D_{ref} , D_{pu} and D_{pr}).

compressor/stretcher (GCS). A folded double-grating setup allows for introducing a negative pulse chirp in our experiment. Otherwise, a double prism setup could be used to impose a positive pulse chirp, profiting from the material dispersion (N-SF11 glass, for example).

The spectral bandwidth $\Delta\omega = 3.7 \cdot 10^{13}$ rad/s of the Gaussian shaped pulses defines the theoretically smallest, Fourier-transform-limited pulse duration of $\tau_0 = 75$ fs. For deliberately stretched pulses the frequency chirp coefficient $\dot{\omega}$ depends on the pulse duration τ_c (cf. [41]):

$$\dot{\omega} = (\Delta\omega/\tau_c)\sqrt{1 - (\tau_0/\tau_c)^2}. \quad (2)$$

The total peak intensity $I = I_{\text{pu}} + I_{\text{pr}}$ never exceeded 640 GW/cm^2 to avoid laser-induced damage of the sample. The kHz repetition rate of the pulse train was reduced by an optical chopper to 12.5 Hz. All coupling processes under investigation emerge in a single pulse shot and no cumulative effects have been observed for repetitive-rate operation. This enabled us to average data of 200 consecutive pulses to reduce the impact of pulse-to-pulse fluctuations and to improve accuracy.

Both interacting pulses enter the sample in a plane perpendicular to the axis of spontaneous polarization \mathbf{c} . The light polarization could be adjusted to each beam independently by two $\lambda/2$ phase retarders, with care taken to avoid possible changes in the temporal delay Δt between the pulses. Usually, the polarization unit vectors are set parallel to the polar axis, $\mathbf{e}_1 \parallel \mathbf{e}_2 \parallel \mathbf{c}$, unless stated otherwise. This particular configuration excludes a possible contribution to pulse coupling from the space charge field grating because the relevant Pockels tensor components of LiNbO_3 are vanishing (see, e.g., [42]).

3. Experimental results

3.1. Coupling of pulses with different energies

We start from the description of experiments with pulses of significantly different energies that allow to characterize a weak-probe gain G_{wp} . Figure 2 gives a typical example of the probe pulse transmission in presence of a pump pulse with the same polarization T_{\parallel} as a function of the temporal delay Δt between both pulses (black data points). The pulse duration of each pulse $\tau_c \approx 80$ fs is close to the Fourier limit τ_0 . The transmission $T_{\parallel}(\Delta t)$ features a considerable increase in the vicinity of $\Delta t = 0$ with a maximum value of $T \approx 2.3$. An asymmetry of the signal

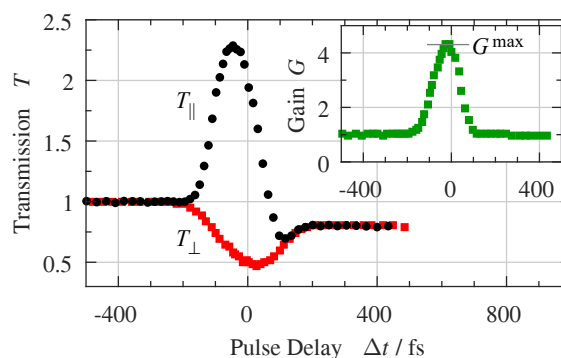


Fig. 2. Pulse delay dependence of the normalized probe pulse transmission with parallel (T_{\parallel} , black dots) and orthogonal polarization (T_{\perp} , red squares). The inset shows the gain G (green squares) evaluated from Eq. (3). The total peak intensity of the two pulses is $I \approx 635 \text{ GW/cm}^2$ with a peak intensity ratio of $R \approx 100$, pulses duration of $\tau_c = (80 \pm 5)$ fs and beam radii of $r = (55 \pm 5) \mu\text{m}$.

$T_{\parallel}(\Delta t)$ is obvious, with the transmission saturated at $T_{\parallel}^{\text{sat}} \approx 0.8$ for large positive Δt . This value of $T_{\parallel}^{\text{sat}}$ below unity can be attributed to the light-induced absorption caused by optically generated small, strong-coupling polarons [33, 36].

It is noteworthy that the appearance of additional oblique beams behind the sample has been detected within the Δt interval where probe amplification occurs ($T \geq 1$). Their angular position suggests that these are higher orders of diffraction from a grating recorded with the two incident pulses. The largest overall energy of these higher diffraction orders could approach 10% of the total transmitted energy.

The transmission of the probe pulse changes dramatically if the polarization of the pump pulse is turned to 90° , as depicted by the red data points. Here, the transmission T_{\perp} shows a dip in the vicinity of $\Delta t = 0$ that can be attributed to the effect of two-photon absorption [33]. In agreement with this assumption, we found that the temporal width of this dip depends on the duration τ_c of the incident pulses, while possible broadening of the dip caused by the group velocity mismatch can be neglected for the used thin birefringent crystal. The saturation is again reached at $T_{\perp}^{\text{sat}} \approx 0.8$.

From the comparison of both curves in Fig. 2 one can deduce that in presence of the pump pulse with the same polarization the probe pulse experiences simultaneously attenuation and gain. The attenuation is caused by two-photon absorption, polaron absorption, and the appearance of higher diffraction orders. It is the diffraction of the strong pump pulse into the weak probe which is responsible for amplification.

A simplified approach can be used to account for all these processes. It represents the normalized transmission of the probe pulse $T(\Delta t)$ as a product of two factors $A(\Delta t)$ and $G(\Delta t)$ that describe the fractional changes of transmission which are due to losses and gain, respectively. As all losses can only decrease the transmission, A should be smaller than unity but should remain always positive, $0 \leq A \leq 1$. The gain factor G is always larger than unity but it is limited by the intensity ratio R of the interacting pulses $1 \leq G \leq R + 1$, as energy can be transferred to the probe only from the pump pulse.

For further analysis, the energy gain is introduced as an experimentally measurable quantity

$$G(\Delta t) = \frac{T_{\parallel}(\Delta t)}{T_{\perp}(\Delta t)} = \frac{A(\Delta t)G(\Delta t)}{A(\Delta t)}, \quad (3)$$

i.e., the ratio of the transmission with identically polarized T_{\parallel} (gain and losses) and cross-polarized T_{\perp} (losses only) pump and probe pulses. According to Eq. (3), the ratio $T_{\parallel}(\Delta t) / T_{\perp}(\Delta t)$ is not affected by nonlinear absorption $A(\Delta t)$. Such a treatment is justified under the assumption that both, the instantaneous losses for TPA as well as losses for residual polaron absorption, exhibit a negligible polarization dependence [36, 43]. A small difference in $A(\Delta t)$ for ordinary and extraordinary pump waves can therefore be neglected. The pulse delay dependence of the gain $G(\Delta t)$ extracted in such a way is shown in the inset to Fig. 2; the value of $G^{\text{max}} = (4.4 \pm 0.2)$ is reached in the vicinity of $\Delta t = 0$.

The gain intensity dependence as well as its intensity ratio dependence are important characteristics for the identification of a particular coupling process. Figure 3 shows the gain G^{max} as a function of peak intensity for the shortest pulses used ($\tau_c \approx 80$ fs) and two different ratios of the peak intensities R . A nonlinear increase of the gain is observed for intensities I below 300 GW/cm^2 for both values of R . Within the quite large error bars the data can be fitted by a $I^{2.5}$ dependence.

The gray area in Fig. 3 represents the possible range of gain variation only for the black squares ($R \approx 1000$). Both dependences, for $R \approx 1000$ and $R \approx 100$, show an obvious tendency to saturation of the gain at high intensities, with saturation level decreasing for $R \rightarrow 1$.

Figure 4 shows the gain $G(\Delta t = 0)$ as a function of the input pump/probe peak intensity ratio R while keeping the total peak intensity I constant. The logarithmic plot used here underlines

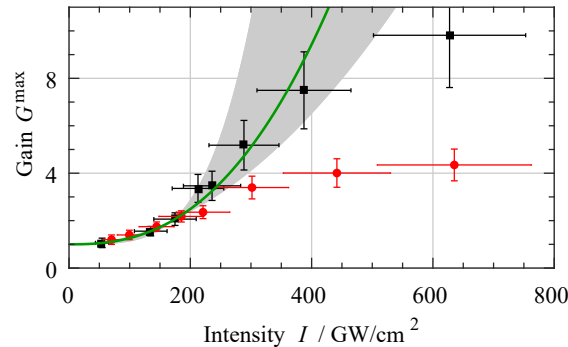


Fig. 3. Gain G^{\max} versus total pulse peak intensity I . Black and red symbols show the data for the intensity ratios $R \approx 1000$ and $R \approx 100$, respectively, for pulses with durations $\tau_c = (80 \pm 5)$ fs and beam radii $r = (55 \pm 5)$ μm . For intensities below 300 GW/cm^2 the measured data can be fitted with $G^{\max-1} \propto I^m$. For $R = 1000$ such a fit gives $m = 2.5$ (green line); the gray shaded area is limited by functions with the exponents $2 < m < 4$.

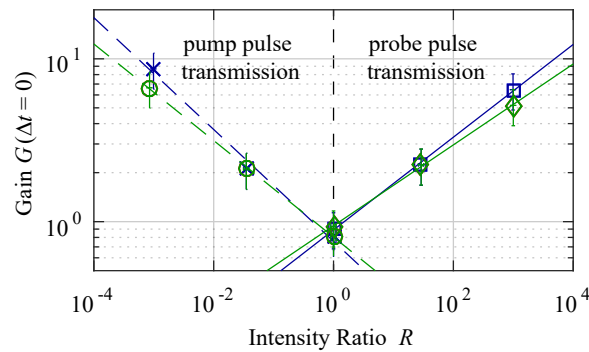


Fig. 4. Gain $G(\Delta t = 0)$ versus peak intensity ratio R in a log-log plot. Right and left branches show the experimentally measured gain for weak probe and weak pump pulses, respectively. The total peak intensity of two pulses is $I \approx 630 \text{ GW/cm}^2$ (blue) and $I \approx 380 \text{ GW/cm}^2$ (green) with pulses duration $\tau_c = (80 \pm 5)$ fs and beam radii $r = (55 \pm 5)$ μm . Solid and dashed lines are plotted as a guide to the eye.

that the energy flows always from the strong to the weak pulse. For $R \leq 1$ the peak intensity of the probe pulse becomes larger than that of the pump, and the measured gain G is related here to the normalized pump pulse transmission. It is obvious that the gain $G(\Delta t = 0)$ increases with growing R and vanishes for equal peak intensities $R = 1$ for a weak probe pulse. Similarly, for $R \leq 1$ the gain of a weak pump pulse increases with R^{-1} . The branches for $R \leq 1$ and $R \geq 1$ are basically symmetric, with approximately the same absolute exponent for the intensity ratio dependence $G \propto R^{\pm 0.3}$. The fact that the measured values of gain $G(\Delta t = 0)$ at $R = 1$ are roughly 10% smaller than unity indicates that additional losses exist besides those already accounted for TPA and polaron absorption. These losses are due to the light going into higher orders of diffraction. They become the most significant for a 1 : 1 intensity ratio of the recording pulses.

The measured dependences of gain [Figs. 3 and 4] are typical for transient beam coupling [37–39] what will be explained in details in section 4, Discussion.

3.2. Coupling of pulses with equal energies

As it was demonstrated in the previous subsection no energy redistribution occurs between two perfectly synchronized pulses ($\Delta t = 0$) with equal energies [see Fig. 4]. In what follows we show that even with $R = 1$ an energy redistribution becomes possible when a temporal mismatch between two frequency-chirped pulses is introduced. Two pulses with equal energies are chosen in these experiments to avoid any possible energy flow from a strong to a weak pulse.

It is known that the removal of frequency degeneracy of two recording waves may result in a strong intensity coupling, both for interactions of continuous waves [2] and sub-picosecond pulses [13,21,44]. The pulse delay of two otherwise identical pulses with a linear frequency chirp $\dot{\omega}$ [see Eq. (2)] is used in our further experiments to adjust a controllable frequency detuning Ω . Both pulses, still called pump and probe in a formal way, have time-dependent frequencies $\omega_{\text{pr,pu}}(t) = \omega_0 + \dot{\omega}t$. Thus, for any non-zero Δt an instantaneous frequency detuning $\Omega(\Delta t)$ appears that does not depend on time:

$$\Omega(\Delta t) = \omega_{\text{pr,pu}}(t - \Delta t) - \omega_{\text{pu,pr}}(t) = -\dot{\omega} \cdot \Delta t. \quad (4)$$

Figure 5(a) gives a representative example of the pulse delay dependence of the normalized transmission $T_{\text{pr,pu}}(\Delta t)$ for two identical pulses, i.e., with the same peak intensity ($R = 1$), chirp coefficient, polarization, pulse duration, beam radius, central wavelength, spectral width and symmetrical angles of incidence [as shown in Fig. 1]. The labeling of pulses as pump and probe is a matter of convention here because both pulses are indistinguishable. However, the sign of the temporal delay is chosen in such a way that for positive values of Δt , the pump pulse passes the sample prior to the probe pulse.

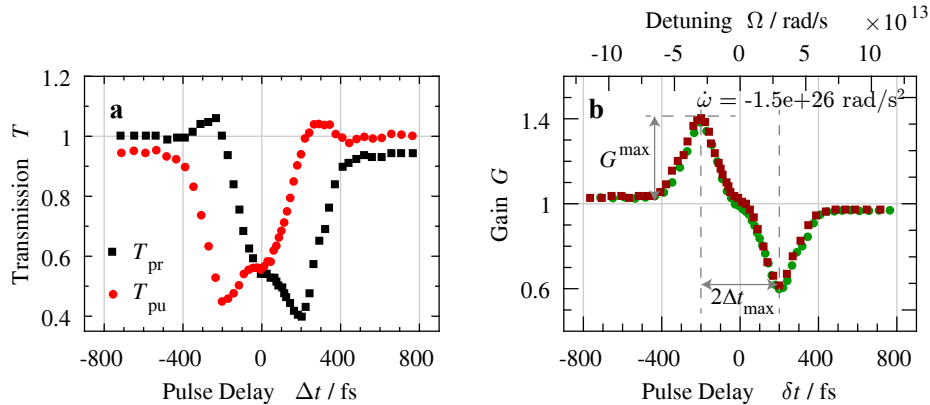


Fig. 5. Pulse delay dependences of (a) normalized transmission $T(\Delta t)$ for pump and probe pulses and (b) gain $G(\delta t)$ evaluated according Eq. (5) (with flipped curve $\delta t = -\Delta t$ for the data T_{pu}). Each pulse has an energy of $W = (5.1 \pm 0.1) \mu\text{J}$, a pulse duration of $\tau_c \approx 235$ fs and a bandwidth of $\Delta\omega = 3.7 \times 10^{13}$ rad/s. The beam radii are $r \approx 160 \mu\text{m}$ and the sum of the peak intensities of both pulses is $I \approx 100 \text{ GW/cm}^2$.

First of all, in Fig. 5(a) a mirror symmetry is obvious for the two curves that define pump and probe transmission. This symmetry could be expected because the advanced pulse becomes the delayed pulse (and vice versa) when the pulse temporal mismatch Δt changes its sign. For this reason the axis of symmetry can be used to find the position of perfect temporal overlap of the pulses $\Delta t = 0$. At this particular position the transmission values are nearly the same for both pulses, thus indicating no energy redistribution. This is in agreement with the data of Fig. 4 for $G(\Delta t = 0)$ at $R = 1$, where only additional losses and no energy redistribution have been detected.

As distinct from the data of Fig. 2, the maximum of the pulse transmission T is reached now at a much longer pulse delay; it approaches 1.1 roughly at $\Delta t \approx \pm 260$ fs. The transmission of the second pulse shows a pronounced dip at the same time, thus indicating that the energy gain of one pulse is caused by a depletion of the other one.

In this new set of measurements with $R = 1$ the transmission is measured for both interacting pulses simultaneously. This allows for estimating the gain G without an additional measurement of the transmission for orthogonally polarized pulses. New expressions for G are derived instead of Eq. (3), still maintaining the same definition of the normalized transmission as a product of loss and gain factors $T(\Delta t) = A(\Delta t)G(\Delta t)$. It is assumed, however, that the pulse delay dependent loss factors are the same for both pulses $A_{\text{pr}}(\Delta t) = A_{\text{pu}}(\Delta t)$. As a consequence, the transmission ratio of both pulses appears to be equal to the ratio of the pulse energy gain $T_{\text{pr}}(\Delta t)/T_{\text{pu}}(\Delta t) = G_{\text{pr}}(\Delta t)/G_{\text{pu}}(\Delta t) = P(\Delta t)$ and it becomes possible to quantify the gain factors as follows:

$$G_{\text{pr}}(\Delta t) = \frac{2P(\Delta t)}{1 + P(\Delta t)}, \quad G_{\text{pu}}(\Delta t) = \frac{2}{1 + P(\Delta t)}. \quad (5)$$

The G values defined by Eq. (5) cannot exceed $G = 2$ for both interacting pulses, what corresponds to a total energy transfer from one pulse to the other. Therefore, the "gain" of the depleted pulse cannot become smaller than $G = 0$; $G = 1$ still indicates no pulse amplification. Because of energy conservation the sum of these two gain parameters should always be constant $G_{\text{pr}}(\Delta t) + G_{\text{pu}}(\Delta t) = 2$.

Figure 5(b) represents the time delay dependence of the gain G replotted from the data of Fig. 5(a) according to Eq. (5). A new variable δt is introduced to pin the gain measured for the delayed pulse always to positive values of δt . Thus, δt coincides with Δt for the black curve of Fig. 5(a) and is inverted in its sign for the red data points $\delta t = -\Delta t$. This change of the pulse delay variable in Fig. 5 does not only underline the similarity of the shown curves, it further allows for adding a second axis for the frequency detuning Ω as estimated from Eq. (4). The data of Fig. 5(b) indicate an energy flow from the delayed to the advanced pulse, i.e., from the pulse with higher frequencies to the pulse with lower frequencies. It should be noted that the coupling direction is insensitive to the LiNbO₃ sample rotation to 180° along the z -axis as well as along the x -axis. The gain extrema are separated by $2\Delta t_{\text{max}} \approx 400$ fs and the maximum gain reaches $G^{\text{max}} \approx 1.4$. This pulse delay, that ensures the strongest coupling, corresponds to a certain fixed frequency detuning of $\Omega_{\text{max}} = 3.0 \times 10^{13}$ rad/s.

The assumption $A_{\text{pr}}(\Delta t) = A_{\text{pu}}(\Delta t)$ that has been formulated when deriving Eq. (5) can be justified as follows: within the area of strong temporal overlap of two pulses, $|\Delta t| \leq 2\tau_c$, the dominant losses are due to two-photon absorption and diffraction into higher orders, whereas the contribution of residual absorption from small polarons is much smaller. The latter can only be seen for large values of $|\Delta t|$ with transmission values slightly below unity. Because of the small magnitude of the polaron absorption in comparison to instantaneous losses, its impact on the gain evaluation should be minor. This estimate is supported by the data of Fig. 5(b), where the deviation of the gain from unity is hardly detectable for large pulse delays $|\delta t|$, and is much smaller than the maximum gain.

In the measurements presented above, the sign of the chirp coefficient is imposed to be negative $\dot{\omega} < 0$, resulting from the negative dispersion introduced by the grating compressor. To verify the sensitivity of the energy transfer direction to the sign of the frequency chirp, the latter was reversed to become positive $\dot{\omega} > 0$ by profiting from the material dispersion of a double prism compressor (N-SF11 dense flint glass).

In Fig. 6 the left and right graphs show the time delay dependences of G for pulses with negative and positive chirp coefficients $\dot{\omega}$, respectively. It is obvious that the flip of the chirp sign results in a change of the energy flow direction, whereas their extrema still occur roughly at same detunings Ω . The difference in gain magnitudes in Fig. 6(a) and Fig. 6(b) might be caused

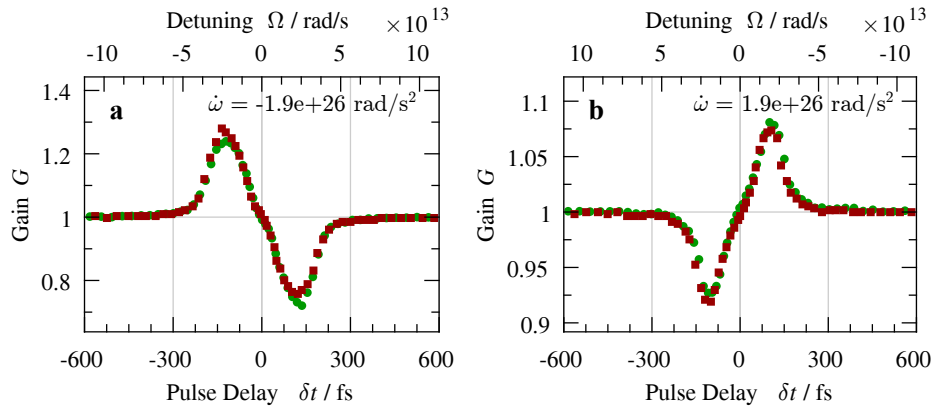


Fig. 6. Pulse delay dependence of gain $G(\delta t)$ for (a) pulses with a negative frequency chirp and energies $W = (2.6 \pm 0.1) \mu\text{J}$ and (b) pulses with a positive frequency chirp and energies $W < 2 \mu\text{J}$. Identical pulses are used, with central wavelengths $\lambda = 590 \text{ nm}$, bandwidths of $\Delta\omega = 4.0 \times 10^{13} \text{ rad/s}$ and durations $\tau_c \approx 200 \text{ fs}$. The pulse frequency detuning Ω estimated according to Eq. (4) is shown as the upper x-axis. Red and green colors mark two interacting pulses.

by different pulse energies. It should be mentioned that these measurements are performed at a higher wavelength ($\lambda = 590 \text{ nm}$) than previous measurements. The two-photon absorption coefficient is smaller for higher wavelength and the residual absorption of photogenerated small polarons is reduced, too. As a consequence, the deviation of the gain from unity in a range of large pulse delays becomes basically undetectable.

The position of gain extrema can be used to determine the optimum frequency detuning for the pulses to ensure the highest energy transfer: $\Omega_{\text{max}} = 2.4 \times 10^{13} \text{ rad/s}$ for Fig. 6(a) and $\Omega_{\text{max}} = 2.0 \times 10^{13} \text{ rad/s}$ for Fig. 6(b). The measured dependences of gain are obviously antisymmetric (odd) functions, i.e., the change of the detuning sign results in the inversion of the energy transfer direction. This leads to the conclusion that in this set of measurements the reason of the pulse energy coupling is the frequency difference of the two pulses.

3.3. Pulse duration dependence

The pulse-delay dependences of gain, similar to that shown in Fig. 5(b), are collected in the next set of experiments for negatively chirped pulses of different durations τ_c . A double grating pulse stretcher is used to control τ_c , sketched in Fig. 1. The measured data are used to plot in Fig. 7(a) the dependence of the largest values of the gain $G^{\text{max}}(\tau_c)$ versus pulse duration (red dots). In the same Fig. 7(a) one can see how the temporal mismatch of the interacting pulses $\Delta t_{\text{max}}(\tau_c)$, which is necessary to ensure G^{max} , varies with the pulse duration (black squares).

The maximum gain increases with the pulse duration up to $\tau_c \approx 300 \text{ fs}$; for longer pulses it saturates at $G^{\text{max}} \approx 1.45$. At the same time, the pulse duration dependence of the largest gain position is linear: $\Delta t_{\text{max}} = \epsilon \tau_c$, and can be fitted with a slope of $\epsilon \approx 0.9$.

According to Eq. (2), the chirp coefficient $\dot{\omega}$ depends on the chirped pulse duration τ_c , as it is shown by the gray shaded curve in Fig. 7(b). For long pulses $\dot{\omega}$ is inversely proportional to the pulse duration τ_c (see hyperbolic asymptote shown with black dots); it decreases, however, in the vicinity of the Fourier-limited pulse duration $\tau_0 \approx 75 \text{ fs}$. The measured temporal mismatch, which is necessary for reaching the maximum gain Δt_{max} , can be used for the evaluation of a corresponding frequency detuning $\Omega_{\text{max}} = -\dot{\omega} \Delta t_{\text{max}}$. The result is plotted with blue squares in Fig. 7(b) for different pulse durations τ_c . For long pulses with $\tau_c > 300 \text{ fs}$ the largest gain is

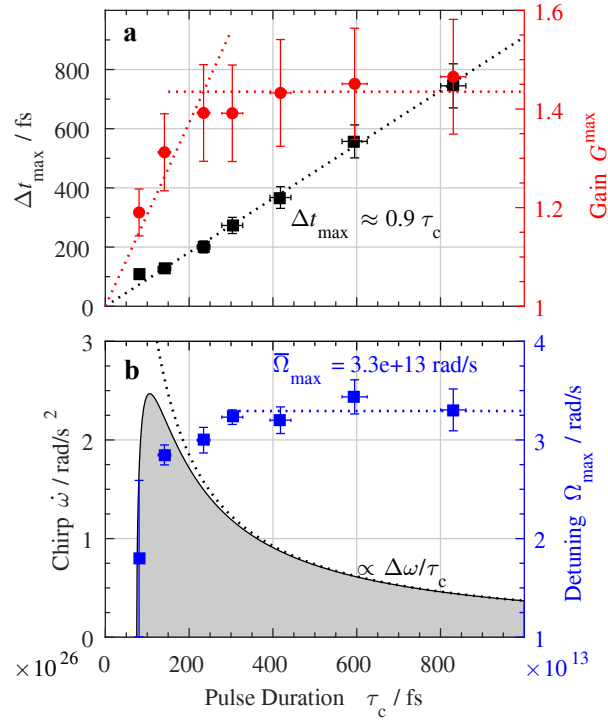


Fig. 7. (a) Pulse duration dependences of largest gain G^{\max} (red dots) and pulse temporal mismatch that ensures this largest gain Δt_{\max} (black squares). The red dotted lines are guiding the eye, while the black dotted line is a linear fit. (b) Pulse duration dependences of the chirp coefficient $\dot{\omega}$ (gray shaded curve) and pulse frequency difference that provides the maximum gain Ω_{\max} (blue squares), extracted from the data plotted in (a). The blue dotted line represents $\bar{\Omega}_{\max}$, the mean value of data above $\tau_c = 300$ fs. A hyperbolic dependence $\propto 1/\tau_c$ (black dots) shows the asymptotic behavior of the chirp coefficient $\dot{\omega}$ for long pulses. Both pulses have the same central wavelengths $\lambda = 488$ nm and bandwidths of $\Delta\omega = 3.7 \times 10^{13}$ rad/s.

always reached roughly at the same frequency detuning $\bar{\Omega}_{\max} = 3.3 \times 10^{13}$ rad/s (dotted blue line); this optimum detuning value decreases for shorter pulses. The same constant value of $\bar{\Omega}_{\max}$ can be extracted by combining Eq. (2) and Eq. (4):

$$\Omega_{\max} = \frac{\Delta\omega}{\tau_c} \epsilon \tau_c = \Delta\omega \epsilon . \quad (6)$$

Furthermore, the ϵ value close to unity indicates that for a maximum gain the pulses are temporally separated by almost their FWHM.

Thus, the presented data confirm the conclusion of subsection 3.2 that the reason of the energy redistribution between two identical pulses nests in their frequency difference. It is shown in addition that the most efficient coupling occurs always at the same optimum detuning $\bar{\Omega}_{\max}$ within a rather wide range of pulse durations.

3.4. Coupling of frequency-shifted pulses with different energies

The results of the previous subsections allow for the conclusion that the energy transfer can appear either because of a difference in incident pulse energies (subsection 3.1) or a difference in

frequencies of the two pulses (subsections 3.2 and 3.3). Whereas the origin of energy exchange for the interaction of delayed chirped pulses of equal energies can be unambiguously attributed to self-diffraction from the moving grating, caused by the frequency difference of the pulses, the non-zero gain of temporally matched, nearly Fourier-transform-limited pulses with different energies requires a more careful analysis.

At first glance, the chirp coefficient is close to zero for Fourier-transform-limited pulses and one cannot expect the removal of frequency degeneracy within the range of pulse temporal mismatch of Fig. 2. At the same time we are dealing with pulses that are not monochromatic. They possess spectra with FWHM $(3.7 - 4.0) \cdot 10^{13}$ rad/s, that exceed the optimum detuning $\Omega_{\max} = (2.0 - 3.3) \cdot 10^{13}$ rad/s [see Fig. 6(b)]. Therefore, it is not excluded that a "blue" spectral slice (with a higher frequency) in one pulse may interact with a "red" slice of lower frequency in the other pulse, and vice versa. This will not result in energy redistribution for identical pulses with the same energies because the contradirectional energy flows will fully compensate for each other. Such compensation becomes, however, only partial if two pulses have different energies; the direction of the resulting energy flow being always from the strong pulse to the weak one [cf. Fig. 4].

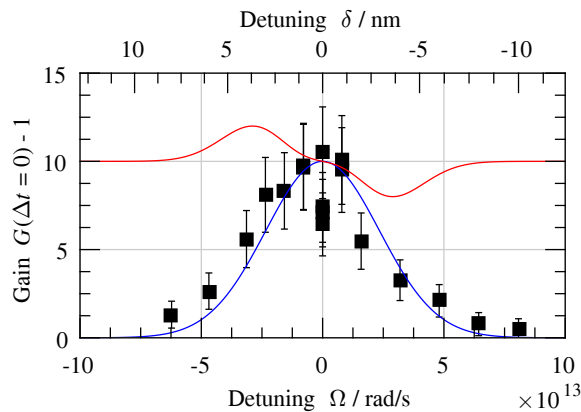


Fig. 8. Gain of a weak probe pulse $G-1$ versus probe-pump pulse frequency detuning $\Omega = \omega_{\text{pr}} - \omega_{\text{pu}}$ (black squares). Blue and red solid lines show qualitatively the expected contributions to the overall gain from transient beam-coupling and coupling from a moving grating (see text).

To clarify a possible influence of the pulse bandwidth and to identify an interaction process which is responsible for the coupling between the weak and strong pulses we have performed an additional experiment with pulses from two independently tunable OPAs. The gain of the weak probe is studied with pump and probe pulses that are matched in time but have deliberately detuned central frequencies $\Omega = \omega_{\text{pr}} - \omega_{\text{pu}}$.

As it was mentioned above, the enhancement of the "red" component of the weak pulse spectrum might be larger than the depletion of its "blue" component thus bringing overall amplification of the weak pulse. Assuming this explanation is valid, one can expect an increase of the measured gain for probe pulses which are gradually tuned to smaller frequencies until Ω_{\max} is reached. For increasing probe frequency, on the contrary, the gain is expected to drop down, becoming even smaller than unity at a certain positive Ω . Thus, one should see a strongly asymmetric detuning dependence of the gain, that is qualitatively similar to the slightly deformed dependence shown in Fig. 5(b).

The measured detuning spectrum of $G - 1$ (filled squares) is depicted in Fig. 8. The wavelength of the pump pulse $\lambda_{\text{pu}} = 488$ nm is fixed, while the probe pulse wavelength λ_{pr} is varied. The

wavelength detuning $\delta = \lambda_{\text{pr}} - \lambda_{\text{pu}}$ is added as the second x -axis on the top.

The detuning dependence of Fig. 8 is only slightly asymmetric, with the maximum shifted to longer wavelength of the probe pulse (negative frequency detuning). It looks like a superposition of a dominating bell-shaped (even) and an odd function with a smaller amplitude. These two functions are shown by blue and red solid lines for guiding the eye, red line being up-shifted to the maximum of the blue one.

Thus, we can conclude that self-diffraction from a moving grating that is recorded by the "red" spectral component of the weak pulse and the "blue" spectral component of the strong pulse does exist and manifests itself in a slight asymmetry of the spectrum shown in Fig. 8. At the same time, the dominating process responsible for coupling of weak and strong pulses in this experiment and all experiments described in subsection 3.1 is the transient energy transfer [37, 38].

4. Discussion

All presented results clearly show a net gain of a probe pulse when it is interacting with a pump pulse within congruent, nominally undoped lithium niobate. This gain cannot be a consequence of sample bleaching because of a very small linear absorption of the used sample in the blue-green spectral domain ($\alpha_{488} \leq 1 \text{ cm}^{-1}$). Moreover, to become clearly visible ($T > 1$) the gain should overcome two-photon absorption, which is quite pronounced within the intensity range of the pulses used in these experiments.

As we mentioned already, we attribute the pulse coupling effects and appearance of higher diffraction orders to self-diffraction from one and the same dynamic grating. Thus, the measured efficiency of diffraction into the first non-Bragg order $\eta \approx 0.01$ allows for estimating roughly the refractive-index modulation $\Delta n \geq (\sqrt{\eta}\lambda/\pi\ell)$. With a sample thickness of $\ell = 280 \mu\text{m}$ and a light wavelength of $\lambda \approx 0.5 \mu\text{m}$ we get Δn on the order of 10^{-4} . Taking into account Gaussian transverse intensity distribution, a nonuniform distribution within the sample thickness because of TPA and its nearly Gaussian temporal variation, the peak value of Δn should be much larger than 10^{-4} and quite strong coupling can be expected. At the same time, to ensure an efficient beam-coupling, the recorded grating should have a component which is $\pi/2$ shifted in phase with respect to the recording fringes [1–3]. The use of various inertial refractive $\chi^{(3)}$ nonlinearities can ensure the necessary phase shift between the grating and the fringes if two interacting waves differ in temporal frequencies and thus form a moving fringe pattern. The response of the inertial nonlinear medium is time-delayed. Therefore, the moving fringes produce a grating which propagates in space with the same speed as the fringes but with the extrema that do not coincide with the maxima of the intensity.

In lithium niobate, phase and/or amplitude gratings can be recorded by several known processes when using femtosecond excitation. The two-photon absorption and optical Kerr effect nonlinearities which have been considered previously as origin of dynamic grating recording [32, 33] are essentially instantaneous. Therefore, self-diffraction from relevant dynamic gratings cannot result in the intensity coupling of the recording waves. The TPA grating can only decrease the intensity of the probe beam while an instantaneous refractive index grating from the optical Kerr effect by definition can never be shifted in space with respect to the light fringes. Other known nonlinearities of LiNbO_3 are caused by photogeneration of excitons, free carrier and small polarons [29, 32, 35] as also by excitation of optical phonons. All mentioned nonlinearities are refractive and inertial and therefore can be involved in pulse coupling. Additional studies will be necessary to identify the origin of the nonlinearity which is responsible for pulse coupling in our experiments.

The intensity redistribution between two waves which are recording a moving index grating [2, 3, 6, 11, 13] is a well known phenomenon. It was reported for laser filaments in gases [6, 13] and in liquids [11] for subpicosecond pulses. Being not qualitatively new, this type of coupling is revealed now for the first time in a solid-state nonlinear material and shown to be very efficient.

The quantitative data for pulse coupling in a LiNbO₃ sample with an interaction length of only 280 μm are quite impressive: one order of magnitude amplification of the weak probe pulse energy [Fig. 3] and nearly 10% net enhancement of one of two pulses with same input energies [Fig. 6] are demonstrated. The energy is transferred from the high frequency pulse to the low frequency one with an optimum detuning of $\Omega \approx 3 \times 10^{13}$ rad/s. The frequency detuning dependences of gain G given in Fig. 6 are obviously odd functions, qualitatively similar to

$$g \propto g_0 \frac{\Omega \tau_c}{1 + \Omega^2 \tau_c^2}, \quad (7)$$

predicted by simple models for lossless media [see, e.g., Eq. (129) of [22]]. The gain factor g defines here the steady-state exponential gain of a weak probe beam, $I_{\text{pr}} \approx I_{\text{pr}}^{(0)} \exp(g\ell)$. It can be expressed via G used in this article, $g \approx (G - 1)/\ell$, ℓ standing for the interaction length. The deviation of experimental dependences of Fig. 6 from the simple form expressed by Eq. (7) might be helpful for the identification of the physical origin of nonlinearity, most probably related to certain crystal lattice resonances.

Let us compare now the manifestations of weak-to-strong pulse coupling in our experiment with the results of the transient beam-coupling model [37]. Being developed for continuous wave interaction, this model predicts no intensity coupling in the steady-state and an appearance of probe wave amplification during a time interval comparable to the grating build-up or decay time τ_r . The intensity is always transferred from a strong wave into a weak one. For the initial stage of recording, $t \ll \tau_r$, the gain increases nonlinearly with intensity I , sample thickness ℓ and time t . The relationship between the relative changes of the probe intensity I_{pr} and parameters mentioned above is as follows [37]:

$$\frac{I_{\text{pr}} - I_{\text{pr}}^{(0)}}{I_{\text{pr}}^{(0)}} = 4\Phi^2 \left[\frac{I_{\text{pu}}^{(0)} - I_{\text{pr}}^{(0)}}{I_{\text{pu}}^{(0)} + I_{\text{pr}}^{(0)}} \right] \exp\left(-\frac{t}{\tau_r}\right) \left[1 - \left(\frac{t}{\tau_r}\right) - \exp\left(-\frac{t}{\tau_r}\right) \right]. \quad (8)$$

Here, $\Phi = k_0 \Delta n \ell / 2 \cos \theta$ stands for the light-induced phase modulation in a sample with a thickness ℓ , $k_0 = 2\pi/\lambda_0$ is a wavenumber, θ is a half-angle between the interacting beams and all superscripts (0) indicate the transmitted intensity with no second wave present. In fact, Eq. (8) gives the expression for the temporal variation of the instantaneous transmission $[T(t) - 1]$ or instantaneous gain $[G(t) - 1]$.

Several assumptions in the above summarized theories prevent from a more quantitative description of the nonlinear interactions of ultrashort pulses: (i) the pulses have a particular temporal envelope which is quite different from a step-like onset in time of the pump intensity, considered in these theories, (ii) pulses with a Gaussian transverse intensity profile can hardly be treated in the plane-wave approximation, and (iii) the propagation effects are not considered in the existing theories. The analysis of the experimental data presented below allows, however, for confirming their qualitative agreement with the predictions of this simplified model.

First, it should be noted that the relationship of Eq. (8) was derived for photorefractive media in which Δn is independent of the light intensity, i.e., the gain is independent of the cw-laser beams intensity in an appropriate experiment. Taking into account that in the subpicosecond time domain the most probable processes of nonlinear index variation $\Delta n(I)$ in lithium niobate are caused by free-carriers or polarons generated via two-photon absorption [36] one can expect, even from Eq. (8), an experimental intensity dependence I^m with an exponent larger than 2. The measured gain of a probe pulse increases, as could be expected, superlinearly with the total peak intensity with $2 < m < 4$ [Fig. 3], showing an impact of the peak intensity ratio. For pulses with different peak intensities it is always the weak pulse that gains intensity [Fig. 4]. The intensity coupling disappears completely for equal peak intensities of both pulses $I_{\text{pr}} = I_{\text{pu}}$ or $R = 1$ [Fig. 4], if the pulses are perfectly matched in time. All these features permit to attribute the

coupling of the weak and strong pulses to a transient-type nonlinear interaction with an inertial phase grating involved [37,38].

We claim, therefore, that two qualitatively different coupling processes are revealed in the experiments with grating-assisted pulse coupling in LiNbO₃, one with a steady-state gain from a moving grating recorded by pulses with different frequencies and the other with a transient gain of a weak pulse in presence of a strong pump pulse with the same frequency. The experimental conditions were selected in a way to inhibit one of these two processes and to study the other one in more detail. The coupling of pulses with equal energies is, in the first instance, feasible because of the frequency difference of two temporally mismatched pulses while the transient beam-coupling can manifest itself in a small-signal amplification of pulses that are perfectly matched in time.

The physical processes that are responsible for the optical nonlinearities at the origin of grating recording itself are not yet established. Some qualitative considerations allow for formulating the requirements for their parameters. In order to observe a transient energy transfer, as it is known, the decay time of the nonlinearity should be longer compared to the pulse duration. For efficient coupling of pulses that are non-degenerated in frequency this time should be, on the other hand, comparable or shorter than the pulse duration. Thus, a good candidate for dominating inertial nonlinearity is the photoexcitation of electron-hole pairs which are further responsible for the appearance of (self-trapped) excitons and/or small, strong-coupling polarons. The nonlinearity which is contributing for coupling from moving gratings might be related to the inherent optical resonances of the LiNbO₃ lattice.

5. Conclusion

The experimental study of the dynamic grating assisted energy transfer between two sub-picosecond pulses reveals that this process can be quite efficient in LiNbO₃. The weak probe pulse can be amplified more than 10 times and the redistribution of energy between two pulses of equal intensities might approach 50% of each pulse energy. This efficient coupling is accompanied, however, by a considerable attenuation of both pulses because of two-photon absorption.

The analysis of the whole scope of experimental data leads to the conclusion that at least two different coupling processes are strongly involved, both related to self-diffraction from the recorded dynamic phase grating. The first coupling process results from the appearance of a moving grating which is shifted with respect to the moving fringe pattern, induced by two pulses with different frequencies. The frequency shift may either be introduced deliberately by using pulses from two different OPAs with adjustable wavelengths, or it may appear if the grating is recorded by two frequency chirped and temporally mismatched pulses from a single OPA. The second process manifests all characteristic features of the transient energy transfer which was first reported for cw and is closely related to stimulated Rayleigh-wing scattering. While the first process ensures an efficient unidirectional coupling between two pulses regardless of their intensity ratios, the second one always provides an efficient energy flow from the stronger to the weaker pulse.

Funding

Deutsche Forschungsgemeinschaft (DFG) (IM 37/11-1, INST 190/165-1 FUGG); Open Access Publishing Fund of Osnabrück University.

Acknowledgment

The authors gratefully acknowledge crystal preparation by K. Polgár and coworkers at the Wigner Research Centre for Physics, Budapest.

References

1. V. L. Vinetskii, N. V. Kukhtarev, S. G. Odulov, and M. S. Soskin, "Dynamic self-diffraction of coherent light beams," *Sov. Phys. Usp.* **22**, 742–756 (1979).
2. L. Solymar, D. J. Webb, and A. Grunnet-Jepsen, *The Physics and Applications of Photorefractive Materials* (Clarendon, 1996).
3. P. Yeh, *Introduction to Photorefractive Nonlinear Optics*, Wiley series in pure and applied optics (Wiley, 1993).
4. P. Günter and J.-P. Huignard, eds., *Photorefractive Materials and Their Applications*, Vol. 1–3, Springer series in Optical Science, (Springer, 2007).
5. S. Smolorz and F. Wise, "Femtosecond two-beam coupling energy transfer from Raman and electronic nonlinearities," *J. Opt. Soc. Am. B* **17**, 1636–1644 (2000).
6. A. C. Bernstein, M. McCormick, G. M. Dyer, J. C. Sanders, and T. Ditmire, "Two-beam coupling between filament-forming beams in air," *Phys. Rev. Lett.* **22**, 13–16 (2009).
7. J. K. Wahlstrand, J. H. Odnher, E. T. McCole, Y.-H. Cheng, J. P. Palastro, R. J. Levis, and H. M. Milchberg, "Effect of two-beam coupling in strong-field optical pump-probe experiments," *Phys. Rev. A* **87**, 053801 (2013).
8. R. L. Sutherland, "Energy transfer between incident laser and elastically backscattered waves in nonlinear absorption media," *Opt. Express* **13**, 9788–9795 (2005).
9. Y. Zhao, T. E. Witt, and R. J. Gordon, "Efficient energy transfer between laser beams by stimulated Raman scattering," *Phys. Rev. Lett.* **103**, 173903 (2009).
10. X. Yang, J. Wu, Y. Tong, L. Ding, Z. Xu, and H. Zheng, "Femtosecond laser pulse energy transfer induced by plasma grating due to filament interaction in air," *Appl. Phys. Lett.* **97**, 071108 (2010).
11. B. D. Stryker, M. Springer, C. Trendafilova, X. Hus, M. Zhi, A. A. Klolomenskii, H. Shroeder, J. Strohbaber, G. W. Kattawar, and A. V. Sokolov, "Energy transfer between laser filaments in liquid methanol," *Opt. Lett.* **37**, 16–18 (2012).
12. C. Gong, Y. Zheng, Z. Zheng, C. Li, X. Ge, R. Li, and Z. Xu, "Energy transfer between few-cycle laser filaments in air," *Appl. Phys. Lett.* **101**, 251111 (2012).
13. Y. Liu, M. Durand, S. Chen, A. Houdard, B. Prade, B. Forrester, and A. Mysyrowicz, "Energy exchange between femtosecond laser filaments in air," *Phys. Rev. Lett.* **105**, 055003 (2010).
14. H. J. Eichler, D. Langhans, and F. Massmann, "Coherence peaks in picosecond sampling experiments," *Opt. Commun.* **50**, 117–122 (1984).
15. C. W. Luo, Y. T. Wang, F. W. Chen, H. C. Shin, and T. Kobayashi, "Eliminate coherence spike in reflection-type pump-probe measurements," *Opt. Express* **17**, 11321–11327 (2009).
16. N. Tang and R. L. Sutherland, "Time-domain theory for pump-probe experiments with chirped pulses," *J. Opt. Soc. Am. B* **14**, 3412–3423 (1997).
17. F. Gires, "Résultats expérimentaux sur la réflexion thermique stimulée," *C. R. Acad. Sci. Ser. B* **t. 266** 596–600 (1968).
18. M. E. Mack, "Stimulated thermal light scattering in the picosecond regime," *Phys. Rev. Lett.* **22**, 13–16 (1969).
19. G. Rivoire and D. Wang, "Dynamics of CS₂ in a large spectral bandwidth stimulated Rayleigh-wing scattering," *J. Chem. Phys.* **99**, 9460–9464 (1993).
20. K. D. Dorkenoo, D. Wang, N. P. Xuan, J. P. Lecoq, R. Chevalier, and G. Rivoire, "Stimulated Rayleigh-wing scattering with two-beam coupling in CS₂," *J. Opt. Soc. Am. B* **12**, 37–42 (1995).
21. A. Dogariu, T. Xia, D. J. Hagan, A. A. Said, E. W. Van Stryland, and N. Bloembergen, "Purely refractive transient energy transfer by stimulated Rayleigh-wing scattering," *J. Opt. Soc. Am. B* **14**, 769–803 (1997).
22. P. Yeh, "Two-wave mixing in nonlinear media," *IEEE J. Quantum Electron.* **25**, 484–517 (1989).
23. R. L. Sutherland, D. G. McLean, and S. Kirkpatrick, *Handbook of Nonlinear Optics*, 2nd ed. (CRC, 2003).
24. R. W. Boyd, *Nonlinear Optics*, 3rd ed. (Academic, 2008).
25. Y. Sivan, S. Rozenberg, A. Halstuch, and A. A. Ishaaya, "Nonlinear wave interactions between short pulses of different spatio-temporal extents," *Sci. Rep.* **6**, 29010 (2016).
26. R. Trebino, *Frequency-Resolved Optical Gating: The Measurement of Ultrashort Laser Pulses* (Springer Science & Business Media, 2012).
27. R. M. Brubaker, Q. N. Wang, D. D. Nolte, E. S. Harmon, and M. R. Melloch, "Steady-state four-wave mixing in photorefractive quantum wells with femtosecond pulses," *J. Opt. Soc. Am. B* **11**, 1038–1044 (1994).
28. H. Crespo, J. T. Mendonca, and A. Dos Santos, "Cascaded highly nondegenerate four-wave-mixing phenomenon in transparent isotropic condensed media," *Opt. Lett.* **25**, 829–831 (2000).
29. H. Badorreck, A. Shumelyuk, S. Nolte, M. Imlau, and S. Odoulov, "Doppler-shifted Raman-Nath diffraction from gratings recorded in LiNbO₃ with ultra-short laser pulses of different color," *Opt. Mater. Express* **6**, 517–522 (2015).
30. S. Odoulov, A. Shumelyuk, H. Badorreck, S. Nolte, K. M. Voit, and M. Imlau, "Interference and holography with femtosecond laser pulses of different colours," *Nat. Commun.* **6**, 5866 (2015).
31. D. Staebler and J. Amodei, "Coupled wave analysis of holographic storage in LiNbO₃," *J. Appl. Phys.* **43**, 1042–1049 (1972).
32. H. T. Hsieh, D. Psaltis, O. Beyer, D. Maxien, C. von Korff Schmising, K. Buse, and B. Sturman, "Femtosecond holography in lithium niobate crystals," *Opt. Lett.* **30**, 2233–2235 (2005).
33. O. Beyer, D. Maxien, K. Buse, B. Sturman, H. T. Hsieh, and D. Psaltis, "Femtosecond time-resolved absorption processes in Lithium niobate crystals," *Opt. Lett.* **30**, 1366–1368 (2005).

34. J. P. Woerdman, "Some optical and electrical properties of a laser-generated free-carrier plasma in Si (Thesis)," Philips Res. Repts Suppl. #7 (1971).
35. P. Reckenthaeler, D. Maxien, Th. Woike, and K. Buse, "Separation of optical Kerr and free-carrier nonlinear responses with femtosecond light pulses in LiNbO₃ crystals," Phys. Rev. B **76**, 195117 (2007).
36. M. Imlau, H. Badorreck, and C. Merschjann, "Optical nonlinearities of small polarons in lithium niobate," Appl. Phys. Rev. **2**, 040606 (2015).
37. N. Kukhtarev, V. Markov, and S. Odoulov, "Transient energy transfer during hologram formation in LiNbO₃ in external electric field," Opt. Commun. **23**, 338–343 (1977).
38. V. Bryksin, A. Groznyj, V. Sidorovich, and D. Stasel'ko, "Efficient amplification of weak light beams by 3D dynamic holograms in media with thermal nonlinearity," Soviet Physics: Technical Physics Letters, **2**, 561 (1976).
39. B. Ya. Zel'dovich, N. F. Pilipetsky, and V. V. Shkunov, *Principles of Phase Conjugation* (Springer, 1985).
40. H. Badorreck, S. Nolte, F. Freytag, P. Bäune, V. Dieckmann, and M. Imlau, "Scanning nonlinear absorption in lithium niobate over the time regime of small polaron formation," Opt. Mater. Express **5**, 2729–2741 (2015).
41. F. Träger, *Springer Handbook of Lasers and Optics* 2nd ed. (Springer Science & Business Media, 2012), Chap. 12.
42. P. Yeh and A. Yariv, *Optical Waves in Crystals*, Wiley Series in Pure and Applied Optics (Wiley, 1984).
43. S. Sasamoto, J. Hirohashi and S. Ashihara, "Polaron dynamics in lithium niobate upon femtosecond pulse irradiation: Influence of magnesium doping and stoichiometry control," J. Appl. Phys. **105**, 083102 (2009).
44. A. Dogariu, and D. J. Hagan, "Low frequency Raman gain measurements using chirped pulses," Opt. Express **1**, 73–76 (1997).

A.5 Chirp control of femtosecond-pulse scattering from drag-reducing surface-relief gratings



PHOTONICS Research

Chirp control of femtosecond-pulse scattering from drag-reducing surface-relief gratings

JULIANE EGGERT,  BJOERN BOURDON, STEFAN NOLTE,  JOERG RISCHMUELLER, AND MIRCO IMLAU*

School of Physics, Osnabrück University, Barbarastr. 7, 49076 Osnabrück, Germany

*Corresponding author: mimlau@uos.de

Received 22 January 2018; revised 12 March 2018; accepted 13 March 2018; posted 14 March 2018 (Doc. ID 320238); published 2 May 2018

The role of chirp on the light–matter interaction of femto- and pico-second laser pulses with functional structured surfaces is studied using drag-reducing riblets as an example. The three-dimensional, periodic microstructure naturally gives rise to a mutual interplay of (i) reflection, (ii) scattering, and (iii) diffraction phenomena of incident coherent light. Furthermore, for femtosecond pulses, the structure induces (iv) an optical delay equivalent to a consecutive temporal delay of 230 fs in places of the pulse. These features enable studying experimentally and numerically the effect of tuning both pulse duration τ and spectral bandwidth $\Delta\omega$ on the features of the wide-angle scattering pattern from the riblet structure. As a result, we discovered a significant breakdown of fringes in the scattering pattern with decreasing pulse duration and/or increasing spectral bandwidth. This unique type of chirp control is straightforwardly explained and verified by numerical modeling considering the spectral and temporal interaction between different segments within the scattered, linearly chirped pulse and the particular geometric features of the riblet structure. The visibility of the fringe pattern can be precisely adjusted, and the off-state is achieved using $\tau < 230$ fs or $\Delta\omega > 2.85 \times 10^{13}$ rad/s.

Published by Chinese Laser Press under the terms of the [Creative Commons Attribution 4.0 License](https://creativecommons.org/licenses/by/4.0/). Further distribution of this work must maintain attribution to the author(s) and the published article's title, journal citation, and DOI.

OCIS codes: (120.4630) Optical inspection; (120.6650) Surface measurements, figure; (240.3695) Linear and nonlinear light scattering from surfaces; (280.4788) Optical sensing and sensors; (320.1590) Chirping; (320.2250) Femtosecond phenomena.
<https://doi.org/10.1364/PRJ.6.000542>

1. INTRODUCTION

Non-contact, laser-based optical sensors are crucial for the quality inspection of micro- and nano-structured surfaces in a variety of technological branches including the semiconductor industry (e.g., integrated circuit control), photonics industry (e.g., optics control), medical technology (e.g., hip joints), and automotive and aerospace fields (e.g., anti-fog and anti-icing surfaces) [1–5]. The approach to use femtosecond (fs) laser pulses as the probing light source in optical sensor technology is driven by the increasing economical availability of stable and high-power ultrashort pulse laser systems. At the same time, sub-picosecond-laser pulses represent a state-of-the-art working tool within a variety of production processes and enable fast and precise marking, cutting, soldering, and welding [6]. We here pursue the question of whether and how the use of ultrashort laser pulses in optical sensor technology may affect the measurement signal with the goal to improve the key measures that are used for quality inspection. A particular focus is given to the impact of the geometry of a relief structure on the wide-angle scattering of an incident, linearly chirped fs-laser pulse. We will therefore neglect the possible effect of

a nonlinear optical response of the surface itself, as it may be expected due to high pulse peak intensities.

The drag-reducing riblet surface [cf. scanning electron microscope (SEM) image in Fig. 1(a)] serves as an example for our study. The interaction of continuous-wave, coherent light with riblet surfaces [cf. Fig. 1(a)] has been intensively studied for the purpose of quality inspection before [7–10]. Riblets obey their relevance in the engineering of drag reduction as they affect skin friction considerably [11–15]. The riblet functionality depends essentially on the integrity of the geometrical shape and therefore on the possibility to detect geometric alterations during production and maintenance with high precision in the submicrometer range at high sensing speed. The optical sensor described in Ref. [8] ensures these demands at high reliability due to a simple optical design [Fig. 1(b)]: a laser beam is incident normal to the riblet sample's surface, such that a wide-angle scattering pattern appears. The pattern consists of three main features in the $\pm 45^\circ$ and 0° directions with respect to the sample's surface and in plane with the incoming beam in accordance with the triangular riblet structure and planes in between. Degradation of the riblets is measured as a decrease in the

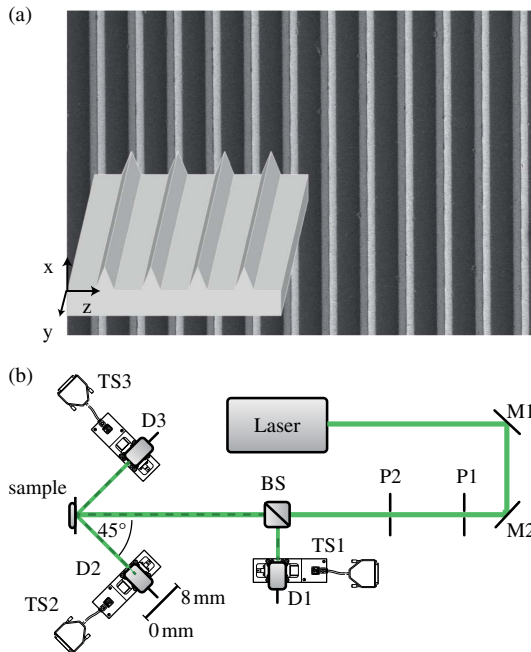


Fig. 1. (a) Scanning electron microscope (SEM) image and schematic, three-dimensional representation of the riblet structure under study. (b) Scheme of the optical setup of the riblet sensor described in Refs. [8,9]: the laser beam is incident normal to the riblet sample's surface, and the intensity distribution of the scattered light is detected in the 0° and ±45° directions. Degradation of the riblet structure is measured as a decrease in intensity around 45°.

intensity in the directions around 45°. Another characteristic of the scattered signal is the interference substructure [8] as a result from light diffraction at the periodic microstructure. It may be used for quality inspection as well [10] and contains information about riblet periodicity and duty cycle. However, we intend to disregard this signal due to signal fluctuations caused by the Moiré effect if fringe and detector array periodicities coincide [16].

One way to suppress the interference structure is to choose a detector diaphragm much larger than the fringe spacing. This strategy can be either realized by an appropriate Iris and/or distance between sample and photodiode. As a disadvantage, however, the dimensions of the optical setup are considerably extended, and the information about the riblet periodicity is lost.

In this work we introduce another strategy for the elimination of interference effects that is based on linearly chirped ultrashort laser pulses as the probing light source. The underlying idea is schematically sketched in Figs. 2(a) and 2(b): from ray-tracing considerations of an incident laser pulse onto a riblet structure, a difference of the optical path length in the ±45°-direction for waves reflected at neighboring flanks becomes obvious. This spatial delay can be estimated to about 70 μm for the given riblet structure under study (Λ = 100 μm, b = 50 μm). It corresponds with a temporal delay of about Δt = 230 fs. The latter is of importance if ultrashort laser pulses are used, in particular, if the pulse duration is in the order

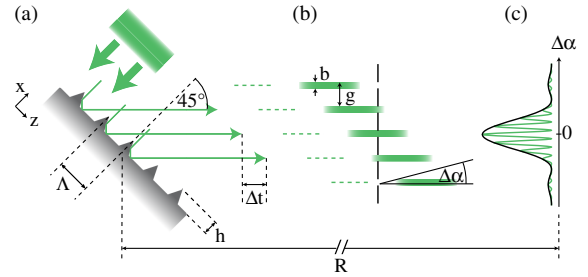


Fig. 2. (a) Scheme of the pulse front reflected in the 45° direction and distinct pulse path lengths from next-neighboring riblet flanks. Period Λ of the riblet structure is 100 μm, and riblet height b is 50 μm. The spatial delay induced by the riblet structure is 70 μm, and the correlated temporal delay is about Δt = 230 fs. (b) and (c) are discussed in the simulation section.

of magnitude of the temporal delay: when the pulse duration is adjusted below the temporal delay, $\tau < \Delta t$, the pulses do not overlap, and the interference should vanish.

In what follows, and based on these preconsiderations, we will examine differences between the following three probing approaches:

- probing with pulse durations $\tau < \Delta t$;
- probing with pulse durations $\tau > \Delta t$ and a broad frequency spectrum;
- probing with pulse durations $\tau > \Delta t$ and both decreasing pulse duration and frequency spectrum.

Both experimental and simulation methods are applied. Our comprehensive study shows that a complete disappearance of the interference at ±45° can be obtained. At the same time, it is possible to keep the interference in the scattering pattern in the direction around 0°. Thus, full access to analyze all important features of the riblet structure (periodicity, deviations of periodicity) is maintained. Furthermore, in analyzing the effect of pulse duration and bandwidth in more detail, we are able to precisely deduce the pulse characteristics for an all-optical control of the appearing wide-angle, scattering pattern. Thus, it becomes possible to choose between on and off states of the interference pattern by proper adjustment of the pulse parameters. Our results enable the redesign of the optical setup with much smaller dimensions while maintaining its reliability and precision. All our findings can be transferred to fs-pulse sensing of surface relief structures with different geometric shapes and dimensions, if the optical delay induced by the structure falls in the time region of the applied pulse duration.

2. EXPERIMENTS

A. Femtosecond Pulses and Simplified Pulse Shaping

We will use the following textbook knowledge about femtosecond pulses as fundament for our study: the time-bandwidth product $\Delta\omega \cdot \tau \geq 4 \ln 2$ for Gaussian-shaped pulses defines a minimum duration τ_0 for a given bandwidth based on the uncertainty principle. As an example, fs pulses in the visible spectral range with durations of $\tau = 50$ fs cover a bandwidth of more than 10 nm. A pulse that is close to the time-bandwidth product is called Fourier-limited, but it does not

preserve its shape when propagating through glass or several meters in air. Dispersion of the refractive index leads to different velocities of the spectral groups within the pulse, causing an extension of the pulse duration (group velocity dispersion) [17]. In the simplest case, a linear chirp results: $\omega(t) = \omega_0 + at$, with central frequency ω_0 and chirp parameter a . For what follows, it is important to note that the chirp parameter a , obtained via frequency gradient $a = \partial\omega/\partial t$, decreases as a function of increasing pulse duration of an incident pulse under the condition of a fixed bandwidth.

If the time-dependent frequency $\omega(t)$ is known, the spectral pulse shape can be transferred to a temporal pulse shape via Fourier transform and vice versa. In the following approach, the simplification

$$\frac{\partial\omega}{\partial t} = \frac{\Delta\omega}{\tau} \sqrt{1 - \left(\frac{\tau_0}{\tau}\right)^2} \approx \frac{\Delta\omega}{\tau} \quad (1)$$

is used to extract the frequency gradient from bandwidth and duration of a strongly chirped pulse $\tau_0/\tau \ll 1$.

Let us transfer this knowledge to design an optical setup for a proper experimental control. On the one hand, the magnitude of pulse chirp from dispersion can be varied by the thickness of the medium. On the other hand, the angular dispersion from prism and grating pairs is used so that the chirp is determined by the distance between them. This procedure is used in every pulse compressor/stretcher to achieve the desired pulse duration [18].

According to Eq. (1), for a fixed bandwidth, the pulse duration depends on the frequency gradient. But for strongly chirped pulses it is also possible to keep the frequency gradient fixed, so that the pulse duration depends on the bandwidth. Both processes are utilized in the following investigations to adapt the abovementioned dependencies.

The first applied method uses group velocity dispersion of borosilicate crown glass to extend the temporal profile by altering the pulse chirp while keeping the spectrum unchanged [cf. Eq. (1)]. A sketch of the experimental realization is shown in Fig. 3(a).

The second technique for fs-pulse shaping manipulates the spectral and temporal features of the pulse concurrently at constant pulse chirp inside a grating stretcher as shown in Fig. 3(b). The first grating BG1 decomposes the spectrum, and the second grating BG2 recollimates the beam while maintaining the spatial wavelength sort. A variable slit in the spatially dispersed spectrum cuts off the high- and low-frequency components [19,20]. Under the condition that the laser pulse is not bandwidth-limited, both the spectral bandwidth and the pulse duration are reduced as the slit width decreases. The advantage of this simplified setup is that an additional pulse duration stretch due to lenses and difficulties of chromatic aberration are eliminated [21].

B. Experimental Setups

An optical parametric amplifier (OPerA solo, Coherent Inc., USA) pumped by a regeneratively amplified Ti³⁺:sapphire laser (Libra-F HE, Coherent Inc., USA) serves as the source for ultrashort laser pulses. The central wavelength is adjusted to $\lambda = 515$ nm, and the spectral bandwidth is

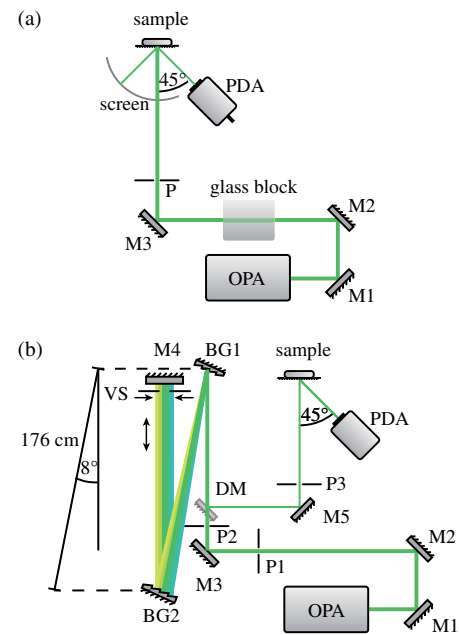


Fig. 3. (a) First setup: the laser beam is incident via mirrors M1–M3 normal to the riblet sample's surface and the scattered intensity pattern is observed on a screen or detected via a photodiode array in the 45° direction. The initial pulse duration is $\tau = 109$ fs. In order to expand the pulse duration, blocks of borosilicate crown glass are placed into the beam path. (b) Second setup: the laser beam is adjusted into a grating stretcher built of BG1, BG2, and M4. Distance between the two blazed gratings of 176(1) cm results in $\tau_2 = 2.4$ ps. The variable slit VS allows for a limitation of the effective bandwidth $\Delta\omega$ of the laser pulse. Its aperture a is varied from 1 to 7 mm. The D-shaped mirror DM separates incoming and stretched pulses. P1–P3 are pinholes to eliminate scattering.

$\Delta\omega = 3.56 \times 10^{13}$ rad/s, estimated via a fiber spectrometer (USB4000, Ocean Optics Inc., USA). In the first experimental setup, shown in Fig. 3(a), the laser beam is incident via mirrors M1–M3 normal to the riblet sample's surface, and the scattered intensity pattern is observed on a screen or detected via a photodiode array (S3902-512Q, Hamamatsu Photonics K.K., Japan) in the 45° direction at a distance between sample and detector of 36.0(5) cm. A pinhole limits the incident beam diameter to $d = (1.0 \pm 0.1)$ mm. The initial pulse duration is estimated via an autocorrelator (pulseCheck 15, APE, Germany) to be $\tau = 109(5)$ fs.

In order to expand the pulse duration, blocks of borosilicate crown glass with edge lengths of 56, 131, 171, and 211 mm are placed into the beam path, resulting in pulse durations of 234(5), 370(5), 680(5), and 900(5) fs, respectively.

In Fig. 3(b), a scheme of the second experimental setup is shown. The same laser beam as used above is adjusted into a double grating setup built of BG1, BG2, and M4 that stretches the pulse duration as a function of the distance between the two blazed diffraction gratings BG1 and BG2, blaze wavelength $\lambda_b = 500$ nm, and line spacing $1/d = 300$ mm⁻¹ (GR25-0305, Thorlabs, Inc., USA) [18]. The distance between the two blazed gratings is adjusted to 176(1) cm, resulting in a measured stretch of pulse duration of $\tau = 2.4(1)$ ps. In our

Table 1. Slit Apertures a , Pulse Duration τ , and Spectral Bandwidth $\Delta\omega^a$

Slit Aperture a (mm)	Pulse Duration τ (ps)	Spectral Bandwidth $\Delta\omega$ (rad/s)	$\Omega\tau$
7.0(1)	2.40(10)	3.56×10^{13}	8.18
6.0(1)	2.30(10)	3.56×10^{13}	8.18
5.0(1)	2.25(10)	2.85×10^{13}	6.55
4.0(1)	2.00(10)	2.35×10^{13}	5.40
3.0(1)	1.70(10)	2.42×10^{13}	5.56
2.0(1)	1.25(20)	2.06×10^{13}	4.75
1.0(1)	0.90(20)	1.92×10^{13}	4.42

^aThe product $\Omega\tau$ is depicted in the discussion.

experiment, the product $\Delta\omega \cdot \tau \geq 17$ and is therefore well above the bandwidth limit. The variable slit VS allows for a limitation of the effective bandwidth $\Delta\omega$ of the laser pulse. Its aperture a is varied from 1 to 7 mm. The D-shaped mirror DM separates the incoming and stretched pulses. The hereby resulting pulse durations and spectral bandwidths are measured via autocorrelator and spectrometer, respectively; an overview is presented in Table 1. The D-shaped mirror DM separates the incoming and stretched pulses. The scattered intensity is measured around 45° by a photodiode array device (S3902-512Q, Hamamatsu Photonics K.K.) with a spatial resolution of approximately 202 pixels/cm, and the distance between sample and detector is 36.0(5) cm. The spectral bandwidth decreases with the slit aperture. It is understandable that the pulse duration, which is initially determined by the stretching induced by the two gratings, is decreased when the maximal and minimal wavelengths are cut off, provided the pulse is not Fourier-transform-limited.

3. RESULTS

A. Experimental Results

Figure 4(a) shows the intensity pattern of the 45° signal obtained with the first setup for pulse durations of (1) 109 fs, (2) 234 fs, (3) 370 fs, (4) 680 fs, and (5) 900 fs, respectively. At all pulse lengths, the intensity distribution is consistent and shows no substructure. The visual appearance of this intensity pattern is shown in the screen photograph in Fig. 4(b) at $\tau = 900$ fs and accordingly shows a smooth appearance. This finding is in contrast to the observable substructure of the 45° signal in Fig. 4(d), obtained with a continuous-wave laser (Compass 215M-75, $\lambda = 532$ nm, Coherent Inc., USA) and well-known from previous experiments [7–9]. In the 0° direction, both intensity patterns in Figs. 4(c) and 4(e) show distinct interference features with three prominent center peaks.

In the setup of Fig. 3(b), the fringe pattern is studied as a function of slit aperture a as depicted in Fig. 5. For a slit aperture of $a = 7$ mm, a smooth intensity distribution is visible as found in Figs. 4(a) and 4(b). As the slit aperture decreases, the interference fades in towards a well-defined substructure at $a = 1$ mm.

The results of the detected intensity patterns for $a = 1$ mm and $a = 7$ mm are shown and fitted to the sum of two Gaussian functions. As suggested in Ref. [8], the area integral

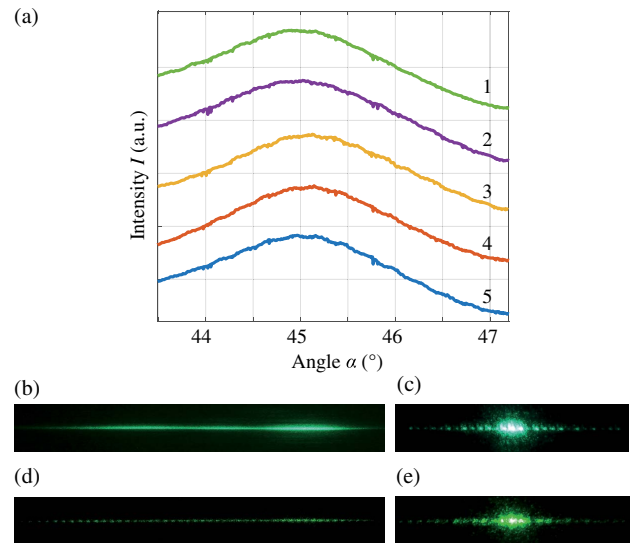


Fig. 4. (a) Intensity patterns of the 45° signal obtained with the first setup for pulse durations of (1) 109 fs, (2) 234 fs, (3) 370 fs, (4) 680 fs, and (5) 900 fs, respectively. (b)–(e) Photographs of the intensity patterns (b), (c) at 900 fs and (d), (e) with a continuous-wave laser ($\lambda = 532$ nm). (b) The 45° signal appears smoothly. This finding is in contrast to the observable substructure of the 45° signal well-known from continuous wave-experiments shown in (d). (c), (e) In 0° direction, both intensity patterns show distinct interference features with three prominent center peaks.

of the Gaussian graph is used for degradation. The data set furthermore reveals that the position of the fringe maxima is slightly displaced as a function of slit aperture. This effect can be attributed unambiguously to the spatial displacement of the laser beam induced by the mechanical changes in the slit aperture. As a result, the laser spot position is slightly displaced on the riblet sample, that in turn displaces the position of the fringe maxima on our detector array.

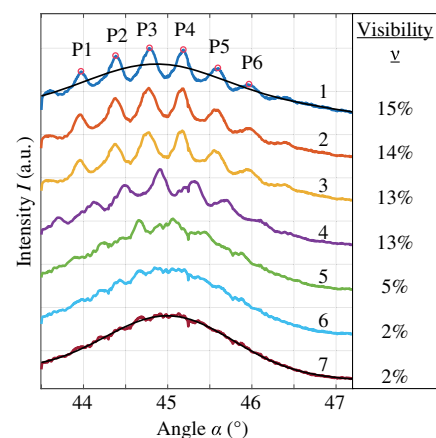


Fig. 5. Intensity pattern as a function of slit aperture a and accordingly labeled from 1 to 7. Smooth intensity distribution for $a = 7$ mm as found in Fig. 4(a). With decreasing slit aperture and consequently decreasing pulse duration and bandwidth, the interference pattern appears. The results of the detected intensity patterns for $a = 1$ mm and $a = 7$ mm are fitted to the sum of two Gaussian functions. On the right, the respective visibilities ν are specified.

Since the focus of this work is not on the evaluation of the degradation, but on the analysis of the interaction between chirped ultrashort pulses and the riblet structure, the fit parameters will not be discussed further. Rather, we turn to the appearance of interference. Related to the fringe pattern, we can define the interference by the contrast, namely given by the visibility ν

$$\nu = \frac{I_{\max} - I_{\min}}{I_{\max} + I_{\min}}. \quad (2)$$

It is determined by averaging the specific visibilities of the six main peaks of the pattern as marked in Fig. 5. The results for ν are listed in Fig. 5 and cover resulting visibility values between 2% and 15%.

B. Simulation

In what follows, we attempt to analyze in more detail the correlation of pulse duration, bandwidth, and fringe pattern in the 45° direction. For this purpose, we refer to Fig. 2(b) and introduce the periodicity g of light emission parallel to 45° , which is determined by the riblet period Λ : $g = \Lambda \cdot \sin 45^\circ$, and width b of a single reflection, which is equal to the width of one riblet flank.

Under these conditions, the generated scattering pattern at distance R can be interpreted as a diffraction signal from a multiple slit as geometrically sketched in Figs. 2(a) and 2(b).

In order to simulate this intensity pattern we describe the time- and angle-dependent electrical field by a sum of a series of normalized plane waves as follows:

$$E(\Delta\alpha, t) = \sum_{n=1}^N \sum_{m=1}^M A_n(t_n) \exp[i(k_n R - (\omega_0 + \frac{1}{2} \dot{\omega} t_n) t_n + \phi_n + \phi_m)], \quad (3)$$

with

$$A_n(t_n) = \exp \left\{ -\frac{2 \left\{ \left[n - \frac{1}{2} (N + 1) \right] \Lambda \right\}^2}{w_r^2} \right\} \cdot \exp \left[-2 (\ln 2) \frac{t_n^2}{\tau^2} \right], \quad (4)$$

$$t_n(t) = t - (n - 1) \cdot \Delta t, \quad (5)$$

$$\omega_n(t_n) = \omega_0 + \dot{\omega} \cdot t_n, \quad (6)$$

$$\phi_n(\omega_n) = \frac{\omega_n}{c} \cdot \sin(45^\circ + \Delta\alpha) \Lambda \cdot \sin 45^\circ \cdot (n - 1), \quad (7)$$

$$\phi_m(\omega_n) = \frac{\omega_n}{c} \cdot \sin(45^\circ + \Delta\alpha) \frac{b}{M - 1} \cdot (m - 1). \quad (8)$$

The natural numbers N and M thereby describe the number of slits and the number of reflected waves at each slit, respectively. The term A_n determines the Gaussian-shaped envelope amplitude based on the transversal beam waist w_r [at $\exp(-2)$ intensity] and the pulse duration τ (full width

at half-maximum, FWHM). The time t_n is a function of the slit number n because of the consecutive delay Δt . The frequency ω_n is a function of time, respecting the frequency gradient $\partial\omega/\partial t$, that results in a time dependence of the wave vector $k_n = \omega_n/c$ as well (c is the speed of light). The phase differences $\phi_{n,m}$ are determined by wave vectors k_n as a function of time due to pulse chirp, besides the geometrical conditions, namely Λ , b , R , and angle of observation $\Delta\alpha$.

Integration of Eq. (3) over time then yields the energy density pattern $W(\Delta\alpha)$

$$W(\Delta\alpha) = \int |E(\Delta\alpha, t)|^2 dt. \quad (9)$$

With this model, it is possible to simulate both of the experimental setups. We like to note that based on Eq. (1), the frequency gradient, bandwidth, and pulse duration are coupled in a way that it is not possible to separately change one of them. Therefore the pulse duration τ can only be altered in expense of the frequency gradient $\partial\omega/\partial t$ [Fig. 6(a)] or the bandwidth $\Delta\omega$ [Fig. 6(b)].

Figure 6 shows the results of the simulations based on Eq. (9) for the bandwidth and frequency gradient according to the experiment. No interference effects are visible when changing the pulse duration, and thus the frequency gradient, at a constant bandwidth [Fig. 6(a)]. However, changing the bandwidth, and thus the pulse duration, at a constant frequency gradient reveals a different picture [Fig. 6(b)]: a diffraction pattern appears in a certain window of bandwidths between $\Delta\omega \approx (0.3\text{--}2.2) \times 10^{13}$ rad/s and pulse durations between $\tau \approx 200\text{--}1500$ fs.

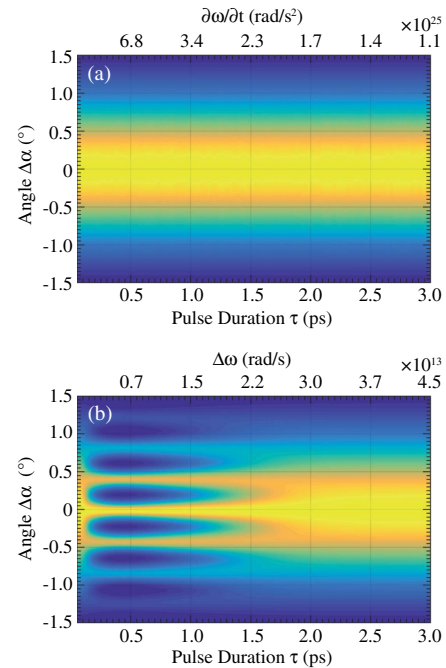


Fig. 6. Numeric energy pattern $W(\Delta\alpha)$ for 45° (a) for a constant bandwidth of $\Delta\omega = 3.41 \times 10^{13}$ rad/s ($\Delta\lambda = 4.8$ nm) and variable pulse duration τ and frequency gradient $\partial\omega/\partial t$, and (b) for a constant frequency gradient $\partial\omega/\partial t = 1.49 \times 10^{25}$ rad/s² and variable pulse duration τ and bandwidth $\Delta\omega$ ($N = 13$, $M = 5$, $b = 15$ μm , $\Lambda = 100$ μm , $R = 0.36$ m).

The calculations were also applied to the direct reflection signal in the 0° direction. In this case, a stationary interference pattern is formed regardless of the chosen parameters for pulse duration τ and bandwidth $\Delta\omega$ (not shown).

4. DISCUSSION

The results of the experiments and the simulation are consistent with each other, and the observed phenomena can be explained on the basis of temporal pulse sequences and interference.

In the 0° direction, the interference pattern is distinctly visible and can be directly attributed to the model of a multiple slit only. This signal originates from perpendicular reflection at the riblet plains, so that no optical path difference is induced in this direction ($\Delta t = 0$, cf. Ref. [9]). In the case of a linearly chirped pulse, the same frequencies simultaneously reach the detector while the chirp is maintained. This case is comparable to probing with continuous-wave light of bandwidth $\Delta\omega$.

In the 45° direction, we can distinguish between three cases. In the simplest case, the pulse duration τ is below the temporal delay Δt , and therefore there is no overlap of next-neighbouring pulse sections, i.e., no interference. The other two cases are depicted in Figs. 7(a) and 7(b) and represent the first [cf. Fig. 3(a)] and second experimental setup [cf. Fig. 3(b)] at $\tau = 900$ fs, respectively.

Shown is a plot of frequency ω and power P versus time for two next-neighbouring pulses with a mutual temporal delay of 230 fs. The slope of frequency is $\partial\omega/\partial t = \Delta\omega/\tau$.

The pulse durations in Figs. 7(a) and 7(b) are similar, whereas the bandwidths are different: $\Delta\omega_a > \Delta\omega_b$, and thus the frequency gradient $\partial\omega/\partial t$ in Fig. 7(a) is larger. Therefore, the difference Ω_a of superposing frequencies is high, and no stationary interference pattern is formed [21]. With decreasing

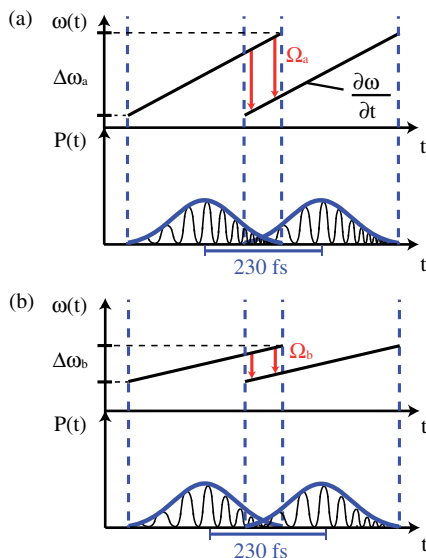


Fig. 7. Plot of frequency ω and power P versus time for two next-neighbouring pulses with a mutual temporal delay of 230 fs. Slope of frequency is $\partial\omega/\partial t = \Delta\omega/\tau$. (a) Frequency detuning Ω_a for overlapping pulses. (b) Same pulse duration as in (a), while bandwidth is decreased, which results in the appearance of a stationary interference pattern.

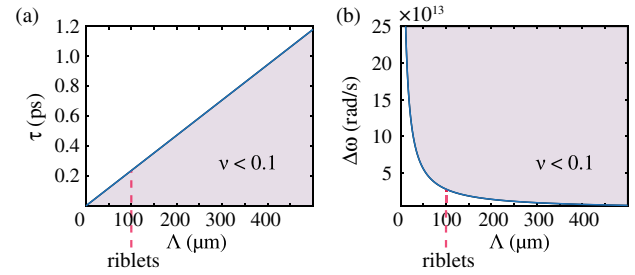


Fig. 8. Influence of structure period Λ on threshold values of (a) pulse duration τ and (b) bandwidth $\Delta\omega$ for a vanishing interference pattern ($\nu < 0.1$). Characteristic period $\Lambda = 100 \mu\text{m}$ of the investigated riblet structure is marked, respectively.

bandwidth of the pulse $\Delta\omega_b < \Delta\omega_a$ [cf. Fig. 7(b)], the interference pattern appears (cf. Fig. 5) as the frequency difference Ω_b is reduced: $\Omega_b < \Omega_a$. The latter is determined by pulse duration τ and bandwidth $\Delta\omega$ or frequency gradient of the pulses $\partial\omega/\partial t$

$$\Omega = \frac{\Delta\omega}{\tau} \cdot \Delta t = \frac{\partial\omega}{\partial t} \cdot \Delta t. \quad (10)$$

For interference, however, Ω alone is not decisive but rather the product $\Omega\tau$. This is illustrated by the second experiment where the frequency gradient $\partial\omega/\partial t$ is constant and thus also $\Omega(t)$, but the visibility of the interference pattern differs essentially. As a condition for interference, an upper boundary value for the product $\Omega\tau$ can be estimated [22]. The values for $\Omega\tau$ of our experiments are depicted in Table 1. Concluding these considerations, the appearance of the interference can be adjusted via the pulse parameters. We note that further parameters may be deduced from the dependence of the scattering features on pulse duration and bandwidth, e.g., the determination of the pulse chirp from the fringe visibility. For this purpose and a sufficient precision, however, it will be necessary to make a point of improving the fringe contrast by appropriate laser (intensity, coherence length, etc.) and/or riblet (periodicity, riblet height, etc.) parameters.

For the particular case of a fixed temporal delay Δt , the product $\Omega\tau$ reads

$$\Omega\tau \leq C \Leftrightarrow \Delta\omega \leq \frac{C}{\Delta t}. \quad (11)$$

Constant C can be drawn from the measurement data. For a vanishing interference contrast of less than 10%, $\Delta\omega > 2.85 \times 10^{13}$ rad/s is valid, which corresponds to $C = 6.56$.

In Fig. 8 the influence of structure period Λ on the threshold values of pulse duration τ and bandwidth $\Delta\omega$ for a vanishing interference pattern ($\nu < 0.1$) is depicted for $C = 6.56$.

The investigations show clearly that the impact on measurements needs to be considered when using a chirped ultrashort laser pulse. In general, one can expect an influence on interference when a temporal delay Δt is induced to fractions of the chirped pulses by a microstructure. Besides the simple case with $\tau < \Delta t$, the choice of bandwidth and chirp affect the appearance of interference effects as well. According to the goal of

our study, we were able to suppress the fringe pattern that overlays with the scattering pattern.

5. CONCLUSIONS

We have introduced the chirp as a novel parameter for the all-optical control of a wide-angle scattering pattern with a drag-reducing riblet structure as an example. In our particular example, we are able to deduce precise requirements for a smooth measurement signal in the 45° direction with a visibility of the interference $\nu < 0.1$ (pulse duration $\tau < 230$ fs or bandwidth $\Delta\omega > 2.85 \times 10^{13}$ rad/s for linearly chirped pulses). The vanishing of the interference substructure as main objective of our study enables the use of a photodiode array within the riblet sensor. This results in an effective improvement of the measurement speed and the possibility to redesign the optical sensor setup with much smaller dimensions. Reliability and precision of the sensor are maintained. It is noteworthy that a standard fs-pulse laser implemented into the riblet sensor fulfills the requirements for a smooth intensity signal in the 45° direction. All our considerations can be easily transferred to similar structured surfaces and specific limit values can be obtained if the optical delay induced by the geometric structure coincides with the pulse duration.

Funding. Seventh Framework Programme (FP7) (CSJU-GAM-SFWA-2008-001); Deutsche Forschungsgemeinschaft (DFG); European Union's Seventh Framework Program (FP7/2007-2013); Clean Sky Joint Technology Initiative (CSJU-GAM-SFWA-2008-001).

Acknowledgment. The authors acknowledge financial support by the European Union's Seventh Framework Program for the Clean Sky Joint Technology Initiative. We acknowledge support by Deutsche Forschungsgemeinschaft (DFG) and Open Access Publishing Fund of Osnabrück University.

REFERENCES

1. M. M. Moslehi, "Sensor for semiconductor device manufacturing process control," U.S. patent 5,293,216 (March 8, 1994).
2. M. M. Moslehi, "Apparatus for semiconductor device fabrication diagnosis and prognosis," U.S. patent 5,719,495 (February 17, 1998).
3. J.-H. Lee, J. P. Singer, and E. L. Thomas, "Micro-/nanostructured mechanical metamaterials," *Adv. Mater.* **24**, 4782–4810 (2012).
4. B. Kasemo, "Biological surface science," *Surf. Sci.* **500**, 656–677 (2002).
5. V. A. Ganesh, H. K. Raut, A. S. Nair, and S. Ramakrishna, "A review on self-cleaning coatings," *J. Mater. Chem.* **21**, 16304–16322 (2011).
6. J. Ion, *Laser Processing of Engineering Materials: Principles, Procedure and Industrial Application* (Butterworth-Heinemann, 2005).
7. M. Imlau, H. Brüning, K.-M. Voit, J. Tschentscher, S. Dieckhoff, U. Meyer, K. Brune, J. Derksen, and C. Tornow, "A method for quality control of a micro-structuring and apparatus therefor," DE102013220006A1 (April 2, 2015).
8. M. Imlau, H. Brüning, K.-M. Voit, J. Tschentscher, and V. Dieckmann, "Riblet sensor—light scattering on micro structured surface coatings," arXiv: 1601.04694 (2016).
9. J. Tschentscher, S. Hochheim, H. Brüning, K. Brune, K.-M. Voit, and M. Imlau, "Optical riblet sensor: beam parameter requirements for the probing laser source," *Sensors* **16**, 458 (2016).
10. U. Meyer, S. Markus, and S. Dieckhoff, "Device for testing the quality of microstructurization," U.S. patent 8,842,271 (September 23, 2014).
11. D. W. Bechert, M. Bruse, W. Hage, J. G. T. van der Hoeven, and G. Hoppe, "Experiments on drag-reducing surfaces and their optimization with an adjustable geometry," *J. Fluid Mech.* **338**, 59–87 (1997).
12. M. Bruse, D. Bechert, J. T. van der Hoeven, W. Hage, and G. Hoppe, "Experiments with conventional and with novel adjustable drag-reducing surfaces," in *Proceedings of the International Conference on Near-Wall Turbulent Flows*, Tempe, Arizona (March 15–17, 1993), pp. 719–738.
13. M. J. Walsh, "Effect of detailed surface geometry on riblet drag reduction performance," *J. Aircr.* **27**, 572–573 (1990).
14. D. W. Bechert, M. Bruse, W. Hage, and R. Meyer, "Fluid mechanics of biological surfaces and their technological application," *Naturwissenschaften* **87**, 157–171 (2000).
15. B. Dean and B. Bhushan, "Shark-skin surfaces for fluid-drag reduction in turbulent flow: a review," *Philos. Trans. R. Soc. London A* **368**, 4775–4806 (2010).
16. G. C. Holst, *CCD Arrays, Cameras, and Displays* (JCD, 1998).
17. L. Brillouin, *Wave Propagation and Group Velocity* (Academic, 2013), Vol. 8.
18. E. Treacy, "Optical pulse compression with diffraction gratings," *IEEE J. Quantum Electron.* **5**, 454–458 (1969).
19. J. P. Heritage, R. N. Thurston, W. J. Tomlinson, A. M. Weiner, and R. H. Stolen, "Spectral windowing of frequency-modulated optical pulses in a grating compressor," *Appl. Phys. Lett.* **47**, 87–89 (1985).
20. J. P. Heritage, A. M. Weiner, and R. N. Thurston, "Picosecond pulse shaping by spectral phase and amplitude manipulation," *Opt. Lett.* **10**, 609–611 (1985).
21. A. M. Weiner, "Ultrafast optical pulse shaping: a tutorial review," *Opt. Commun.* **284**, 3669–3692 (2011).
22. S. Odoulov, A. Shumelyuk, H. Badorreck, S. Nolte, K.-M. Voit, and M. Imlau, "Interference and holography with femtosecond laser pulses of different colours," *Nat. Commun.* **6**, 5866 (2015).

Acknowledgement

Zuallererst möchte ich Herrn Prof. Dr. Mirco Imlau danken für die Aufnahme in der Arbeitsgruppe *Ultrakurzzeitphysik* und die interessante Thematik der holografischen Gitter mit Femtosekundenpulsen. Außerdem danke ich ihm für die stetige Diskussionsbereitschaft und Unterstützung während der gesamten Promotion.

Ich möchte mich auch bei Herrn Prof. Dr. Dominik Schaniel von der Universität Lorraine bedanken für die Begutachtung dieser Arbeit.

Special thanks are also dedicated to Prof. Dr. Serguey Odoulov from National Academy of Sciences of Ukraine for fruitful discussions, patience in explaining the particularities of dynamic holography as well as his kind support even beyond physics not only during my stay in Kiev.

Weiterhin möchte ich mich auch bei Herrn Dr. Holger Badorreck und Herrn M.Sc. Björn Bourdon für die gute Zusammenarbeit bedanken. Mein Dank gilt außerdem auch allen anderen aktuellen und ehemaligen Kollegen in der Arbeitsgruppe für die interessanten Diskussionen, stetige Hilfsbereitschaft und das nette Arbeitsklima.

Den Mitarbeitern der elektronischen und feinmechanischen Werkstätten danke ich für die Hilfe und schnelle Bearbeitung von verschiedensten Reparatur- und Entwurfsarbeiten.

Der letzte und wichtigste Dank gilt meinen Eltern und meiner ganzen Familie für ihre langjährige Unterstützung, während der Promotion und des gesamten Studiums.

Eidesstattliche Erklärung

Ich erkläre hiermit, die vorliegende Arbeit selbstständig und ohne unerlaubte Hilfe verfasst und keine anderen als die angegebenen Hilfsmittel und Quellen verwendet zu haben.

Osnabrück, den 9. August 2018